This is to certify that the
dissertation entitled

CONTROL OF MULTIPHOTON MOLECULAR EXCITATION
WITH SHAPED FEMTOSECOND LASER PULSES

presented by

Bingwei Xu

has been accepted towards fulfillment
of the requirements for the

Ph. D. degree in Chemistry

Major Professor's Signature

Aug 22, 2008

Date

CONTROL OF MULTIPHOTON MOLECULAR EXCITATION WITH SHAPED FEMTOSECOND LASER PULSES

By

Bingwei Xu

A DISSERTATION

Submitted to
Michigan State University
In partial fulfillment of the requirements
For the degree of

DOCTOR OF PHILOSOPHY

Chemistry

2008

ABSTRACT

CONTROL OF MULTIPHOTON MOLECULAR EXCITATION WITH SHAPED FEMTOSECOND LASER PULSES

By

Bingwei Xu

The work presented in this dissertation describes the use of shaped femtosecond laser pulses to control the outcome of nonlinear optical process and thus to achieve the selectivity for multiphoton molecular transitions. This research could lead to applications in various fields including nonlinear optical spectroscopy, chemical identification, biological imaging, communications, photodynamic therapy, etc.

In order to realize accurate pulse shaping of the femtosecond laser pulses, it is essential to measure and correct the spectral phase distortion of such pulses. A method called multiphoton intrapulse interference phase scan is used to do so throughout this dissertation. This method is highly accurate and reproducible, and has been proved in this work to be compatible with any femtosecond pulses regardless of bandwidth, intensity and repetition rate of the laser. The phase control of several quasi-octave laser sources is demonstrated in this dissertation, with the generation of 4.3 fs and 5.9 fs pulses that reach the theoretically predicted transform-limited pulse duration.

The excellent phase control achieved also guarantees the reproducibility for selective multiphoton excitations by accurate phase and/or amplitude shaping. Selective two-photon excitation, stimulated Raman scattering and coherent anti-Stokes Raman scattering with a single broadband laser source are demonstrated in this dissertation. Pulse shaping is used to achieve a fast and robust approach to measure the two-photon excitation spectrum from fluorescent molecules, which provide important information for

two-photon biological imaging. The selective excitation concept is also applied in the field of remote chemical identification. Detection of characteristic Raman lines for several chemicals using a single beam coherent anti-Stokes Raman scattering spectroscopy from a 12 meter standoff distance is shown, providing a promising approach to standoff detection of chemicals, hazardous contaminations, and explosives.

Yaping

ACKNOWLEDGEMENTS

Within my past five-year graduate studies at Michigan State University, lots of people at the Department of Chemistry provided me their cooperation and support which are highly appreciated. I thank them all.

I am thankful to the members of my committee, Profs. Warren Beck, Katharine Hunt and James McCusker, who provide me their time, advise and support. I would also like to thank the past and present members in Dantus research group: Dr. Vadim Lozovoy, Dr. Igor Pastirk, Dr. Matthew Comstock, Dr. Tissa Gunaratne, Dr. D. Ahmasi Harris, Dr. Johanna Dela Cruz, Dr. Haowen Li, Dr. Peng Xi, Dr. Dmitry Pestov, Jess Gunn, Xin Zhu, Yves Coello, Tricia Miller, Paul Wrzesinski, Lindsey Weisel, Yair Andegeko and Janelle Shane. Especially, I would like to thank Dr. Vadim Lozovoy who offered me numerous great research ideas and inspiration. Many thanks to Dr. Dmitry Pestov, Yves Coello and Paul Wrzesinski for reading drafts of this dissertation and making suggestions.

Thanks for Department of Chemistry, James L. Dye Endowed Fellowship and National Science Foundation for supporting me so that I could accomplish my graduate research. Thanks to College of Natural Sciences for dissertation completion fellowship that helps me complete the dissertation financially.

I would particularly like to thank my advisor, Prof. Marcos Dantus, who led me into the intriguing world of laser control and always provided support and ideas professionally and personally throughout my whole graduate studies.

TABLE OF CONTENTS

LIST OF TABLES

LIST OF FIGURES

KEY TO ACRONYMS/ABBREVIATIONS

AOM	Acoustic optical modulator
APD	Avalanche photon diode
BBO	Barium borate
BP	Binary phase
BPS	Binary phase shaping
CARS	Coherent anti-Stokes Raman scattering
CPA	Chirped pulse amplification
CR	Contrast ratio
CW	Continuous wave
DCM	Double-chirped mirrors
FROG	Frequency resolved optical gating
GA	Genetic algorithms
GDD	Group delay dispersion
GVD	Group velocity dispersion
HPTS	8-hydroxypyrene-1,3,6-trisulfonic acid
HR	High reflecting
KDP	Potassium dideuterium phosphate
KLM	Kerr lens Mode-locking
LC	Liquid crystal
MII	Multiphoton intrapulse interference
MIIPS	Multiphoton intrapulse interference phase scan
M-SPIDER	Modified spectral phase interferometry for direct electric-field reconstruction
NA	Numerical aperture
Nd:YLF	Neodymium:lithium floride
Nd:YVO4	Neodymium:yttrium vanadate
NLO	Nonlinear optical
NOPA	noncollinear optical parametric amplifier
P&A	Phase and amplitude
SHG	Second harmonic generation
SLM	Spatial light modulator
S/N	Signal to noise ratio
SPIDER	Spectral phase interferometry for direct electric-field reconstruction
SRS	Stimulated Raman scattering
Ti:Sa	Titanium:sapphire
TL	Transform-limited
TOD	Third-order dispersion

TPA	Two-photon absorption
TPE	Two-photon excitation
TPEF	Two-photon excited fluorescence
TPFM	Two-photon fluorescence microscopy

Introduction

When I first joined Professor Dantus research group in 2003 and started using the femtosecond (1fs $=10^{-15}$ s) laser as a research tool, a dream (or question) started to build in my mind: can a femtosecond laser become the ultimate automated photonic tool for every field? For example, could a doctor uses a laser as an accurate diagnostic tool or treatment of diseases, and a soldier use a similar laser as a remote detection tool for hazardous materials? In each case, all they need to do is simply turn on the laser and press a button. The computer software and hardware integration, makes it as easy as using a laser pointer, eliminating the need for a laser expert. This may sound bizarre and implausible, however, this scenario will be possible if there is a broadband laser that can cover all the molecular excitations and if one can "teach" such a laser to identify molecules. This dissertation focuses on this pursuit of transforming cutting-edge laser and spectroscopic technology into a multi-purpose and automated tool that uses tailored laser pulses. This instrument could benefit research in a wide range of fields, such as laser control of chemical reaction, functional imaging, attosecond technology, high harmonic generation, control of nanoscale systems, etc. On the other hand, this multi-purpose tool can be directly used as an analytical tool for remote molecular sensing and identification and as a spectroscopic tool for biologists to study different fluorophores.

Femtosecond laser are able to produce pulses with an extremely short time duration that allows one to monitor and tailor chemical reactions in real time. On the

other hand, it also has a very broad range of phase-locked spectral components that can be treated as a coherent superposition of millions of monochromatic light waves. An octave spanning femtosecond laser source (<2.8 fs) would cover all the optical frequency range through different nonlinear optical (NLO) processes. However, since such a light source would excite all the molecular transitions, the selectivity is lost. Consequently, such a laser source cannot be used to study a certain interesting transition or access specific fingerprint transitions to identify molecules. Fortunately, by controlling the phase, amplitude and/or polarization, which is commonly referred as pulse shaping, one can use the laser source to control the outcome of the NLO processes, accomplish transitions selectively and then ultimately teach the laser to identify molecules. Therefore, the key to this research project is coherent laser control of molecular transitions through multiphoton processes.

The advances in the field of coherent laser control have been stimulated by the pursuit of controlling chemical reaction, or to a greater extent, controlling the light-matter interaction. In 1980, Nobel Prize laureate Ahmed Zewail[1] suggested using femtosecond laser pulses to control a chemical reaction, taking advantage of the ultrafast time scale during which the energy from the light cannot be redistributed throughout the system as fast. Soon after, Warren and Zewail published a series of papers about using shaped femtosecond pulses to demonstrate the photon echo response in the iodine molecule.[2-7] This very interesting science was very difficult to perform due to the difficulties associated with the laser source. However, the invention of the self-mode-locked Titanium:sapphire (Ti:Sa) laser[8, 9] in 1990,

provided a laser system with long-term stability, largely enhanced advances in the field of laser control of chemical reactions. A number of significant results have been published and been reviewed extensively.[10-21]

The first NLO process was observed in 1961,[22, 23] soon after the invention of the laser.[24] , However, the concept that an atom or a molecule could absorb two photons simultaneously had been predicted substantially earlier by Maria Goppert-Mayer in 1931.[25] More than 20 years after the start of the NLO field, Warren first proposed to use shaped pulses in NLO application in a theoretical paper published in 1984.[26] Three years later, Warren et al experimentally demonstrated[6] the effect of pulse shaping of a nanosecond laser pulse on the yield of induced nonlinear fluorescence for the iodine molecule. In the early 1990's Weiner and Nelson published a breakthrough paper on selectively driving different vibrational modes of an alpha-perylene molecular crystal through multi-pulse impulsive stimulated Raman scattering (SRS).[27, 28] In that experiment, they used a phase-only pulse shaper with an etched mask to generate a train of pulses. Amplitude shaping of the pulse was applied a few years later by Broers to demonstrate the spectral focusing of second harmonic generation (SHG) and two-photon absorption (TPA) of Rydberg states in Rubiduim.[29-31]

After the first prediction that optimization of a chemical product was possible through multiphoton processes by Tannor, Kosloff and Rice[32, 33], Judson and Rabitz made a ground-breaking suggestion[34] in 1992 to use the computer learning algorithms or genetic algorithms (GA) to optimize the phase and amplitude of the laser pulses to achieve a desired outcome of an optical process based on feedback, even without

knowing the Hamiltonian of the system. This proposal inspired various research projects and led to the first experimental implementation in control of energy transfer in a molecular system by Warren et al in 1997.[35] Since then, control of different NLO processes using GA has been reported extensively, including optimizing the SHG output for different femtosecond laser sources with various pulse shaping devices[36-45], control of the yield of chemical reactions[46-52], TPA in isolated atoms[53-55] or solutions[56, 57], energy transfer and distribution in small molecules[58-61], polymers[62] and bio-molecular complexes[63], four-wave mixing[64], high harmonic generation[65] and other NLO processes[66-70].

In 1998, Silberberg et al demonstrated that phase-shaped femtosecond pulses can control TPA in Cesium atoms[71] They also found that as a π spectral phase step was scanned across the spectrum of the pulse, a dramatic increase of TPA occurred when the π spectral phase step was at the center of the spectrum where the Cesium atom has a sharp resonance.[72] However, this sharp resonance effect deteriorated for large molecules in solution, when the TPA was broadband.

Inspired by the work of Silberberg, the Dantus group started to investigate how to control the multiphoton excitation of large organic molecules in solution with shaped femtosecond laser pulses. A new approach to laser control called multiphoton intrapulse interference (MII) was demonstrated by using a sinusoidal function that caused the interference between frequency pairs within the bandwidth of the pulse during multiphoton excitations.[73, 74] Binary phase shaping (BPS) for MII was also introduced to the pulses for different applications.[75, 76] One of the most important

applications of MII, which already has achieved commercialization, is the use a well-known reference phase to measure and correct the spectral phase distortion that the femtosecond pulses accumulate as they transmit through or reflect from any dispersive medium. This idea[77] was conceived in 2002 and forms a solid base for this dissertation.

In this dissertation, Chapter 1 discusses the fundamental principles that form the scientific basis for all the projects, while Chapter 2 presents the major experimental tools used throughout this research. Chapter 3 discusses in detail the spectral phase measurement and correction method based on MII, including a quantitative analysis of this technique and Chapter 4 presents several experimental applications of this technique, including the control of quasi-octave-spanning laser sources. The last chapter describes how selective two-photon, SRS and coherent anti-Stokes Raman scattering (CARS) can be achieved with a single shaped femtosecond laser source. The content of the dissertation is probably only a very small step towards our ultimate goal, but still this step brings us closer to realizing the dream.

Chapter 1

Principles

Femtosecond pulses consist of a large number of phase-locked frequency components. The relative phases of each of the frequency components can be altered, and the control over the amplitude and phase of different frequency components is usually referred to as pulse shaping. The methodology for pulse shaping, where arbitrary phase control is possible for each frequency within the bandwidth of the laser pulse, was developed over 20 years ago due to its potential in telecommunications.[78] Modern pulse shapers have been available for over a decade.[79]

By appropriately manipulating the spectral phase of an ultrashort excitation pulse, one can readily control ground state and excited state molecular dynamics, or cause chemically selective molecular excitation. Gerber, et al showed that adaptive femtosecond pulse shaping could be used to selectively excite one specific molecule without disturbing another.[56] This experiment was carried out in two different containers with solutions of distinct electronically and structurally complex dye molecules. Differences in the signals from each container were recorded.

In the Dantus group, a MII method has been used for coherent control (by either enhancing or suppressing) multi-photon transitions. This method is based on intrapulse interference, which takes place within the ultrashort laser pulse spectrum during a multiphoton process. In this chapter, I will discuss in detail the MII theory,

the phase control of the pulses, and the specific phase shaping that used throughout this dissertation, where the spectral phase function takes only values of 0 and π.

1.1. Mulitphoton intrapulse interference theory

A single multiphoton transition simultaneously involves several photons with only a fraction of the transition energy (e.g., 1/2 for a two-photon or 1/3 for a three-photon process). Some of the constraints are the number of photons (two, three, four, etc.) and energy conservation, meaning that the sum of photon energies should be equal to the transition energy. Because the large bandwidth of the femtosecond pulses allows different combinations for a certain transition, the final transition probability depends on the inference of all pathways. Broers showed that eliminating the interfering frequencies changed the NLO outcome.[29]

It has long been known that the NLO processes are sensitive to the spectral phase of the laser pulses.[20] For example, Silberberg [71, 72] used a step phase function, scanned across the laser pulse spectrum, to demonstrate a sharp dependence on the phase of two-photon absorption in Cesium atom. The effect, however, was not observed when samples have broadband absorption, as large molecules in solution do. The Dantus group was motivated by Silberberg's work and started to explore the condition of the laser control for multiphoton transition of large molecules in solution in 2001. The first demonstration of MII[73, 74] was soon published in 2002. In these multiphoton excitation experiments, a sinusoidal spectral phase function was used to cause MII to control the multiphoton excitation of the large molecules including proteins in solution, and to manipulate two-photon versus three-photon transitions. MII also

showed the potential to enhance the amplitude of the nonlinear field at specific frequency and suppress the nonlinear field amplitude elsewhere, i.e., to achieve the selective molecular excitation. The demonstrated selective two-photon excitation using MII relied on utilizing the difference in two-photon excitation cross sections of different molecules or effect of different micro-chemical environment, e.g. different pH values in solution, which change the properties of sensitive chromophores.[80] A new functional imaging method in two-photon microscopy based on MII was also introduced.[81, 82]

To understand how MII works, one can consider a two-photon process such as SHG. For the fundamental pulse (excitation pulse) centered at ω_0, the maximum SHG will take place at $2\omega_0$. However, the intensity of the SHG at $2\omega_0$ depends on not only the field intensity at ω_0, but on the entire bandwidth of the pulse according to:

$$S^{(2)}(2\omega) \propto \left| \int \left| E_0(\omega+\Omega) \right| \left| E_0(\omega-\Omega) \right| \exp\left[i\left(\varphi(\omega+\Omega) + \varphi(\omega-\Omega) \right) \right] d\Omega \right|^2 \quad (1.1)$$

where $\omega+\Omega$ and $\omega-\Omega$ refer to blue- and red-shifted frequencies, respectively. As illustrated in Fig. 1.1(a), when the spectrum of the pulse is broad, the photons at the frequency $\omega_0+\Omega$ combine with the photons with frequency at $\omega_0-\Omega$ to result in the transition at frequency $2\omega_0$. When the transition is not at the center of the excitation pulse, as shown in Fig. 1.1(b), the photons at the frequency $\omega_0-\Delta/2+\Omega$ paired with photon at the frequency $\omega_0-\Delta/2-\Omega$ will cause the transition at $2\omega_0-\Delta$. Note that the photons at frequencies in the white area of the spectrum do not contribute to this transition because no photons at the lower frequency ($-\Omega$) side of spectrum can pair with those photons.

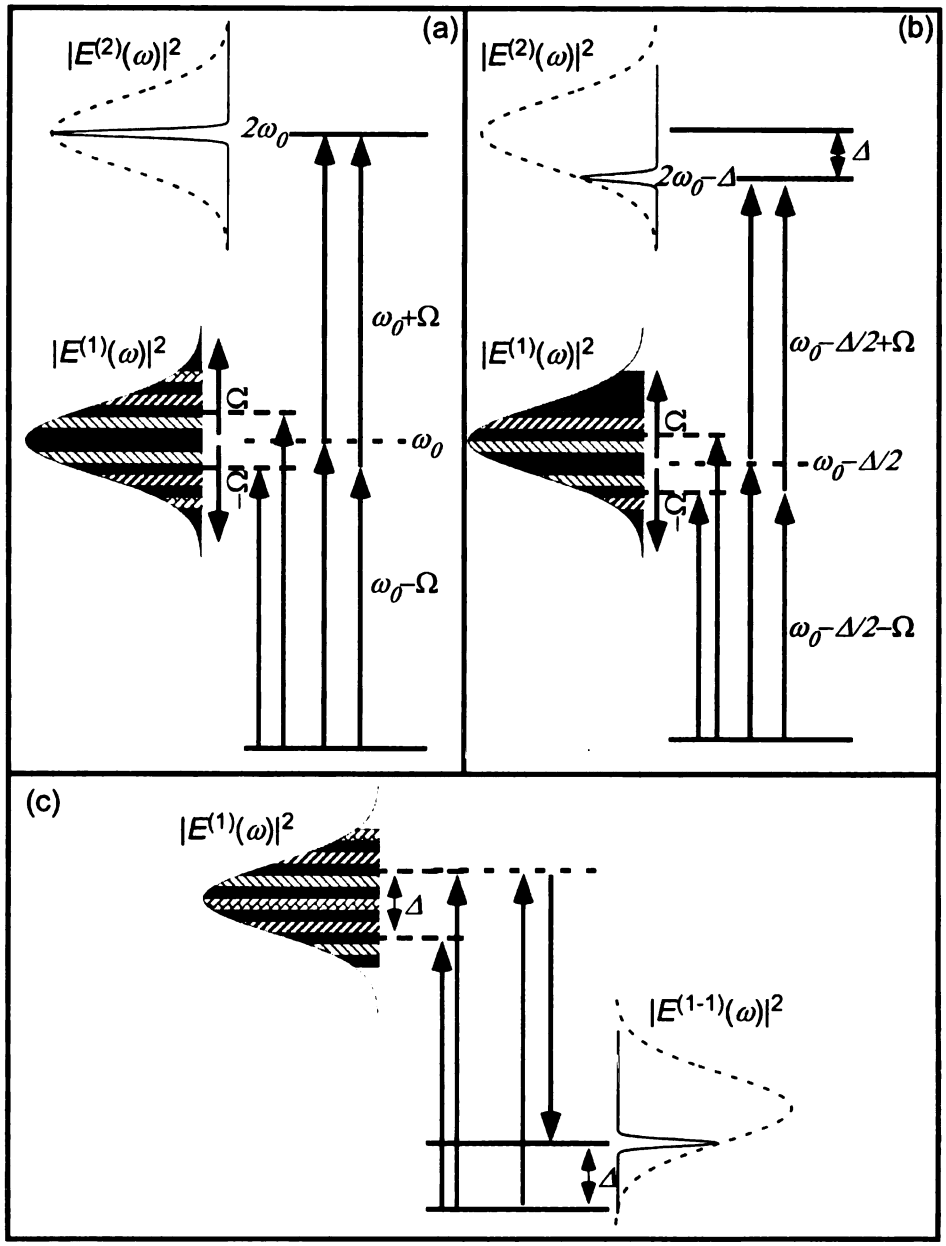

Fig. 1.1. The concept of MII. (a) shows that when the two-photon transition is at the center of the spectrum, the photons at the frequency $\omega_0+\Omega$ combine with the photons at frequency $\omega_0-\Omega$ to result in the transition at frequency $2\omega_0$. All possible frequency pairs contribute. When all frequency pairs add up constructively, the intense peak at $2\omega_0$ appears. (b) shows that when the two-photon transition is not at the center of the spectrum, i.e., at $2\omega_0-\Delta$, the photons at the frequency $\omega_0-\Delta/2+\Omega$ paired with the photons at the frequency $\omega_0-\Delta/2-\Omega$ will cause the transition at $2\omega_0-\Delta$. (a) and (b) show how MII works for large molecules that have broadband transition. (c) shows how MII works for stimulated Raman transitions. The pump photons at frequency $\omega_0+\Delta+\Omega$ will work with the Stokes photons at frequency $-(\omega_0+\Omega)$ to excite the transition at Δ. In all panels, the frequency pairs are shown in same patterns.

Fig 1.1(c) illustrates the case of a stimulated Raman transition, where the pump photons at frequency $\omega_0+\Delta+\Omega$ will work with the Stokes photons at frequency $-(\omega_0+\Omega)$ to excite the transition at Δ in frequency or $\Delta/2\pi c$ in wavenumber units. For all of the cases, the transition intensity depends on the sum over all possible Ω values.

All three words in the definition of MII are essential. First, it occurs only when spectrally-broad pulses induce a multiphoton transition. Second, the interference happens within the bandwidth of the pulse, i.e., different part of the pulses or photons with different frequencies interfere with each other. Third, the interference is over all the possible pathways Ω, or in other words, involves all the frequency pairs. To control the outcome of multiphoton transitions, one can change the spectral phase of the pulse or mathematically speaking, the phase term in the bracket of Eq. (1.1), to control the intrapulse interference condition and ultimately control the multiphoton processes.

1.2. Effect of spectral phase on NLO processes

According to Eq. (1.1), when transform-limited (TL) pulses, i.e. pulses with a constant phase across the spectrum, are used for SHG, the SHG reaches its maximum at each frequency since the exponential term is the same for all the frequency. Consequently, selectivity is lost, and so is the control over the SHG. This is true for all the NLO processes, under the condition that the system has no intermediate resonances, and that the system is interrogated under the weak field regime.

One possible way to regain the selectivity is through amplitude shaping, i.e.

modification of the amplitude of the laser spectrum. One can use an amplitude mask that only allows a small portion of the spectrum transmit through, as shown in Fig. 1.2(a). Although this method works well for selective excitation (Fig. 1.2(b)), the efficiency is very low[75] since most of the photons that would contribute to this transition are lost during the process. Note that the intensity of each peak in Fig. 1.2(b) obtained with amplitude-only shaping is multiplied by 50 to be on the same scale: the actual intensity is very small compared with TL excitation where no photon is lost.

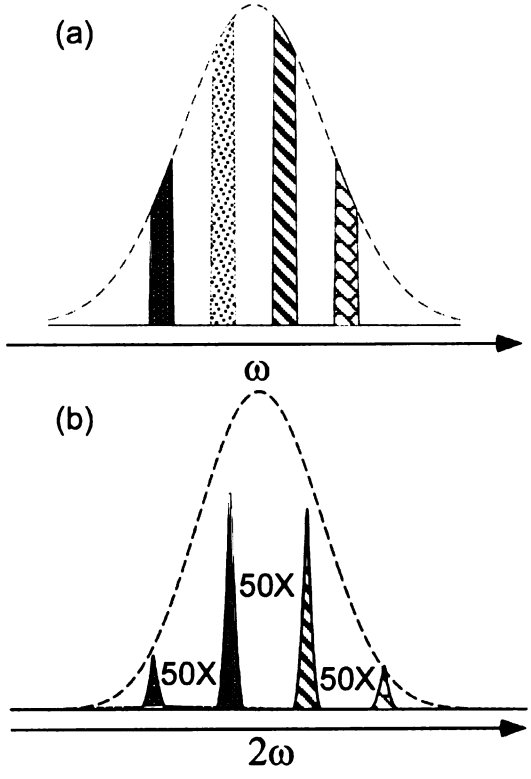

Fig. 1.2. Effect of amplitude-only shaping on SHG. (a) represents that only a small portion of the spectrum transmits for each amplitude mask. The dashed line illustrates the original spectrum. (b) shows the calculated SHG spectrum for each amplitude mask. The dashed line demonstrates the calculated SHG spectrum for a TL excitation pulse. Note that the intensity of the SHG spectra resulting from the amplitude shaping is scaled by a factor of 50: the actual intensity is very small compared with TL excitation where no photon is lost.

Spectral phase shaping of the pulses is a much more efficient approach. The

simulation using a Gaussian excitation pulse in Fig. 1.3 illustrates how the SHG spectra depend on the spectral phase. A linear phase function clearly has no effect on the NLO spectrum (Fig 1.3 (a)). Quadratic phase function (chirp) changes the intensity of the SHG spectrum without affecting the shape; furthermore, the SHG spectrum is not sensitive to the sign or center of the quadratic phase function (Fig 1.3(b)). Cubic phase function has a significant effect on the shape of the NLO spectra (Fig. 1.3(c)). It generates a maximum at the symmetry point of the cubic function that reaches the TL excitation intensity. Cubic phase is relatively good for selective NLO excitation although there is still some unwanted background on other frequencies. Besides, because of the cubic dependence on the frequency, the value of the cubic phase may be very large at the edge of the spectrum, making it relatively difficult to implement via available pulse shaping devices in a real experiment. Figs. 1.3(d), (e) and (f) illustrate how sinusoidal phase modulation changes the NLO spectra. Compared with the cubic phase function, the sinusoidal phase function is limited to a certain range so it does not diverge toward infinity at the edges of the spectrum as a cubic phase function does. In addition, the Taylor series expansion of the sinusoidal function contains a cubic frequency dependence term that would produce selectivity. As expected, a single period of the sinusoidal phase function generates a maximum around the inversion point. However, the peak feature is relatively broad and a large background at other frequencies is still present (Fig. 1.3(d)). The amplitude of the sinusoidal phase function is one parameter to be adjusted. As shown in Fig. 1.3(e), the five times increase of the amplitude makes the SHG peak narrower, compared with

that in Fig. 1.3 (d). The background at undesired frequencies still exits. Another parameter to be adjusted is the period of the sinusoidal function. As it increases (Fig. 1.3(f)), the SHG peaks also get narrower: however, multiple peaks appear as more than one inversion point exists in the spectral phase function within the pulse spectral bandwidth.

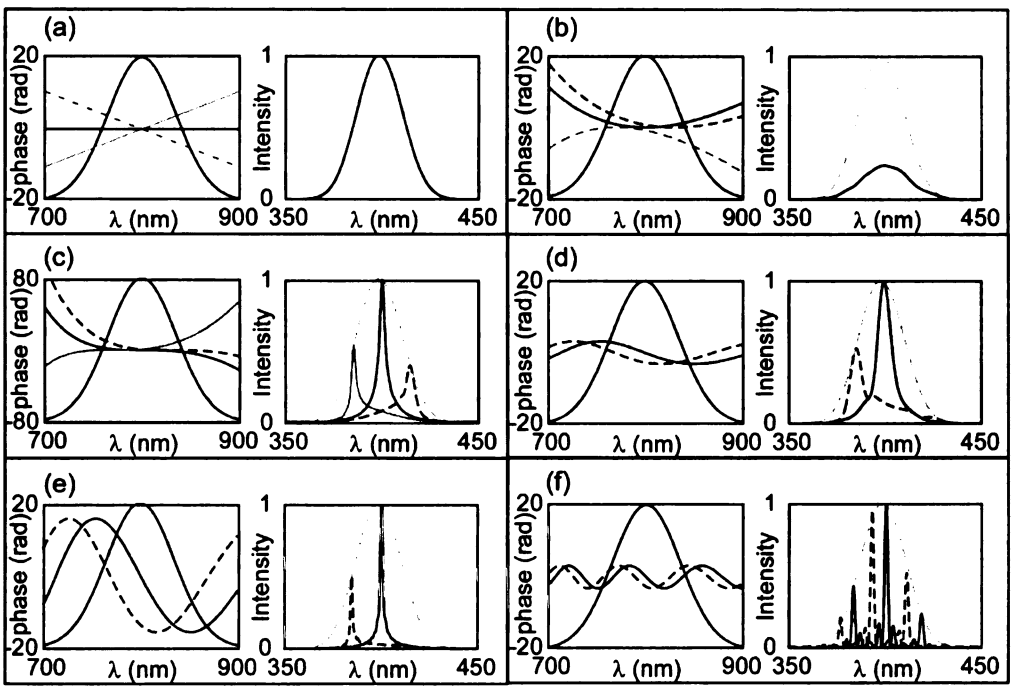

Fig. 1.3. Effect of phase shaping on SHG. In all panels, the left graph illustrates the fundamental spectrum of the excitation pulses and the applied phases, while the right graph shows the corresponding SHG spectra with gray dashed line representing the TL SHG spectrum. Panels (a), (b) and (c) illustrate the effect of three linear, quadratic and cubic phase functions on SHG, respectively. Panels (d), (e) and (f) show the effect of different sinusoidal functions on SHG.

The simulations shown in Fig. 1.3 demonstrate that the spectral phase of the excitation pulses has a critical effect on the outcome of NLO processes, in this case the SHG spectrum. Similarly, the spectral phase distortion that the laser pulses accumulate through propagation in or reflection from any dispersive medium, including the various optical components and even air, has a significant effect on the

outcome of the NLO process. In order to achieve robust and reproducible control over NLO processes, such phase distortion must be measured and corrected at the sample in the first place. The accurate phase measurements throughout this dissertation were accomplished with a method[77] based on MII. In such a method, a well-known reference phase function is used to measure the unknown phase distortion of the pulse. Correction of the spectral phase distortions serves as the base for the accurate phase shaping that has been utilized for all the applications in this dissertation. The details of this method and its quantitative analysis will be discussed in Chapter 3.

Although none of the phase modulation functions in Fig. 1.3 gives optimum selectivity, they allowed us to identify some characteristics of the phase that are needed. First, the phase requires a non-constant second derivative, in other words, the phase must have at least a third-order dependence term on the frequency. Second, the phase function requires a specific symmetry. Third, the phase function should not diverge with increasing or decreasing frequency for easy experimental implementation. While there may be numerous phase functions that satisfy these criteria, an exhaustive search through all possible functions would take impractically long time. One could use random arbitrary shaping to achieve some level of selectivity, but the resulting amplitude at the desired frequency is not very high.[20]. Therefore, instead of arbitrary phase shaping, we went back to Eq. (1.1) and found a different phase shaping approach discussed next.

1.3. Binary phase shaping

A closer look at the exponential term or rather the phase-dependent term in Eq. (1.1)reveals that by setting the phase values to only 0 or π (Fig 1.4(a)), the contribution from each photon pair ($\omega+\Omega$ and $\omega-\Omega$) is restricted to 1 or -1, respectively, assuming that the spectral amplitude of the excitation pulse is constant. With these two values, it is relatively easy to design phases where the sum is maximized for a target transition frequency and zero otherwise. Such binary phase (BP) functions with values only 0 or π are the most efficient approach we have found to achieve selectivity. Fig. 1.4(b) is an experimental demonstration of selective SHG excitation via BPS.

Compared with arbitrary phase shaping, BPS greatly reduces the number of possible different phase functions that need to be tested for selective excitation without discarding all the optimal solutions. For example, if there are 100 pixels that can take 1000 different phase values to achieve selective excitation through phase shaping of the pulses, the number of all possible phase combinations is $(1000)^{100}=10^{300}$. This number is so larger, that it is hard to understand. For example, the number of atoms in the universe is estimated at 10^{79}. It would take longer than the life of the universe to test even a small fraction of the possible arbitrary phase functions. This number will be even larger if amplitude modulation is also considered. On the other hand, using BPS the number of different phases quickly reduces to $2^{100}\cong10^{30}$, and if symmetry constraints are applied, the number of phases can be further reduced to $2^{50}\cong10^{15}$, a number significantly smaller than 10^{300}. Further

reductions are possible as will be illustrated further.

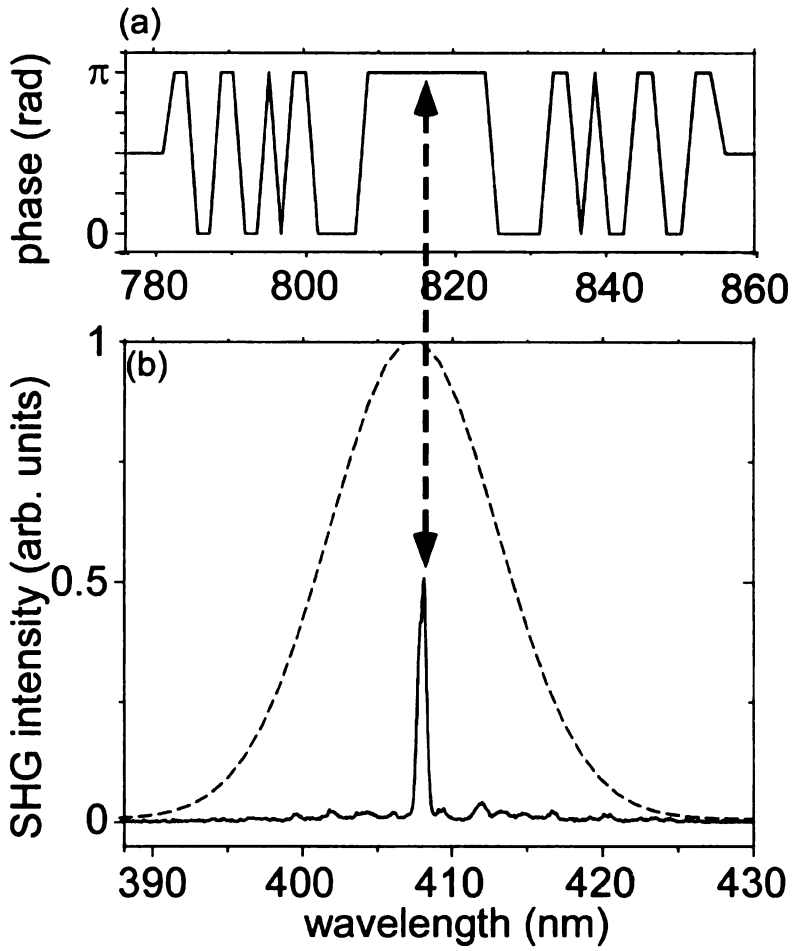

Fig. 1.4. BPS and its effect on NLO processes. (a) shows a BP function with reflection symmetry. (b) illustrates the experimental SHG spectrum (solid line) for the BP function shown in panel (a), giving very good selectivity. The dashed lines show the SHG spectrum for TL pulse. Note that the maximum appears at the symmetry point of the BP function.

The Dantus group first demonstrated the use of prime-number inspired BPS to generate selective SHG excitation in 2004.[75] Following that, BPS has been applied in different fields, e.g., to achieve functional imaging through 1 mm biological tissue,[82] to realize the multidimensional chemical recognition through laser controlled mass spectroscopy[83-88] and to control other spectroscopic technique.[89] In Chapter 5, I will discuss how to use the number theory to generate the optimized BP analytically for

selective SHG and SRS and its applications in two-photon excitation (TPE) and CARS spectroscopy.

Chapter 2

Experimental Tools

2.1 Laser System

The first lasers capable of producing sub-picosecond pulses were developed in the early 1980's[90-93]. Those ultrafast laser systems were dye-based lasers and were generally home-built and relatively large and unreliable. Over the last three decades, the duration of the pulses was significantly reduced (pulses as short as 2.8 fs laser were generated[94]) and some systems have become as compact as the human hand (e.g. the fifth laser system I will describe later). The experiments presented in this dissertation were performed on five different femtosecond laser systems in Professor Dantus's laboratory at Michigan State University.

The first system was a Ti:Sa oscillator system (Kapteyn-Murnane Labs) pumped by a neodymium:yttrium vanadate ($Nd:YVO_4$) laser (Spectra Physics: Millennia V). It generates sub-12 fs pulses (110 nm FWHM) centered near 800 nm, with a repetition frequency of 87 MHz. The average output power is 250 mW. Most of the experiments presented in Chapter 3, experiments presented in sections 4.2 and 5.1 in were accomplished with this laser system.

The second laser source was a regeneratively amplified Ti:Sa laser system which delivers 40 fs pulses centered at 800nm, with 0.7 μJ per pulse at 1kHz repetition rate. In this system, the output of a femtosecond Ti:Sa oscillator (Kapteyn-Murnane Labs), which is pumped by a $Nd:YVO_4$ laser (Spectra Physics: Millennia) and capable of producing ~15 fs pulses centered at 800 with 80 MHz repetition rate, is amplified by a

regenerative amplifier (Spectra Physics Spitfire) pumped by a 1kHz neodymium:lithium floride (Nd:YLF) laser (Spectra Physics: Evolution X). A portion of experiments described in Chapter 3 involved this system.

The third laser is a Ti:Sa oscillator with chirped mirror technology. The oscillator (Nanolayers GmbH: Venteon Pulse 1), pumped by a Nd:YVO_4 laser (Coherent: Verdi-5), generates an ultra-broadband spectrum spanning over more than 400 nm (from 620 to1050 nm). The corresponding 4.3 fs pulses have ~1 nJ energy per pulse with a repetition rate at 78 MHz. The laser system was involved in the experiments in sections 3.3, 4.1.1 and 5.2.

Experiments described in sections 4.1.2 and 5.3 were performed with a home-built continuum generation system. In this system, ~20 fs laser pulses from a Ti:Sa oscillator (Coherent: Micra), are amplified by a regenerative amplifier (Legend USP, Coherent) and then focused into an argon-filled hollow waveguide which generates sub-5 fs pulses with 0.2 μJ energy per pulse. The broad bandwidth and high energy of the system are ideal for CARS spectroscopy at remote distance.

Finally, the fifth laser, utilized for experiments discussed in section 4.1.3, is a home-built Ti:Sa oscillator with ring-bow tie geometry from Professor Cruz group (University of Campinas, Brazil). The extremely small cavity size provides a repetition rate of 2.12 GHz.

Overall, the first two laser systems are used to prove the concepts of phase control and selective excitation. Using the phase control and selective excitation methods, applications of the universal laser source are explored on the last three

systems. A substantial part of my work in this dissertation involved construction, maintenance and characterization of the laser system and various experimental setups. Each laser system described above was equipped with one dual mask pulse shaper. The only exception was the fourth system, which has two pulse shapers: one phase-only pulse shaper in between the Micra oscillator and the Legend USP amplifier, and one for the pulses after the argon-filled hollow waveguide. The details of pulse shaper layout including optical setups of the pulse shapers for different laser system are discussed later in this chapter. All the applied experimental setups and the corresponding detection schemes are described in later chapters, together with the experiments.

2.1.1 Ti:Sa Oscillator

Lasers with pulsed rather than continuous wave (CW) output have the advantage that a fixed amount of energy is confined in a very short time interval, resulting in the high peak power but relatively low average output power. The common scheme of a pulsed laser is shown in Fig. 2.1. It involves two mirrors to form a cavity, a gain medium in the cavity and a loss modulator for mode-locking.

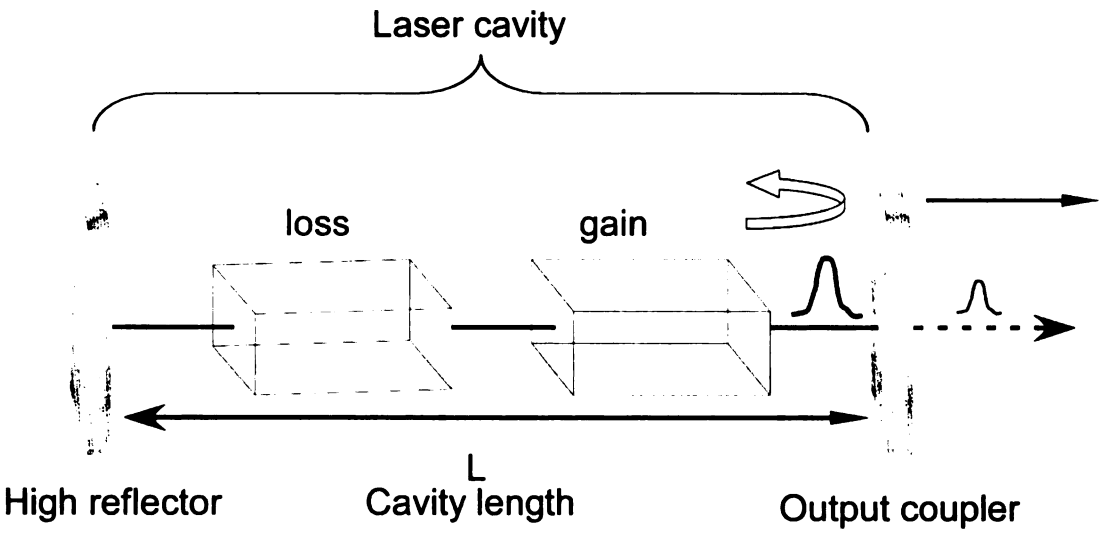

Fig. 2.1. Common cavity design for a pulsed laser. An output coupler partially transmits a small fraction of the laser pulse out of the laser cavity. The transmitted photon bursts are equally spaced by the cavity round-trip time: TR = 2L/vg, where L is the laser cavity length and vg is the pulse propagation velocity. Typically, a loss modulator (in time or spatial domain) is used to compress the laser light into short pulses around the minimum of the loss modulation.

Among all the available gain media, Titanium-doped sapphire (Ti^{3+}:Al_2O_3, usually annotated as Ti:Sa) is the most used transition-metal-doped gain medium for femtosecond solid-state lasers. It was introduced in 1986[95], and short after, the CW lasing action on Ti:Sa gain medium was demonstrated.[96] In 1990, the first sub-100 fs laser was reported by Spence and coworkers.[8, 9] Thereafter Ti:Sa lasers[97, 98] quickly replaced most dye lasers, which had previously dominated the field of ultrashort pulse generation. The Ti:Sa crystal has a typical four-level energy diagram as shown in Fig. 2.2.

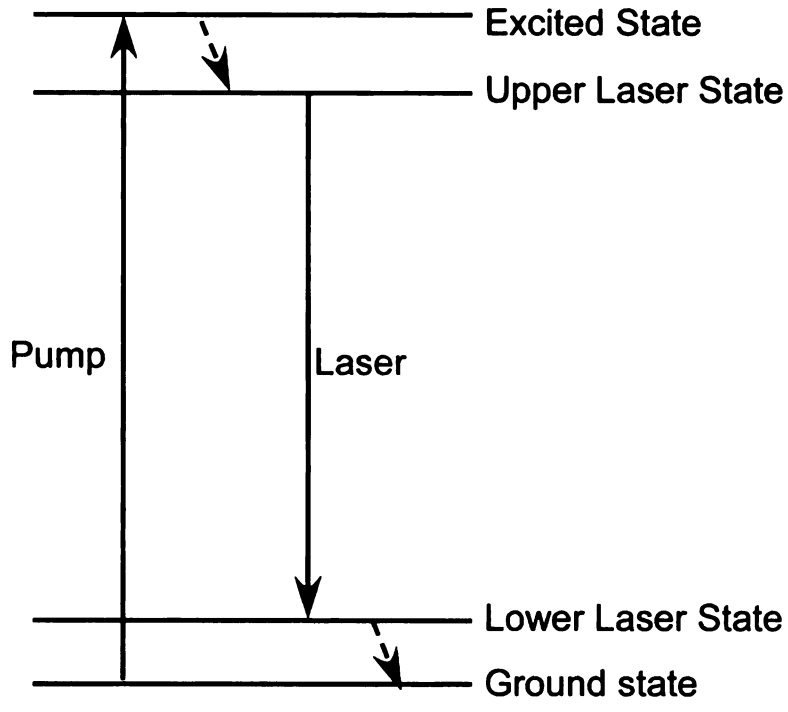

Fig. 2.2. Energy level diagram of a typical four-level gain medium. The lower laser state is well above the ground state. The pump laser excites the atoms or ions to a state higher in energy than the upper laser level. The excitation process is usually followed by a rapid non-radiative transfer of the population on the upper laser level. The upper laser state usually has a long lifetime for the spontaneous emission, i.e. the population lives long enough for stimulated emission to contribute to the gain. After the stimulated process, the population on the lower laser state quickly relaxes to ground state. Ideally, no appreciable population occurs in the lower laser state during the laser operation.

Despite the rather short lifetime for the upper laser level (3.2 μs, which implies relatively higher pump intensity), the broad gain cross-section, large energy storage density, excellent thermal conductivity and wide range of possible pump wavelengths of Ti:Sa crystal make it an exceptional gain material for femtosecond lasers and amplification systems. The maximum gain and laser efficiency is obtained at ~800 nm with very broad emission band (650 -1100 nm), making it possible to generate pulses with less than 5 fs pulse duration (the pulse duration of the Ti:Sa laser system that will be presented in section 2.1.3 is ~4.3 fs). Since the peak of the absorption band is at ~500 nm, the energy loss resulting from reabsorption of the laser radiation is also

minimized.

Generation of pulsed laser light requires so called "mode-locking" techniques. Mode-locking works in the laser cavity by insuring that the all the longitudinal modes, i.e. the frequency components of the laser spectrum, have a fixed phase relationship (see Fig.2.3.). Mode-locking techniques can be divided into two main categories: active and passive mode-locking. Active mode-locking involves a periodic modulation of the resonator losses or the round-trip phase change, achieved with an active element, e.g. an acousto-optic or electro-optic modulator.[99] When such modulation is synchronized with the cavity roundtrip, short pulses, usually with a picosecond time duration, are produced.

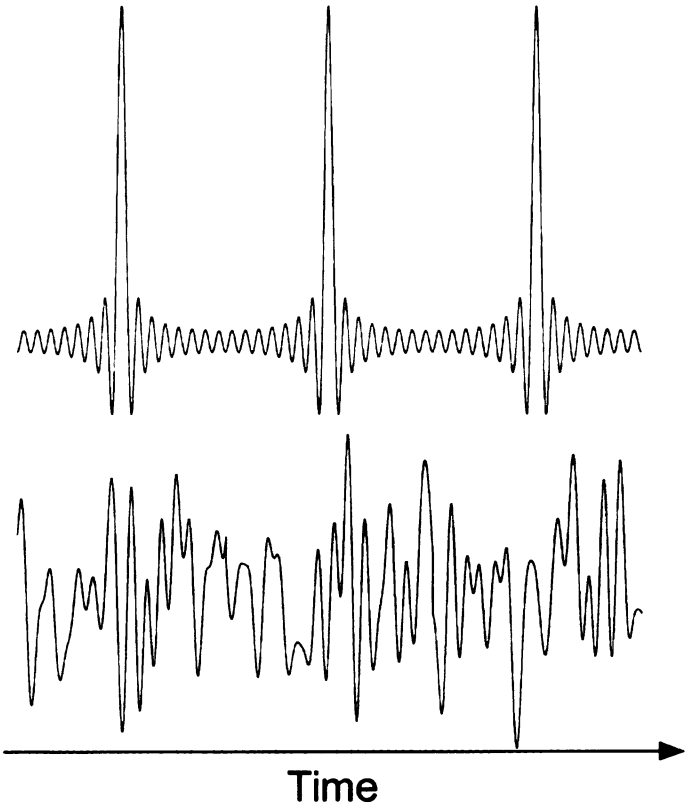

Fig. 2.3. Calculated temporal of relation of the intracavity field of the laser with 15 modes. (a) constant phase relationship (equal zero) between each mode, (b) random phase relationship between each mode.

Passive mode-locking implies the use of a nonlinear passive element inside the laser cavity, e.g. a saturable absorber, first discovered in 1972.[100] The ultrashort pulses from the cavity with a Ti:Sa crystal as the gain medium are generated from passive mode-locking, in the form of Kerr lens mode-locking (KLM). In this case, an artificial saturable absorber, rather than a real one, is created in the gain medium by the nonlinear self-focusing effect: Kerr lens effect.

This modelocking mechanism was first referred as "magic modelocking",[9] until detailed explanations were given in the following few months.[101-103] The core of the KLM is the non-linear refractive index (n_2) of the Ti:Sa crystal. The effective index of refraction of the Ti:Sa crystal can be written as $n=n_1+n_2I(r,t)$, where n_1 is the linear refractive index and $I(r,t)$ is the spatial and temporal distribution of the intensity of the laser beam. As one can see, the effective index of refraction has dependence of the distribution of the laser field intensity. Therefore, when the laser beam has a Gaussian intensity distribution as shown in Fig 2.4., the Ti:Sa crystal acts effectively as a lens. In combination with a hard aperture inside the cavity, such self-focusing effect reduces the mode area of the high intensities through the aperture and hence results in mode-locking. The KLM without an intracavity hard aperture was demonstrated later in 1993[104] and now is applied in most of commercially available Ti:Sa femtosecond lasers.

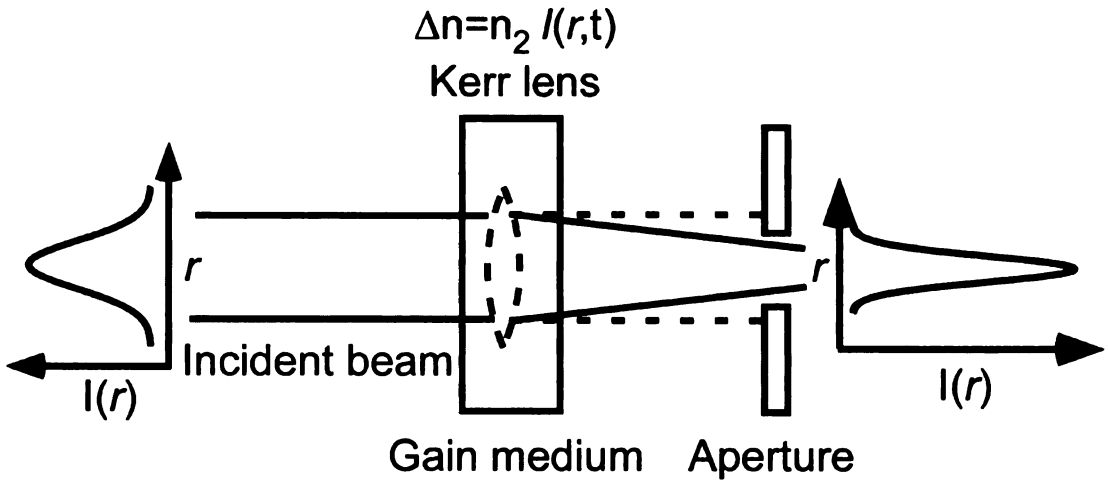

Fig. 2.4. Kerr lens effect. A nonlinear lens is formed in the central part of the beam profile, and only the modes with high intensity can pass through the aperture.

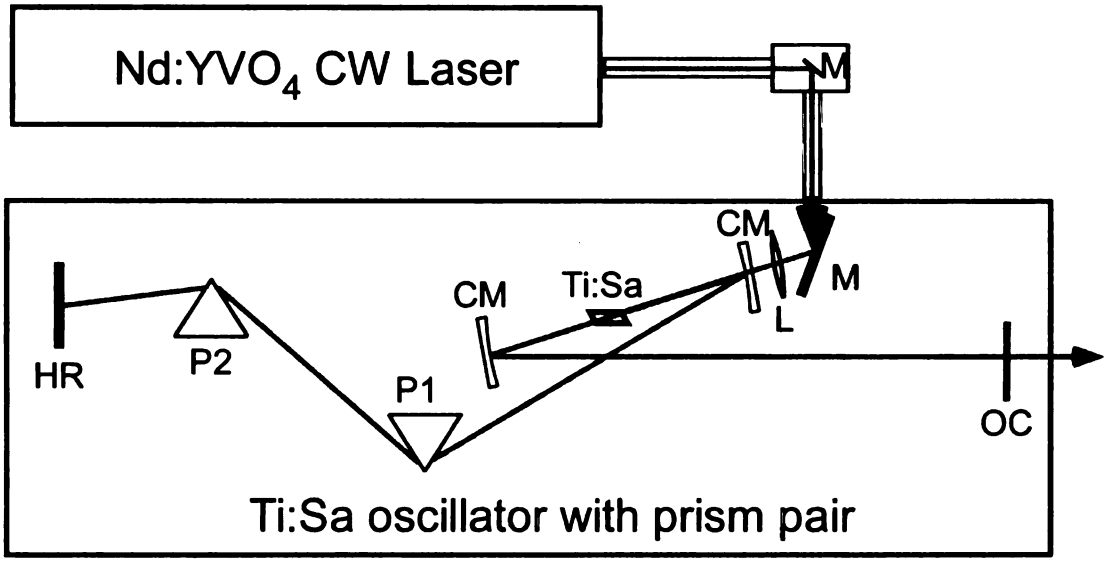

Fig. 2.5. Schematic of a typical Ti:Sa laser oscillator with an intracavity prism-pair compressor. M: mirror, L: lens, CM: curved mirror, Ti:Sa: Ti:Sa crystal, P1 and P2: prism pair, HR: high reflector and OC: output coupler.

A schematic description of a Ti:Sa laser oscillator is shown in Fig. 2.5. The successful implementation of the KLM theory and control of intracavity group velocity dispersion (GVD) through the prism pair (P1 and P2)[105, 106] result in pulses as short as 8.5 fs.[107]

2.1.2 Ti:Sa regenerative amplified system

Femtosecond pulses generated by a Ti:Sa oscillator are very suitable for weak field studies, e.g. biological imaging. However, those pulses do not provide enough energy for strong-field experiments, such as chemical bond breaking or photon-induced chemical reactions. For those applications, amplification is required to generate an output with high optical power from relatively small input optical power.

Most optical amplifiers are laser amplifiers, where the amplification is based on stimulated emission. There are also optical parametric amplifiers based on media with $\chi^{(2)}$ nonlinearity[108] or a fiber device with the $\chi^{(3)}$ nonlinearity.[109] Other types of nonlinear amplifiers include Brillouin amplifiers[110] which exploit the delayed nonlinear response of a medium and Raman amplifiers.[111] In the case of a laser amplifier, a gain medium which can be stimulated by the signal light to emit more light into the same radiation modes (either insulators doped with some laser-active ions, e.g. Ti:Sa crystal, or semiconductors, which can be electrically or optically pumped), is used.

Since such gain media tend to have lower emission cross sections, the effective gain needs to be accumulated through multiply passes of the gain medium in order to achieve the high amplification. This can be performed in three different ways: multi-pass[112, 113], regenerative[114, 115] and multi-stage amplification. Multi-pass amplification is obtained with combination of mirrors that allows the beam to pass the gain medium several times with slightly different angles (see Fig. 2.6). However, the

difficulties in alignments and lower pulse-to-pulse stability when compared with regenerative amplifiers make latter more practical. Multi-stage amplifiers, used for some special applications that will not be discussed in this thesis, are amplifier chains that provide very large amplification factors, e.g., to obtain pulses with energies on the order to Joules.

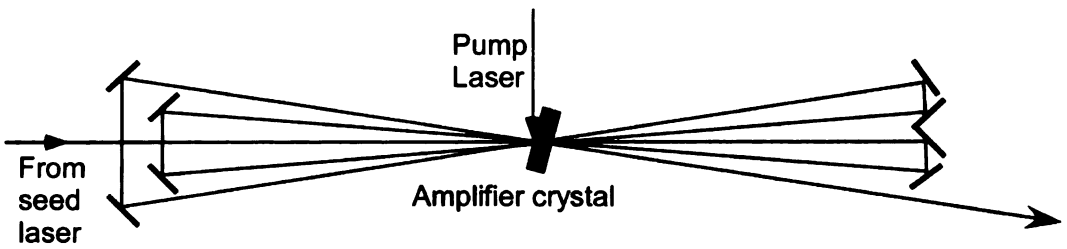

Fig. 2.6. Multi-pass amplifiers. The combination of the mirrors allows the beam to pass the gain medium multiple times.

Regenerative amplifiers achieve multiple passes of the gain medium with a cavity containing the gain medium and an optical switch including usually an electro-optic modulator (Pockels cell) and a polarizer. The number of round-trips that pulse travels through gain medium in the cavity is controlled by the optical switch. This number can be very large, leading to a very high amplification factor. The output pulse energy from a regenerative amplifier varies from several hundred miliJoules to several Joules.

In femtosecond amplifiers, some problems, e.g., nonlinear pulse distortion and damage of the gain medium and other optical elements, arise as the peak intensity of the optical pulses becomes very high during the amplification process. In 1985, Strickland and coworkers demonstrated a technique, called later chirped pulse amplification (CPA), that can effectively prevent those problems.[116-119]

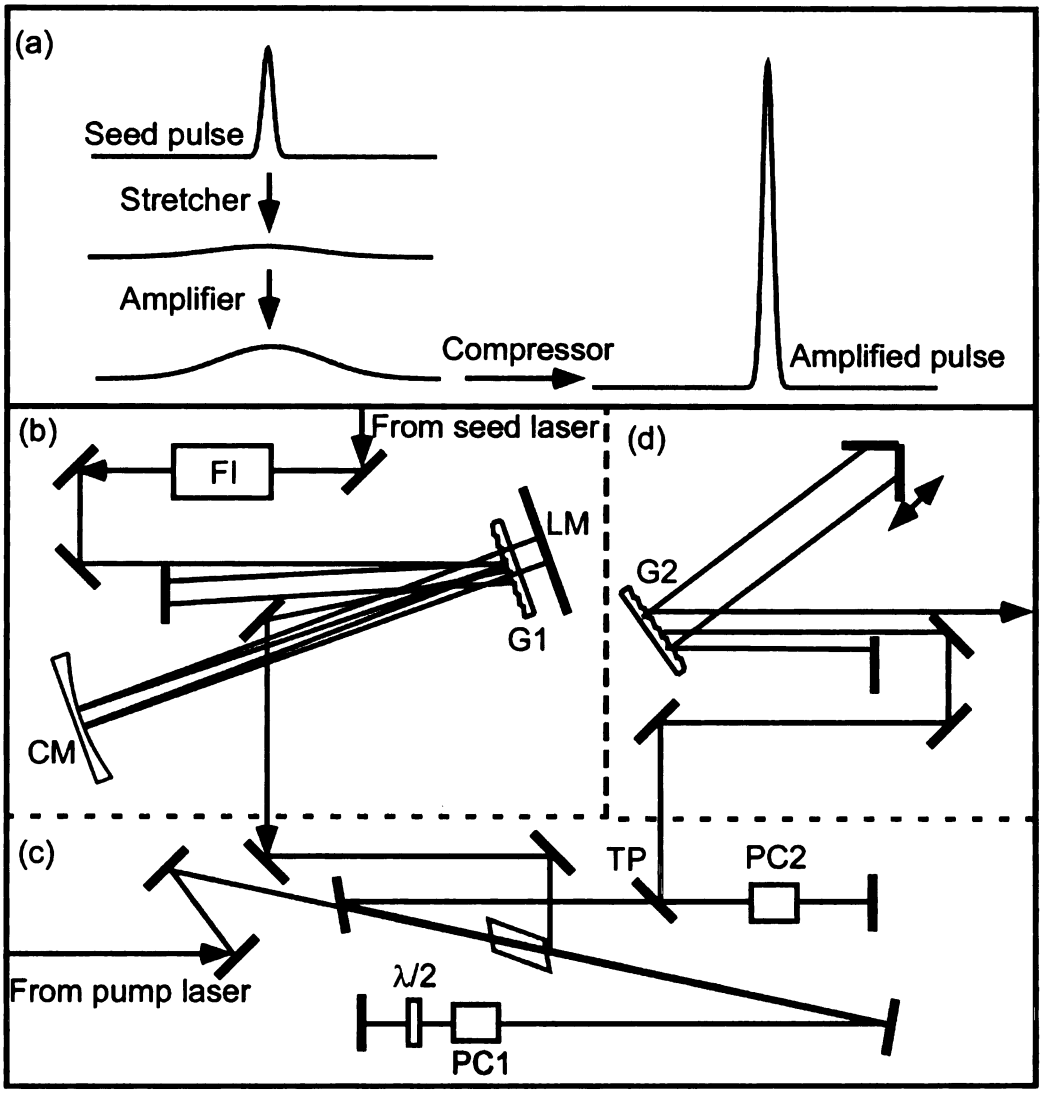

Fig. 2.7. Regenerative amplifier and CPA technique. (a) illustrates the temporal pulse shape evolution in CPA. (b), (c) and (d) illustrate the stretcher, regenerative amplifier and compressor, respectively. The combination of (a), (b) and (c) gives a full optical layout of a regenerative amplifier based on CPA. FI: Faraday isolator, G1 and G2: grating, CM: curved mirror, LM: long mirror, P: periscope, PC1 and PC2: Pockels cells, and λ/2: half-wave plate.

The idea of CPA is illustrated in Fig. 2.7(a). The seed pulses are chirped, i.e. temporally stretched to a much longer duration by highly dispersive optics, e.g., a stretcher comprising a pair of gratings (Fig. 2.7(b)), before they pass through the gain medium. The stretched pulses have significantly less peak intensity (3-5 orders of magnitude lower), and relieve the detrimental effects during amplification. The

amplified pulses are then temporally compressed to the temporal duration comparable to that of the seed pulses by removing the chirp with a grating-pair compressor (Fig. 2.7(d)) and the very high peak intensity is restored. The optical layout of a regenerative amplifier with CPA is shown in Fig. 2.7. The two amplified systems I used in this dissertation are based on the design introduced by Positive Light which first was marketed by Spectra Physics and then purchased by Coherent. The models names are Spitfire and Coherent Legend USP, and can generate ~35 fs and ~30 fs pulses, respectively.

2.1.3 Venteon Ti:Sa Oscillator

As mentioned in section 2.1.1, the shortest pulse demonstrated while using an intracavity prism pair is as short as 8.5 fs[107]. When even shorter pulses are needed, a different scheme is required to compensate the intracavity dispersion. The new scheme involves very specially designed mirrors called double-chirped mirrors (DCM).[120, 121]

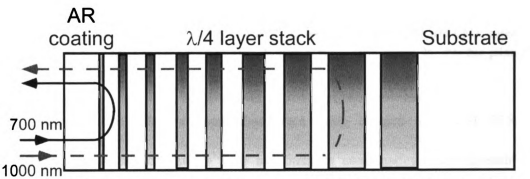

Fig. 2.8. Multi-layer structure of a typical chirped mirror. Note that 700 nm light travels much less distance than 1000 nm light does, resulting certain amount of negative chirp, i.e. shorter wavelength components of the pulses arrives earlier than longer wavelength ones. AR: anti-reflective

Chirped mirrors are composed of stacks of quarter-wave layer pairs that have

maximum reflectivity for different wavelength. Fig. 2.8 shows the structure of a typical chirped mirror: the light with shorter wavelength will be reflected by the first few layers and the light with longer wavelength will penetrate deeper and be reflected by the last few layers. Therefore, the light with shorter wavelength travels much less distance in medium than the light with longer wavelength, resulting in the negative chirp that would compensate the intracavity dispersion of the Ti:Sa oscillator. This chirped mirror idea was first demonstrated by Krausz and coworkers in 1994[122] and a 11 fs Ti:Sa oscillator[123] based on such mirrors was demonstrated. A few years later, DCMs were developed to reduce the dispersion oscillations arising from the strong index discontinuity in chirped mirrors.

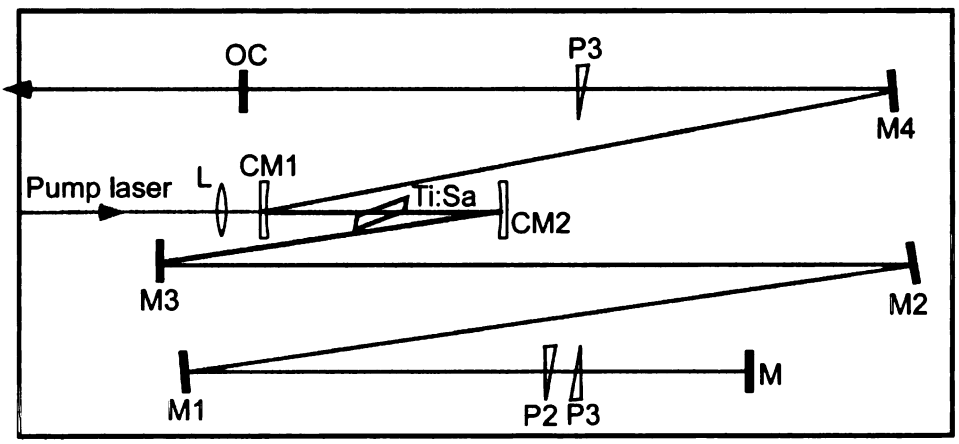

Fig. 2.9. The optical setup schematics for Venteon Ti:Sa oscillator. L:lens, CM1 and CM2: curved mirrors (DCM pair), M1,2 and M3,4: DCM pairs, M:mirror, Ti:Sa: Ti:Sa crystal, P1- P3: thin prisms and OC: output coupler.

There are two different approaches when using chirped mirrors in Ti:Sa oscillators: use them exclusively[124] or use them in combination with adjustable prisms[125, 126]. The latter allows for a continuous adjustment of intracavity dispersion through prisms, and tends to generate shorter pulses. The Venteon Ti:Sa oscillator has this configuration (see Fig. 2.9). In particular, the laser that we used has specially

coated mirrors obtained from Prof. Kaertner from MIT.

2.1.4 Continuum generation in the hollow waveguide

The femtosecond laser amplifier is able to generate pulses with very high peak power. However, the wavelength span of those pulses is reduced compared with the seed pulses due to the gain narrowing effect in the amplifier. The shortest pulses that can be obtained from a Ti:Sa-based CPA system are usually limited to ~15 fs[127]. For some applications such as high harmonic generation and attosecond pulse generation, shorter but still intense pulses are required. One scheme to produce sub-10 fs pulses with large energy per pulse is filament generation.[128] The major challenge for this technique is the spatial mode quality as well as pulse-to-pulse stability. Another common approach is the compression of the continuum generated by self-phase modulation in a rare-gas filled hollow-core fiber [129-132]. We choose the later design for the experiments presented in this dissertation for the better spatial mode quality that this approach provides.

Figure 2.10 shows the optical setup for ultrabroad bandwidth generation with hollow waveguide. Laser pulses from a 15-fs oscillator (Micra Coherent) are shaped by a 4*f* reflective pulse shaper (the pulse shaper will be discussed in detail in section 2.2) using a 128-pixel phase-only programmable liquid crystal (LC) spatial light modulator (SLM). The shaped pulses are then amplified by a regenerative amplifier (Legend USP, Coherent) and focused by a 1 meter focal length curved mirror into an argon-filled hollow waveguide that is 0.39 m long and has a 500 μm inner diameter.

By adjusting the incident laser power, argon pressure and quadratic phase component of the input laser pulse, a continuum broadened spectrum is generated. Optimal continuum generation is obtained when high-order dispersion is eliminated by the pulse shaper and a quadratic phase equivalent to -500 fs^2 group delay dispersion (GDD) is added to the input pulse. It results in an ultrabroad bandwidth spectrum corresponding to sub-5 fs TL pulses (see section 4.1.2). For some applications such as remote chemical detection and identification presented in section 5.3, such ultrabroad bandwidth spectrum is not necessary. In this case, an argon pressure of 0.15 MPa with the input pulse energy of 340 μJ is used to generate 200 μJ of hollow waveguide output from 750 to 870 nm.

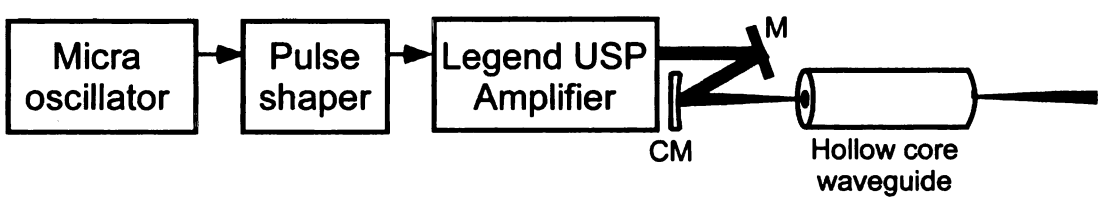

Fig. 2.10. The schematic optical setup for continuum generation from a hollow waveguide. M: mirror and CM: curved mirror.

2.1.5 Ti:Sa oscillator with 2.12 GHz repetition rate

Although a typical femtosecond Ti:Sa oscillator has a repetition rate of ~100MHz, Ti:Sa oscillators with higher repetition rate, from 1 GHz[133] to 10 GHz have been demonstrated. This kind of laser is extremely useful for application such as optical frequency combs[134] for optical frequency metrology and atomic clocks[135], direct measurements of frequencies of several hundred terahertz with 17-digit accuracy[136] and so on.

Ti:Sa oscillators with GHz repetition rates usually have a prismless bow-tie ring

cavity configuration rather than the linear cavity configuration used in the Ti:Sa oscillators described previously in Fig. 2.5. Since the repetition rate is determined by the cavity length, the cavity length of this kind of laser is very small, typically smaller than a human hand. The 2.12 GHz repetition rate laser we used was built in Professor. Cruz's group (University of Campinas, Brazil). It consists of two curved mirrors with broadband high reflecting (HR) coatings and 3 cm radii of curvature, a HR convex mirror with -1 m focal length, and a flat output coupler (2% transmission), configured similar to that described in reference [137] (Fig. 2.11). All mirrors inside the cavity are chirped except the output coupler. The laser provides 0.4 nJ pulses at 2.12 GHz repetition rate with the spectrum spanning ~400 nm

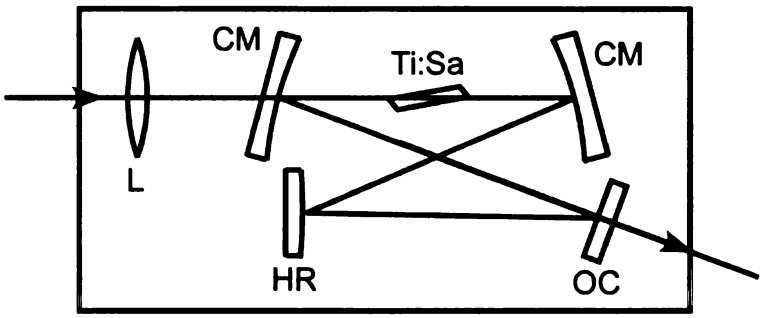

Fig. 2.11. Optical setup schematics of a laser system with bow-tie ring cavity configuration. L: lens with focal length 3 cm; CM: chirped curved mirror (3 cm radius of curvature); Ti:Sa: Ti: Sapphire crystal; HR: high reflection curved mirror with focal length -1m; OC: output coupler. Note that after the pulses hit on HR, they are reflected to OC instead of CM. This is the major difference between the bow-tie ring cavity configuration and the linear cavity configuration. The actual size shown in the figure is approximately 7×3 cm.

2.2 Pulse Shaper

As presented in Chapter 1, we propose to use phase and amplitude shaping to control NLO processes through MII, thus "teaching" the femtosecond laser pulses to fulfill a specific task, e.g., what phase would be optimal phase for a 10 fs laser pulse centered at 800 nm to excite only the breathing vibration mode of toluene. Some tasks

require simple phases such as quadratic phase (chirp) that can be introduced by passive optics such as prism- or grating-based compressors and an optical fiber. The early studies on quantum control of a chemical reaction by the Dantus group were accomplished with the use of a prism based compressor.[138]

However, when more complicated phases, such as higher order polynomial phases, sinusoidal phases or binary phases, are required, the simply apparatus mention above is not sufficient. In this case, a more sophisticated pulse shaping device, capable of modulating the incident electric field, is necessary. There are two different approaches: directly shape the femtosecond pulses in time domain, or shape the femtoscond pulses through masks in frequency domain. The acoustic optical modulator (AOM), introduced by Tournois, is a good example for the former approach.[139-141] The laser pulse is first chirped so that different frequency components enter the AOM at different times. While the pulse is frequency dispersed, a strong acoustic wave enters the crystal and shapes the pulse. This system is compact because it shapes the laser pulse in the time domain. The major difficulty is that extremely accurate synchronization between the laser and the electronics driving the acousto-optical elements is required for precise delivery the desired phase and/or amplitude.

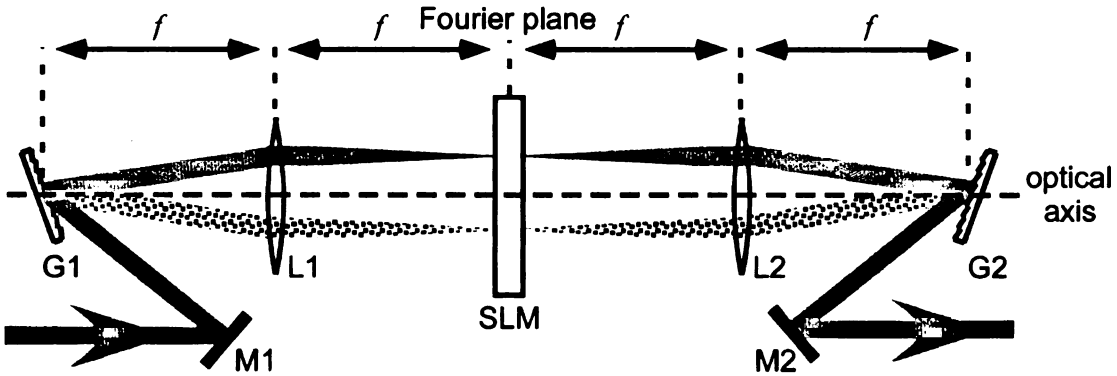

Fig. 2.12. Schematic layout of a 4*f* pulse shaper. The incident beam is dispersed by grating G1 (two different patterns represent different wavelengths) and then focused by lens L1, so that different frequency components are spatially distributed into one dimension at the Fourier plane. An SLM is placed at the Fourier plane in order to modulate the spectral phase and/or amplitude of the pulses. All frequency components are then recombined by lens L2 and grating G2. The distance between each optical component is an *f*, the focal length of the lenses.

The Fourier-transform pulse shaper shown in Fig 2.12, first demonstrated by Weiner and Heritage in 1987,[142, 143] is a typical solution for the pulse shaping in the frequency domain. The laser pulses are first dispersed into different frequency components by a grating (or other dispersive optics), then directed through a pair of identical lenses and finally to the second grating that is identical to the first one. Note that the pair of the lenses forms a 1:1 telescope and both gratings are placed at the focal planes of the lenses. Therefore, the different frequency components are spatially separated and focused by the first lens at the Fourier plane, i.e. at the plane in the center between the pair of lenses. This is equivalent to a Fourier transform of the pulse from the time domain to the frequency (or spectral) domain. The second half of the optical setup recombines all the frequency components, i.e. inverse Fourier transforms the pulses back into time domain. To control the phase of the pulse, a phase shifter, e.g., a LC-SLM, is placed at the Fourier plane where it can modify each frequency component independently. The whole optical setup is called 4*f* setup since

all the optical components are separate by the same focal distance *f*.

Besides the classical linear 4*f* setup, there are other designs of Fourier transformed pulse shapers. Each design has its own advantages and disadvantages. For the experiments described in this dissertation, I used two different designs shown in Fig 2.13: one is prism-based (panel (a)), and another is grating-based (panel (b)).

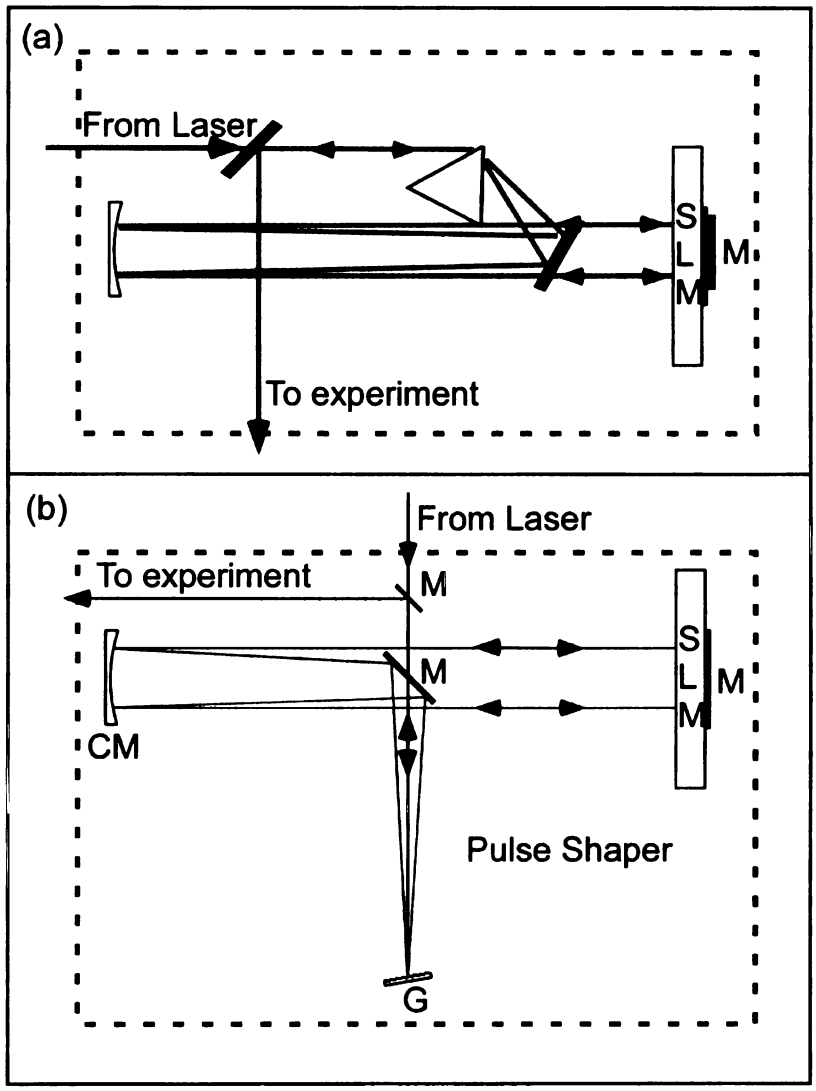

Fig. 2.13. Optical layout of a Fourier-transform pulse shaper. (a) illustrates a prism-based reflective pulse shaper. (b) illustrates a grating-based pulse shaper. Note that the grating is near Littrow condition, i.e., the first order dispersion of the grating propagates along the incoming beam axis, so that the reflection efficiency of the grating is maximized.

The prism-based shaper setup was used with a standard Ti:Sa oscillator and a 128

pixel SLM. The advantage of the prism as a dispersive element is that it is very energy efficient compared with a grating. However, the dispersion of a prism depends on the material from which the prism is made, and usually it is not sufficient to spread the spectrum accross a 640 pixel SLM. On the contrary, gratings with large groove density are more dispersive, but have lower energy efficiency, which is typically 70-90% and tend to be less efficient for broader spectra.

Both of the pulse shaper designs in Fig. 2.13 are reflective designs, i.e., a retro-reflection mirror is placed at the Fourier plane, making the beam travel through the SLM twice. The reflective design has two advantages: 1) it saves space and 2) it doubles the maximal phase retardance of the pulse shaper compared with transmission design shown in Fig. 2.12. The complexity that it brings is the separation of the incoming and outgoing beams. One obvious solution is to displace them vertically, making the off-axis angle of the curved mirrors larger and thus causing slightly larger spherical aberration. Another solution is to use a beam splitter to separate them, resulting in at least 75% energy loss of the pulse shaper. I used the first solution throughout the dissertation.

The SLM is an optical device that uses nematic LC material to alter the phase or polarization of the incident light. The LC material provides an electrically dependent index of refraction for the incident light with polarization along the LC's extraordinary axis but not the light polarized along the ordinary axis, which is orthogonal to the extraordinary one. This is the basic principle that explains how a LC-SLM modulates the phase or polarization of the light. When the orientation of the

LC on the SLM is horizontal (i.e., horizontal extraordinary axis), the SLM can alter the phase of the horizontally polarized incident light. This kind of SLM is usually referred as phase-only SLM. When the orientation of the LC is at 45 degrees to the horizontal axis, it acts as a set of electrically variable waveplates that can alter the polarization of the incident light (usually, polarized horizontally). Combined with a polarizer at the exit of the SLM, the amplitude modulation is achieved as the "waveplates" vary from zero to half wavelength. This SLM is an amplitude-only SLM. A third kind of SLM contains two LC layers with the orientation of each layer orthogonal to each other, and at 45 degrees to the polarization of the incident light. In this case, the phase and amplitude of the light can be modulated simultaneously. The device is referred as a phase and amplitude (P&A) or double-mask SLM. The SLM's used in this project have either 128 or 640 pixels, with pixel size equal to ~97 μm. The pixels can work independently from each other; therefore, one can control the phase and/or amplitude of different frequencies of the incident pulses and achieve the desired pulse shape through changing the voltage on each pixel, provided the SLM is well calibrated.

The calibration of the SLM refers to the determination of the relationship between the retardance achieved and the voltage applied on the SLM, or in other words, the correspondence between the desired phase and amplitude and the voltage applied on the SLM pixels, since the phase and amplitude are related to retardance by:

$$T = \cos^2[\frac{\pi(R_A(V_A) - (R_B(V_B))}{\lambda}] \tag{2.1}$$

$$\phi = \frac{\pi}{\lambda}[R_A(V_A) + R_B(V_B)] \tag{2.2}$$

for a double-mask SLM, where $R(V)$ is the retardance as a function of voltage for each LC array, A and B. The calibration of the SLM is usually achieved by scanning the voltage on the LC array and recording the transmission of the laser spectrum (for double-mask SLM, one needs to apply the maximum possible voltage to one LC array while scanning the other one). $R(V)$ can then be retrieved numerically or analytically through Eq.(2.1).

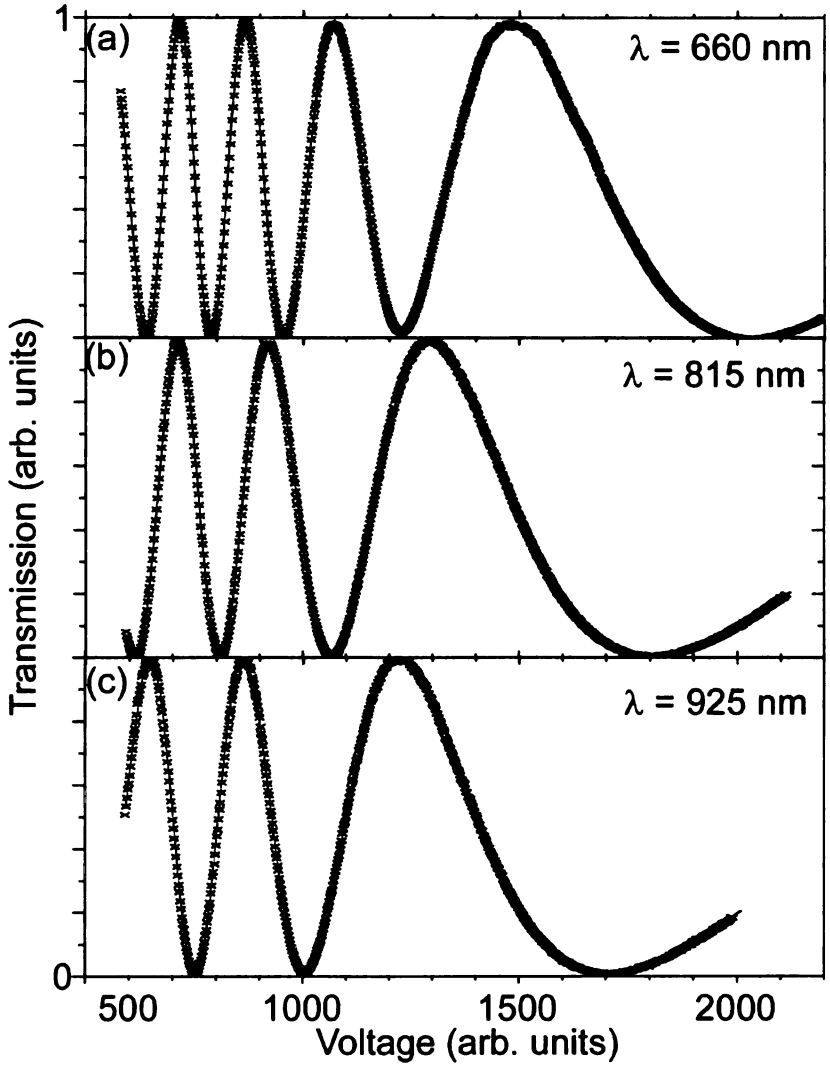

Fig. 2.14. The calibration data (crosses) for different wavelength and their fitting function (gray solid lines). Note the excellent agreement between the data and the fitting function, indicating a precise calibration.

To shape femtosecond pulses accurately, each pixel of the SLM needs to be

calibrated independently because of the frequency dependence of the index of refraction values. Fig. 2.14 shows the voltage dependence of the transmission for three different wavelength (black crosses) or pixels, usually referred as calibration data. Note that the shape of the curve has a large dependence on the incident wavelength. By fitting these curves for all pixels, the $R(V)$ for each pixel can be retrieved analytically. The gray solid lines in Fig. 2.14 shows the fitted functions through an automated calibration program I designed. It takes ~15 minutes for the automated program to calibrate an SLM accurately.

Chapter 3

Pulse characterization technique:

multiphoton intrapulse interference phase scan (MIIPS)

Femtosecond lasers have been applied in a very wide range of fields which now include: optical communications[144], control of chemical reactions[46, 145], nonlinear optical processes[146, 147], semiconductors[148], quantum[149] and nonlinear optical[150] computation, biomedical imaging[151], metrology, micromachining, analytical chemistry, material processing, photodynamic therapy, surgery, and even dentistry. However, as the femtosecond laser pulses get reflected by optical surfaces such as a dielectric mirror, or propagate through a lens, an optical fiber, a microscope objective or any medium other than vacuum, the spectral phase distortion from those media accumulates. These distortions have a significant effect on the nonlinear properties of the pulse, resulting in increased pulse duration, loss of peak intensity (see Fig 3.1) and, even loss of information. As a result, these distortions have serious detriments on almost every application. The shorter the initial pulses, the more significant the distortions become (see the inset of Fig. 3.1), making the characterization and compensation of phase distortions in ultrashort pulses at the sample extremely important.

To minimize the effect of the spectral phase distortion, there are two broad categories of approaches: (i) direct pulse compression and (ii) phase measurement followed by compensation. In case of the former approach, one minimizes phase

distortions without measuring them. The early incorporation of compressors consisting of gratings, prisms,

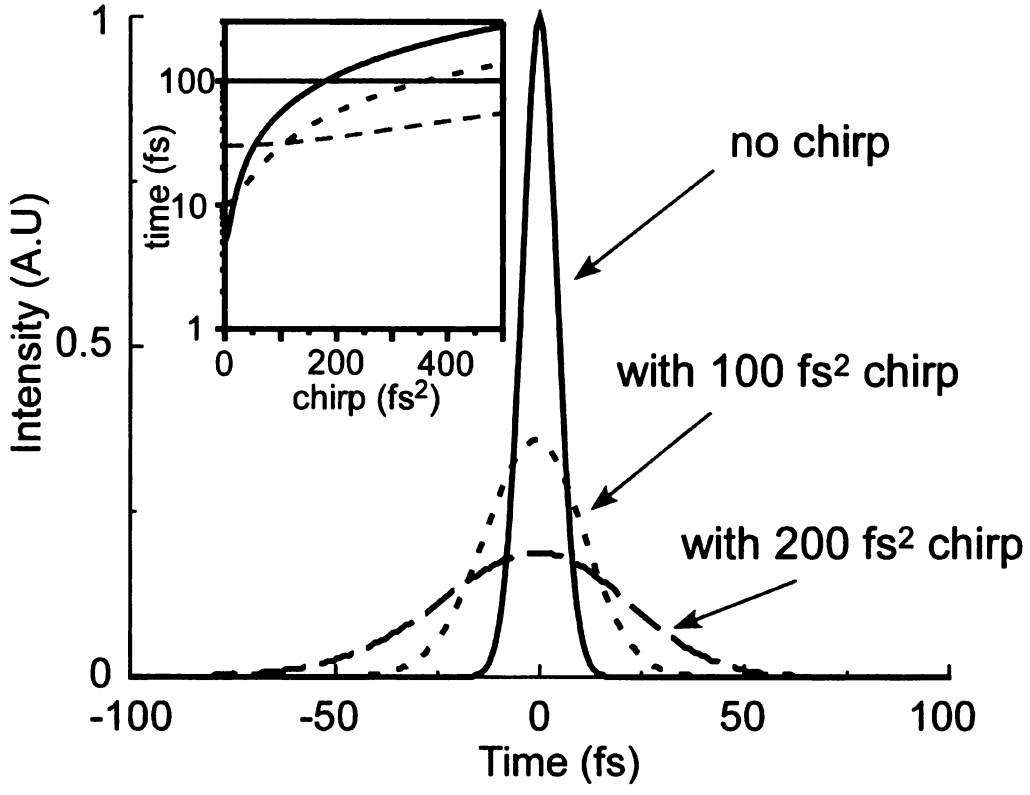

Fig. 3.1. Temporal profiles of a 10 fs pulse with different amount of chirp. The solid line illustrates a Gaussian-shape pulse without phase distortions (TL pulse), the short dashed line shows the pulse with 100 fs^2 chirp, and the long dashed line represents the pulse with 200 fs^2 chirp. Note that besides the obvious increase in the time duration, there is a drop of the peak power by ~1/3 for 100 fs^2 and ~1/7 for 200 fs^2 chirp. The inset shows how quadratic phase distortion (chirp) affects the time duration of initially TL pulses of 5, 10, 30 and 100 fs durations. Note that the same amount of chirp, e.g., 400 fs^2, changes dramatically (by an order ofmagnitude) the time duration of initially short pulses, 5 or 10 fs long, while has essentially no effect on a pulse of 100 fs duration.

and their combination led to the great advancements in femtosecond technology during the early 1980s, culminating in the production of 6 fs pulses[152]. A decade later, Silberberg gourp[36] and Gerber group[37] developed independently another characterization-free scheme, which involved a computer-controlled pulse shaper and a GA that took the integrated SHG intensity from the laser pulses as the feedback in a

closed loop. In both of these characterization-free techniques, success depends on the noise level of the laser system. The pulse-to-pulse stability of the SHG output is typically 2-6%, assuming laser power fluctuations of 1-3% in the fundamental. As a result, the time duration of the pulses after measurement-free approaches could reach as low as 1.02-1.06 times of that of the TL pulses, provided the GA is given sufficient time to converge.

The second category of approaches relies on accurate phase measurement which is followed by accurate compensation. These techniques are required when short time duration of the pulses (<1.1 times of that of TL pulses) is consistently required, such as when the ultrashort pulses are used to study the NLO properties of materials. Among the available spectral phase characterization techniques, the early development of Naganuma *et al.*[153], who used fringe resolved autocorrelation and the spectrum of the pulse to retrieve phase information, and the development of frequency resolved optical gating (FROG)[154] and spectral phase interferometry for direct electric-field reconstruction (SPIDER)[155] represent milestones in the field. Once the spectral phase of the laser pulses is retrieved, a negative spectral phase function can then be introduced into the system by a well calibrated pulse shaper for pulse compression.[45, 139, 156, 157] Here in this chapter, I will present a method called MIIPS which uses a series of well-calibrated reference phases to measure the unknown spectral phase distortion of the femtosecond laser pulses at the target and then corrects the distortion. It is a single beam method which is not autocorrelator/interferometer based as the first three methods stated earlier in this paragraph. From the MIIPS

method, one can analytically obtain the spectral phase across the pulse. Consequently, this method has proven to be extremely powerful, accurate and robust, and has yielded reproducible demonstrations of selective microenvironment probing,[80] multiphoton microscopy,[81] functional imaging[76, 158] and chemical agent identification[83, 84] using ultrashort phase-shaped pulses.

Historically, sinusoidal functions were used as the reference functions for MIIPS. Therefore, I will first discuss the sinusoidal MIIPS after a detailed presentation of the theory. I will present the experimental implementation of sinusoidal MIIPS and its quantitative analysis, including accuracy, precision, dynamic range and the ability to measure arbitrary phase and accurately delivery of desired phase. Following that, a new implementation of MIIP with quadratic reference phase functions (chirp) will be presented.

3.1 Theory

It has long been recognized that NLO processes are sensitive to the second derivative of the spectral phase. Take the SHG for example. The SHG spectrum $S^{(2)}(\omega)$ at a frequency ω can be written as an integral over the spectral amplitude $|E(\omega)|$ and phase $\varphi(\omega)$ of the pulse, according to [159, 160]

$$S^{(2)}(\omega) \propto R(\omega)\left|\int \chi^{(2)}(\omega)E(\omega)E(\omega-\Omega)d\Omega\right|^2 \qquad (3.1)$$

In the case when the laser pulses are not as short as one-optical-cycle and provided that a thin nonlinear crystal is used to generate the SHG spectrum, the pulse spectral response R and the susceptibility χ can be treated as constants, so we can rewrite Eq.

(3.1) for the fundamental pulse with phase modulation $\varphi(\omega)$ as:

$$S^{(2)}(2\omega) \propto \left| \int |E(\omega+\Omega)||E(\omega-\Omega)| \exp\left[i\left(\varphi(\omega+\Omega)+\varphi(\omega-\Omega)\right)\right] d\Omega \right|^2 \quad (3.2)$$

According to Eq. (3.2), the signal is proportional to the integral of the product of a real positive kernel, $|E(\omega+\Omega)||E(\omega-\Omega)|$, with the complex exponent of phase $\varphi(\omega+\Omega)+\varphi(\omega-\Omega)$. TL pulses ($\varphi \equiv 0$) generate the maximum intensity for an SHG spectrum, because the oscillatory component of the integral is zero.

The phase modulation produced by all physical processes, e.g. transmission through any dispersive medium, is typically a continuous function, allowing us to write a Taylor series expansion around ω. The Taylor series expansion of the sum of the phases at positive and negative detuning is

$$\varphi(\omega+\Omega)+\varphi(\omega-\Omega) = 2\varphi(\omega)+\varphi''(\omega)\Omega^2 + \ldots + \frac{2}{(2n)!}\varphi^{2n'}(\omega)\Omega^{2n} \quad (3.3)$$

where $\phi^{n'}(\omega) \equiv d^n\phi(\omega)/d\omega^n$. According to Eq. (3.2), the SHG spectrum is maximized when $\varphi(\omega+\Omega)+\varphi(\omega-\Omega)$ is zero. To first approximation, neglecting higher order even terms, the SHG spectrum has a local maximum at ω when the second order phase distortion, $\varphi''(\omega)$, equals zero.

MIIPS measures the unknown spectral phase by successively imposing a set of parameterized (p) reference spectral phase functions $-f(\omega, p)$ to the pulses with unknown spectral phase distortion $\phi(\omega)$. Hence the total phase of the pulse becomes $\varphi(\omega) = \phi(\omega) + [-f(\omega, p)]$. The SHG spectrum (other nonlinear optical process, e.g., third harmonic generation, can also be used[161]) corresponding to each reference phase is then acquired. In this case, for a certain frequency ω_i, when $\varphi''(\omega_i) = \phi''(\omega_i) + [-f''(\omega_i, p)] = 0$, or in other words, when

$\phi''(\omega_i) = f''(\omega_i, p)$, the SHG intensity at ω_i reaches its maximum possible intensity.

Consequently, in the second derivative space, the set of reference functions $f''(\omega,p)$ can be visualized as a grid used to map the unknown $\phi''(\omega)$, and when $f''(\omega,p)$ intersects $\phi''(\omega)$ at any frequency ω_i, the SHG intensity will be maximized at ω_i. At this frequency, $f''(\omega)$ "compensates" (cancels) $\phi''(\omega)$, and the unknown function, $\phi''(\omega)$, can be measured. In other words, once we find out which reference function $-f(\omega,p)$ gives the SHG maximum for a frequency ω_i, the second derivative will be given by

$$\phi''(\omega_i) = f''(\omega_i, p_{\max}) \tag{3.4}$$

where $p_{\max}$ is the parameter in the reference phase function for which the NLO signal is maximized at ω_i.

In principle, the reference function could be any function. In practice, the simplest grids for mapping the unknown spectral phase in second derivative space are constant functions $f''(\omega, p) = p$ (as the horizontal dashed lines shown in Fig. 3.2(a)),[162] which correspond to the quadratic phase or linear chirp that can be introduced by passive or adaptive optics. For each reference phase, a SHG spectrum is plotted as a function of p in a two dimensional contour map (Fig. 3.2(b)). The feature of interest is $p_{max}(\omega)$, which can be visualized by drawing a line through the maxima in the contour plot (solid curve in Fig. 3.2(b)). The spectral phase information is directly obtained by finding $p_{max}(\omega)$ and using Eq. **Error! Reference source not found.**. In this particular case, Eq. **Error! Reference source not found.** reads

$$\phi''(\omega_i) = f''(\omega_i, p_{\max}) = p_{\max}(\omega_i) \tag{3.5}$$

Therefore, the unknown $\phi''(\omega)$ is directly obtained from the contour plot without any mathematical treatments, as shown in Fig. 3.2(b).

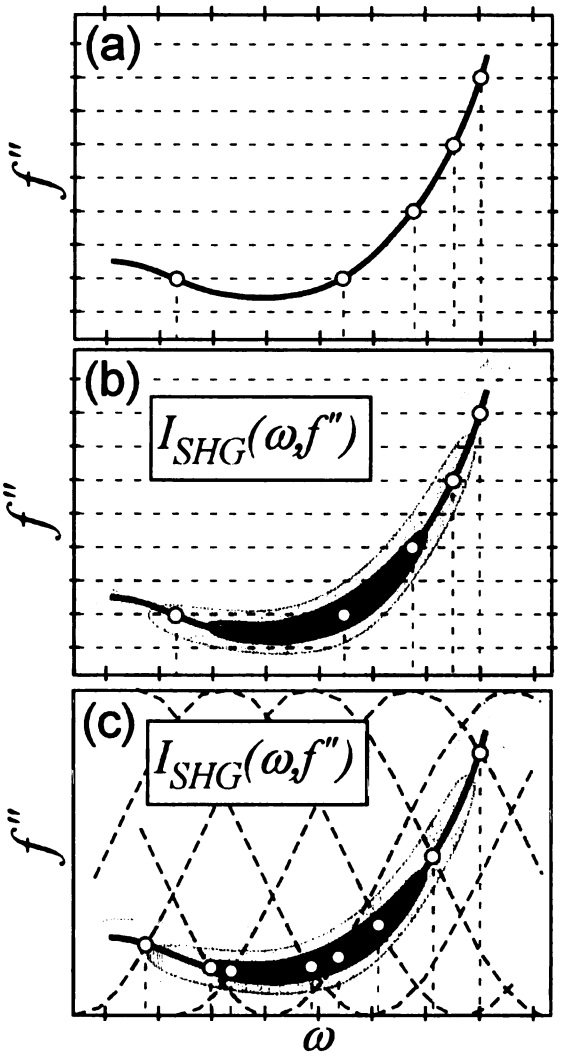

Fig. 3.2. Principle of MIIPS. A set of reference functions $f''(\omega,p)$ provides a reference grid that is used to map the unknown $\phi''(\omega)$. (a) Conceptual diagram based on a horizontal reference grid (dashed) corresponding to different amounts of linear chirp. The solid line represents the unknown $\phi''(\omega)$. (b) shows the MIIPS trace corresponding to a horizontal grid. (c) Shows the MIIPS trace corresponding to a sinusoidal grid. Note that in both cases the unknown $\phi''(\omega)$ is directly revealed by the contour plot.

Different phase functions can be used when an adaptive pulse shaper is involved. The MIIPS method was first used by introducing a set of sinusoidal phases $f(\omega,\delta)=\alpha\sin(\gamma\omega-\delta)$, where δ is the parameter that scans over a 4π range[77, 163]. When the SHG (or other NLO) signal is plotted as a function of ω and $f''(\omega,\delta)$, results

from any reference phase look similar and the unknown $\phi''(\omega)$ is revealed drawing a line through the maxima in the contour plot as shown in Fig. 3.2(c). Note that the dashed lines correspond to the second derivative of the sinusoidal reference functions, $f''(\omega,\delta) = -\alpha\gamma^2 \sin(\gamma\omega - \delta)$, and that the maximal SHG signal occurs at the points at which a reference function intersects the unknown $\phi''(\omega)$. The SHG spectrum can also be plotted as a function of δ. In this case, diagonal parallel lines separated by π are obtained for $\delta_{max}(\omega)$ when the pulses are TL, as shown in the next section.

3.2: Sinusoidal MIIPS

3.2.1 Experimental implementation

The experimental setup for MIIPS necessitates only a thin SHG crystal, a spectrometer, and a pulse shaper capable of accurately introducing spectral phase modulation (see Fig. 3.3). There are no beams to overlap in space and time, and no moving parts. Most experiments presented below in section 3.2 were carried out with a Ti:Sa oscillator capable of producing sub-12 fs pulses centered near 800 nm which has been described in section 2.1.1. The amplified Ti:Sa laser system detailed in section 2.1.2 was also used. A 10μm type-I β-barium borate (BBO) crystal was utilized for SHG, and the output was directed to a spectrometer with ~2 nm spectral resolution. The prism-based pulse shaper, described in section 2.2, which consists of two SF10 prisms, two 200-mm focal length cylindrical mirrors and a dual-mask SLM (CRI, Inc., SLM-256), was used to impose the sinusoidal reference function.

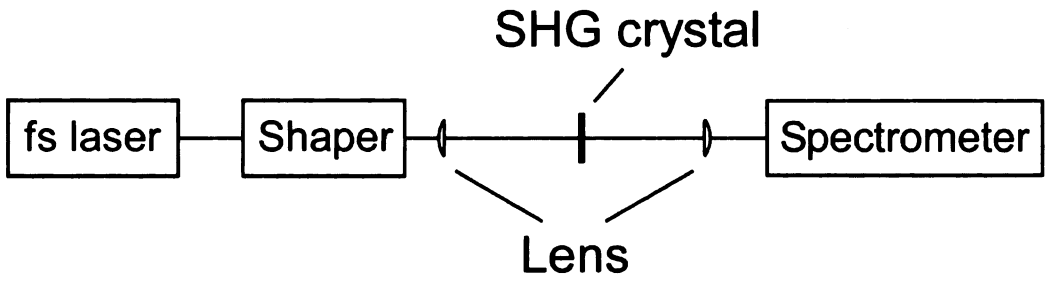

Fig. 3.3. Schematic experimental setup for MIIPS. It requires no interferometer/autocorrelator setup. One simply needs to introduce the laser beam to a NLO medium to generate and then acquire the NLO spectra. In most common cases, a thin SHG crystal, e.g. a BBO crystal, is used as a NLO medium, and the SHG spectrum is recorded for a set of phase masks imposed by the pulse shaper.

For MIIPS measurements, the reference functions $f(\delta,\omega)=\alpha\sin(\gamma\omega-\delta)$ are used, where α and γ are fixed parameters with values equal to 1.5π and the estimated duration of the TL pulse, respectively; the phase shift, δ, is a variable parameter typically scanned from -0.5π to 3.5π. The advantages to use the sinusoidal functions are following. First, the maximum amplitude is limited to 2α over all values of δ, which is experimentally practical because the delay range of an the adaptive pulse shaper is limited to several π. Second, the periodicity of the sinusoidal function allows MIIPS a chance to check the data reproducibility of data and to effectively average out random fluctuations and systematic shifts.

For most measurements, we used γ = 10 fs, α = 1.5π and scanned δ = 128 steps over a 4πrange. The acquisition of an SHG spectrum for each step over this range results in two replicas of the MIIPS trace. From the acquired spectra, a 2D contour plot for $SHG(\delta,\omega)$ is obtained (see left panels of Fig. 3.4), where $\omega = \pi c/\lambda_{SHG}$. The value of $\delta_m(\omega)$ for each frequency is found, and, from these values, the second derivative of the unknown phase is calculated by

$$\phi''(\omega) = \alpha\gamma^2 \sin\left(\gamma\omega - \delta_m^n(\omega)\right) \tag{3.6}$$

There are multiple solutions (index n) for Eq. (3.6). Because of these multiple solutions, the range in which we search for the maxima of the SHG spectra must be specified.

The expected values of $\delta_m^n(\omega)$ for TL pulses can be found by substituting $\phi'' = 0$ into Eq. (3.6),

$$\delta_m^n(\omega) = \gamma(\omega - \omega_0) + n\pi, n = 0, \pm 1, \pm 2 \ldots \tag{3.7}$$

where $\omega_0 = 2\pi c/\lambda_0$ is the carrier frequency and λ_0 is the central wavelength of the laser spectrum.

For TL pulses, the features in the MIIPS trace where the SHG signal is greatest form parallel lines separated by π. Based on this observation, we can restrict the search area of $\delta_m(\omega)$ for non-TL pulses. These black lines shown in the left panels of Fig. 3.4 define the search area.

For the analysis of a sinusoidal MIIPS trace, the $\delta_m^n(\omega)$ values in two neighboring areas are defined (as shown in the left panels of Fig. 3.4) and used to calculate the second derivative of the unknown phase distortion

$$\phi''(\omega) = \tfrac{1}{2}\alpha\gamma^2\left[\sin\left(\gamma\omega - \delta_m^1(\omega)\right) + \sin\left(\gamma\omega - \delta_m^2(\omega)\right)\right] \tag{3.8}$$

The use of two lines provides more accuracy in the measurements.

An iterative procedure of measurement and compensation is used to obtain very accurate results. The experiment begins as described above, and the phase is measured. To compensate this distortion, $-\phi^{I}(\omega)$ is added to the phase using the pulse shaper, the phase scan is repeated, and the next order of phase correction, $\phi^{II}(\omega)$, is

measured. The sum, $-(\phi^{I}(\omega)+\phi^{II}(\omega))$, is used as the correction function for the next iteration. The convergence towards an accurate phase profile is exponentially fast and the phase distortion is close to zero after only 3-5 iterations. As shown in Fig. 3.4, the residue of the phase at the fifth iteration is very close to zero.

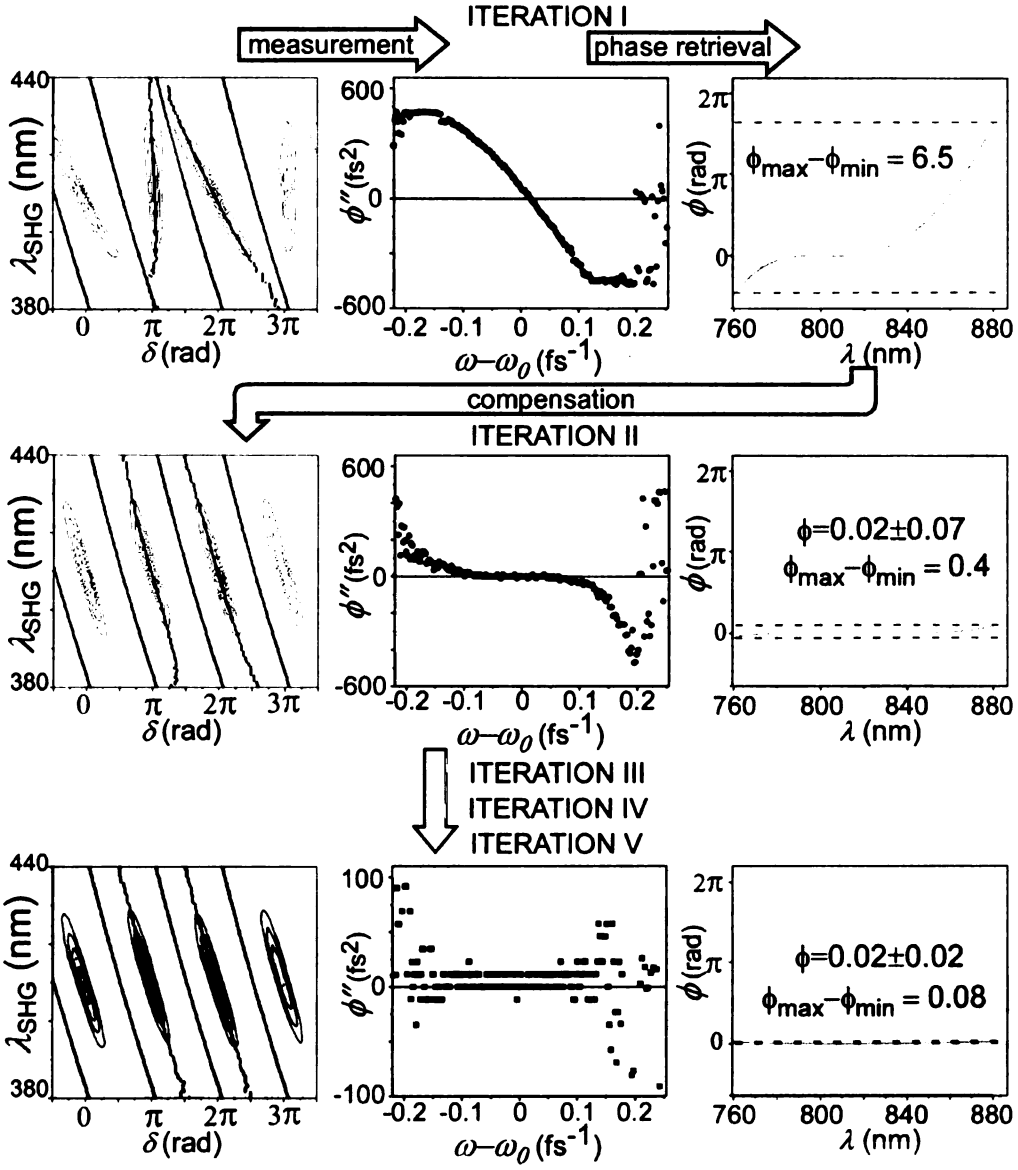

Fig. 3.4. Experimental demonstration of the MIIPS iteration process. The left panels are SHG spectra as the δ parameter of the reference function is scanned. Each vertical line corresponds to a separate SHG spectrum obtained at a given value for δ. The black lines which separate the MIIPS traces are used to define the region for searching $\delta max(\omega)$. The dots within those boundaries show $\delta max(\omega)$. The center panels show the measured second derivative of the spectral phase. The right panels show the phase calculated from the measured second derivative.

The unknown function $\phi(\omega)$ is accurately given by the sum of the iteratively determined compensation functions,

$$\phi_{measured} = \phi^{I} + \phi^{II} + \cdots + \phi^{N} \tag{3.9}$$

Fig. 3.5 highlights the measured phase after 5 iterations for this measurement, as well as the phase measured from the first iteration of this measurement. It shows that the first iteration already gives a good approximation of the phase distortion and the only significant deviation appears at the wings of the spectrum.

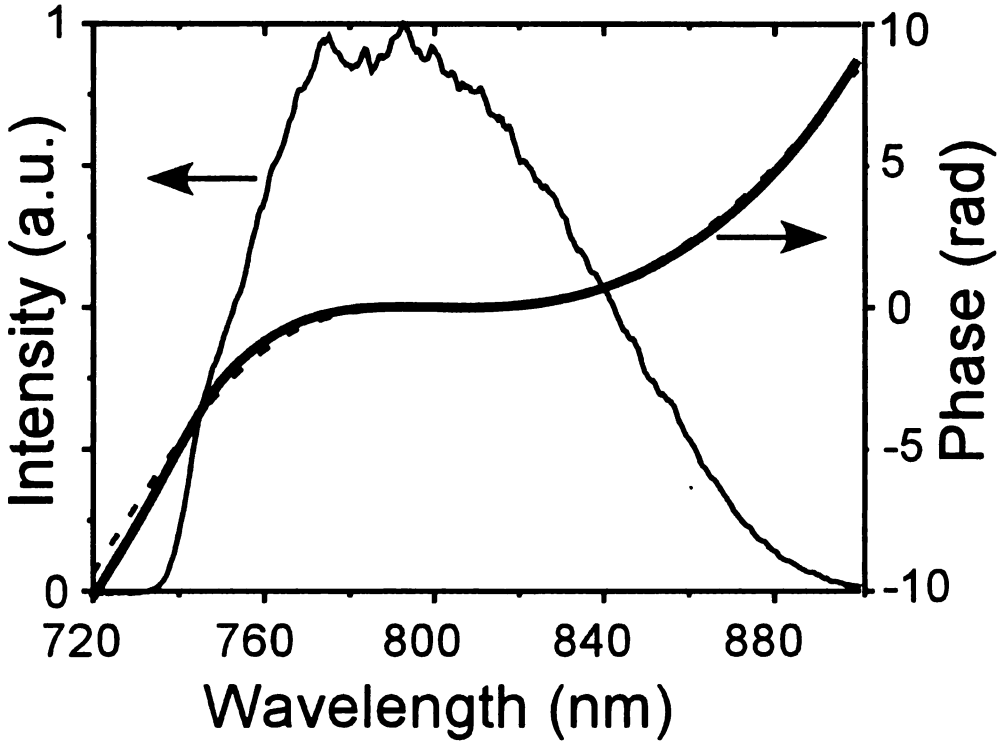

Fig. 3.5. Measured phase. The thick solid line highlights the measured phase after five iterations, and the dashed line shows the measured phase from the first iteration. The thin solid line shows the spectrum of the laser pulse.

3.2.2 Accuracy

To quantitatively test the accuracy of MIIPS, we measured the GVD of quartz, a material for which the value of GVD has previously been measured by more conventional and accepted techniques. The beam was passed through quartz windows

of thicknesses 3.25, 4.92, 6.53 and 9.58 mm before being focused on an SHG crystal. MIIPS was used to directly measure the GDD introduced by the quartz slabs, together with all other optical elements in the system, and the optical system along (with no quartz present) as a reference.

Fig. 3.6(a) shows the measured second derivative of the spectral phase of the system for the different thicknesses of quartz. It is very important to note that the lines are both parallel and spaced proportionally to the thickness of the quartz (as shown in Fig. 3.6(b)). The GVD introduced by the quartz windows was measured to be 36.2 ± 0.5 fs^2/mm at 800 nm, which is in good agreement with the 35.92 ± 0.05 fs^2/mm measured by Diddams and Diels[164], using white-light interferometry. For further comparison, the GVD of quartz at 800 nm was calculated using the Sellmeir formula and the constants published by Malitson[165], and found to be 36.162, which is in excellent agreement with our measured value.

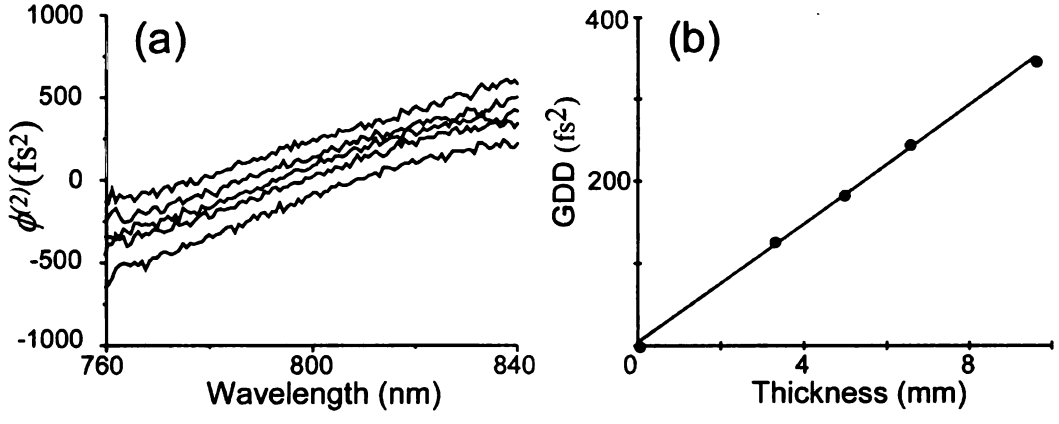

Fig. 3.6. GVD measurement of quartz using MIIPS. (a) shows the measured GDD of the system (from bottom to top: 0, 3.25, 4.92, 6.53 and 9.58 mm thick quartz windows). (b) shows the GDD at 800 nm as a function of thickness.

The measurement process was then repeated for glass microscope slides (crown glass, Fisher Scientific, each 1 mm thick), this time measuring the GDD as a function

of the number of slides. Nujol index matching oil was used between them to avoid multiple reflections at the interfaces. As the thickness of the slides is uniform, a reliable system for quantifying the GVD is expected to show a linear dependence of GDD on number of microscope slides.

Figure 3.7(a) summarizes the measured second derivatives of the spectral phase for every other slide addition. Fig. 3.7(b) (all data shown) highlights the reliability of the MIIPS method. It can be seen that the experimentally measured GDD versus the number of microscope slides (thickness of glass) can be successfully fitted by a straight line. The GVD introduced by the microscope slides was measured to be 50.7 ± 0.5 fs^2/mm at 800 nm. Assuming the type of crown glass used for the microscope slides corresponds to Ohara glass S-NSL 5 (equivalent to Schott glass K5), we can compare the measured GVD with the calculated value using the Sellmeir formula and constants available from Ohara.[166] The calculation gives 50.13 fs^2/mm at 800 nm, which is in good agreement with the experimental measurement.

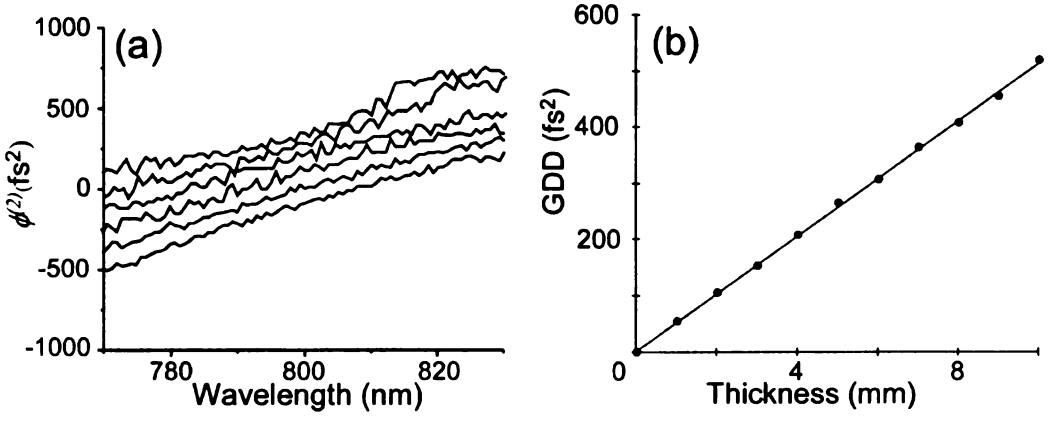

Fig. 3.7. GVD measurement of microscope slides using MIIPS. (a) shows the measured GDD of the system (from bottom to top: 0, 2, 4, 6, 8 and 10 mm microscope slides). The data for the odd number of slides (odd thicknesses) were omitted from this graph, but not from the calculation, for clarity. (b) shows the GDD at 800 nm as a function of thickness.

Both of the above results demonstrate that the second derivative of the spectral phase can be measured by MIIPS with incredibly high accuracy. A more recent work shows that MIIPS can measure the GVD of water with an error lower than 0.2 fs^2/mm[167]. This ±0.2 fs^2/mm accuracy and a ±0.1 fs^2/mm precision obtained with MIIPS allowed detecting a ~1.3 fs^2/mm difference between the GVD of deionized water and that of seawater.

3.2.3 Reproducibility/Precision

In this subsection, reproducibility tests for MIIPS are described. Several MIIPS iterations were run to obtain a compensation mask (negative of the measured phase). This compensation mask was then applied, and a single iteration of MIIPS was run ten times successively (each time starting from the compensation mask). The measured phases were then analyzed for reproducibility. The solid line in the lower panel of Fig. 3.8 is the average of the ten measured phases. The error bars in all figures show ±1 standard deviation for every fifth point. The reproducibility of MIIPS is seen to be excellent over a range well exceeding that of the FWHM, as shown in the upper panel of Fig. 3.8.

For a quantitative comparison of MIIPS with other well-established phase measurement methods, the average of the standard deviations for each point was calculated using the power spectrum as a weighting function. Over the entire range of the spectrum, analyzing the full set of data, across the whole spectrum, the statistical phase error was calculated to be 0.013 rad. Using a reduced set of five scans, the

statistical phase error found to be 0.011 rad. Table 3.1 compares these results to those reported by Gallman et al for FROG and SPIDER.[168]

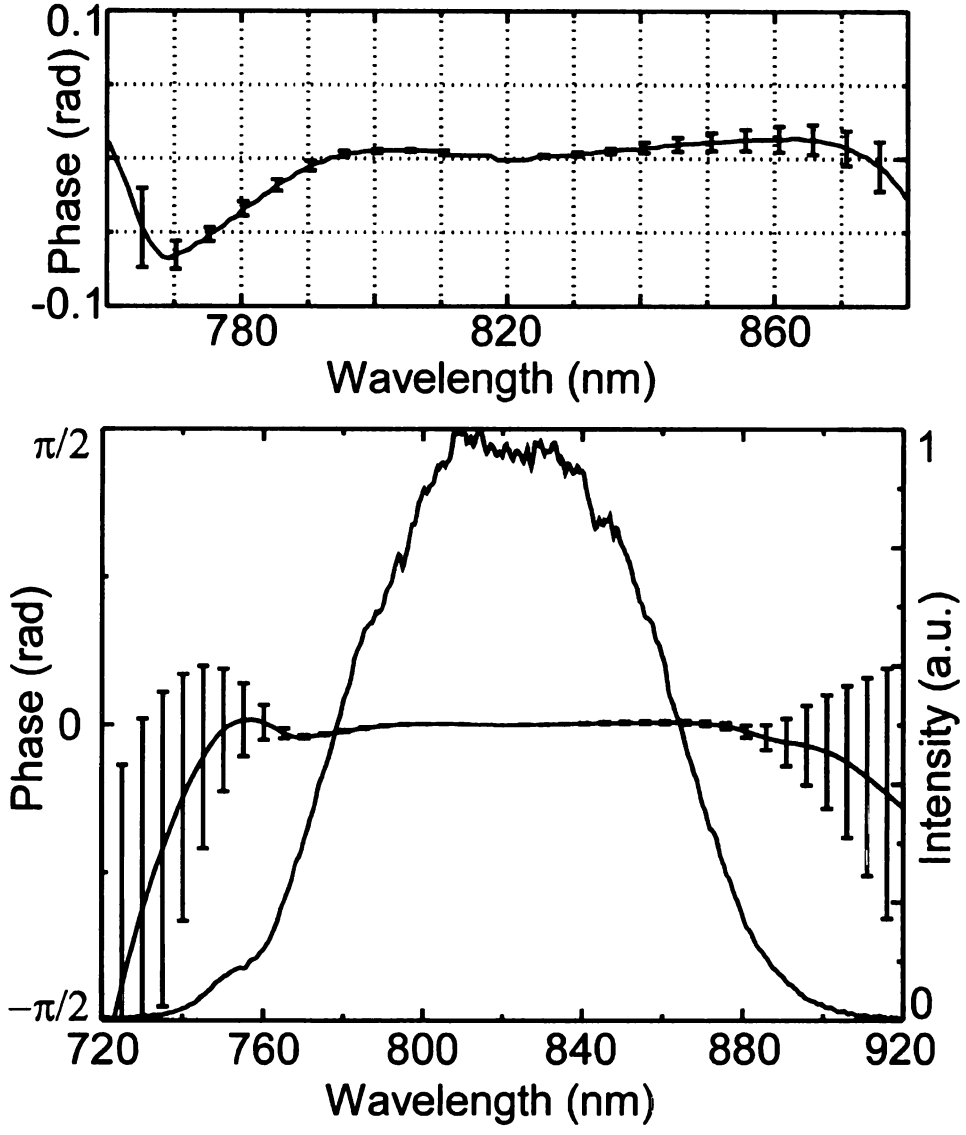

Fig. 3.8. Reproducibility of MIIPS. In both panels, the solid line shows the average of ten independently measured phases, while the error bars show ± 1 standard deviation for every fifth point. The lower panel shows the full range of collected data. The upper panel shows a closer view of the region over which MIIPS can compensate the phase distortion (760-880 nm).

Also of interest is the great reduction of statistical phase error when the range of data analyzed was reduced to that where the measured phase was flat (i.e. MIIPS had successfully compensated phase distortions). For this range (shown in the upper panel

of Fig. 3.8.), the statistical phase error was reduced to just 0.004 rad. Additionally, some tasks, such as GVD measurement at a certain frequency, do not require the knowledge of the phase over a wide spectral range. Within the FWHM of a pulse, MIIPS measures the phase with unprecedented precision: the statistical phase error is 0.0028 rad. This data leads us to conclude that MIIPS is a method with high reproducibility, exceeding that of FROG and SPIDER techniques.

Table 3.1. Comparison of Reproducibility for MIIPS, FROG and SPIDER: Statistical Phase Error (in rad)

Method	Full Data Set	Reduced Data Set	Full Data Set (FWHM)
MIIPS	0.013	0.011	0.0028
FROG[168]	0.122	0.048	
SPIDER[168]	0.044	0.017	

3.2.4 Arbitrary phase measurement

Here the ability of MIIPS to measure arbitrary phase distortions is tested. The availability of automated pulse shapers has made possible the generation of ultrashort laser pulses with complex spectral phases, which are used in areas such as coherent control[20, 169] and nonlinear microscopy[80, 170, 171]. The characterization of complex phases without the need of a well-characterized reference pulse has been experimentally demonstrated using SPIDER [172]. Here MIIPS is used to measure complex arbitrary phases. This is done by applying the known synthetic phases to a

TL pulse, running several iterations of MIIPS, and comparing the measured phase with the applied phase. We analyzed two different synthetic functions: a double Gaussian and a sine function with amplitude $\pi/2$ and four periods across the SLM; the results are shown in Figs. 3.9(a) and (b), respectively. Note the good agreement between the measured (dots) and applied phases (solid line) in each case, indicating that MIIPS is capable of accurately retrieving an arbitrary phase from a pulse.

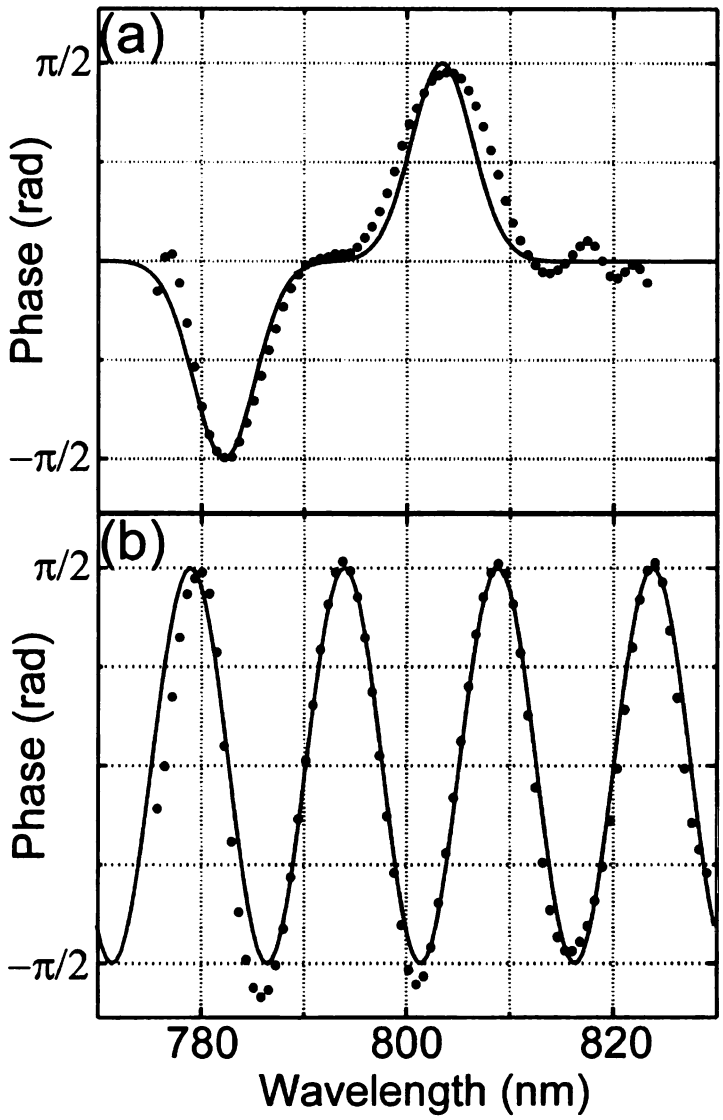

Fig 3.9 Ability of sinusoidal MIIPS to measure arbitrary phase functions (the same pulse shaper was used to introduce and measure the arbitrary phase functions). (a) shows the result for an applied double Gaussian function. (b) shows the result for a sinusoidal function. The dotted lines show the measured phase, and the solid lines are the applied phase.

In a set of recent experiments to measure the complex spectral phases, two independent all-reflective grating-based pulse shapers containing a 640-pixel dual-mask SLM (SLM-640, CRi Inc.) were used. One pulse shaper introduced the desired spectral phase, while the other was used to measure it using sinusoidal MIIPS. The agreement between the introduced and measured phases illustrates the performance of the method for the case of complex spectral phases; see Fig. 3.10.

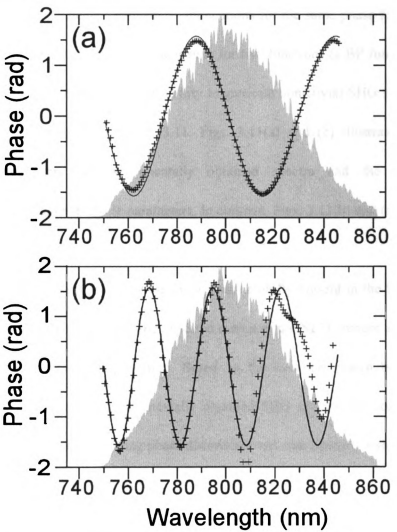

Fig. 3.10. Sinusoidal MIIPS measurements of complex spectral phases. The solid curves correspond to the synthetic spectral phases introduced by the first pulse shaper. The crosses correspond to the phases measured by the second pulse shaper. The shaded areas represent the spectrum of the pulses. The introduced phases (a) and (b) are sinusoidal functions with periods 39 and 78 fs, respectively.

3.2.5 Accurately delivery of desired phase after MIIPS compensation

To quantitatively test the accuracy of the MIIPS method to not only measure the spectral phase of a pulse, but to subsequently compensate for the measured phase distortions while imposing a desired phase profile, MIIPS was first used to acquire a TL pulse. A well-defined phase function was then introduced to the TL pulse, and the SHG spectrum was recorded. The experimentally measured spectrum was compared to the spectrum predicted by theoretical applications for the same phase function and the known fundamental spectrum. The results for two functions (a BP function and a sinusoidal function), chosen for their ability to generate non-trivial SHG spectra with multiple peaks, are shown in Fig. 3.11. Figs. 3.11(a) and (c) illustrate excellent agreement between the experimentally obtained spectra and the theoretical calculations with no adjustable parameters. In contrast, Figs. 3.11(b) and (d) show the resulting SHG spectra when the same phase functions are applied to the uncompensated pulses. Clearly, phase distortions naturally present in the laser pulses cause significant deviations from the expected output of the NLO process and must be eliminated by accurate compensation. Based on the excellent match between the theoretically predicted and experimentally obtained SHG spectra, we conclude that MIIPS is capable of compensating phase distortions, and consequently eliminating the deleterious effects the distortions have on NLO processes.

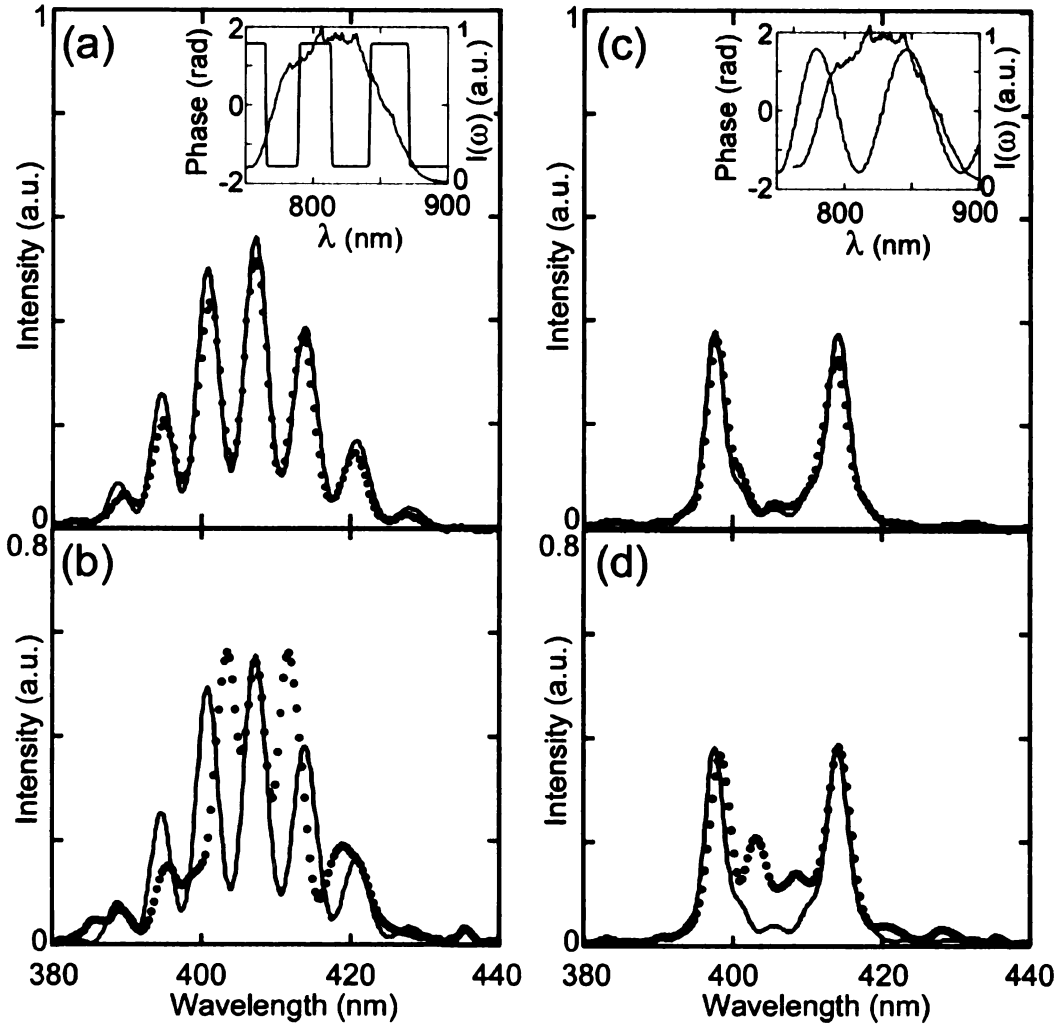

Fig. 3.11. Delivery of a desired phase profile to the pulse at the target: experimental data and theoretical calculations. The solid line in each panel shows the theoretical spectrum predicted for the application of a particular binary phase (panels (a) and (b)) or a particular sine function (panels (c) and (d)). The dotted lines correspond to the experimentally measured SHG spectrum for each case. For panels (a) and (c), pulses are MIIPS pre-compensated before the phase masks, shown in the insets, are applied. For panels (b) and (d), the phase masks applied directly, without MIIPS compensation of phase distortions.

3.2.6 Dynamic range

In this section, we tested the dynamic range for chirp compensation of the MIIPS method. At the low end, phase deviations over the entire bandwidth of the pulse (760-880 nm) are typically in the milliradian range: 0.02 rad (see Fig. 3.4). Higher sensitivity can be achieved through adjusting in the parameters α and γ and by

reducing the step size for the parameter δ to smaller than the size of a SLM pixel. Already at 0.02 rad, MIIPS is more sensitive than most of the established methods. At the high end of phase distortions, there is a point where maxima in the MIIPS traces coalesce and one can no longer measure a distance between them. This occurs when phase distortions are of the order of $\alpha\gamma^2$. Even in these cases, MIIPS is still capable of introducing a compensation phase that, after a number of iterations, corrects for very large phase distortions, as shown below.

When the phase modulation is greater than the total retardation allowed by the SLM, the phase is reformed by wrapping. Since the allowed retardance of our SLM ranges from -3π to 3π, we fold the spectral phase within a $\pm 1.1\pi$ range ($\pm 1.5\pi$ must be reserved for the reference sine function). In Fig. 3.12, we show the result of phase compensation for a 40 fs pulse from an amplified laser system that has been significantly chirped (3×10^4 fs^2) by the gratings in the internal compressor. Notice that despite significant wrapping of the phase (Fig. 3.12(b)), excellent compensation has been achieved, as can be judged by the residue phase (see the top panel of Fig. 3.12(a)).

The top end of the dynamic range is three times greater for the shaper used with the amplified system than for the sub-12 fs laser system on which most of the work was done. The range is limited by the optical design of the pulse shaper taking into account the available number of pixels and the maximum retardation per pixel. Empirically, for the a shaper with a 128-pixel SLM, we find the upper dynamic range in ϕ''_{max} to be $\phi''_{max} = \phi_{max}\tau^2/4$, where ϕ_{max} is the maximum wrapping (in our

case 100 rad) and τ is the pulse duration. A similar estimation can be made for higher order terms.

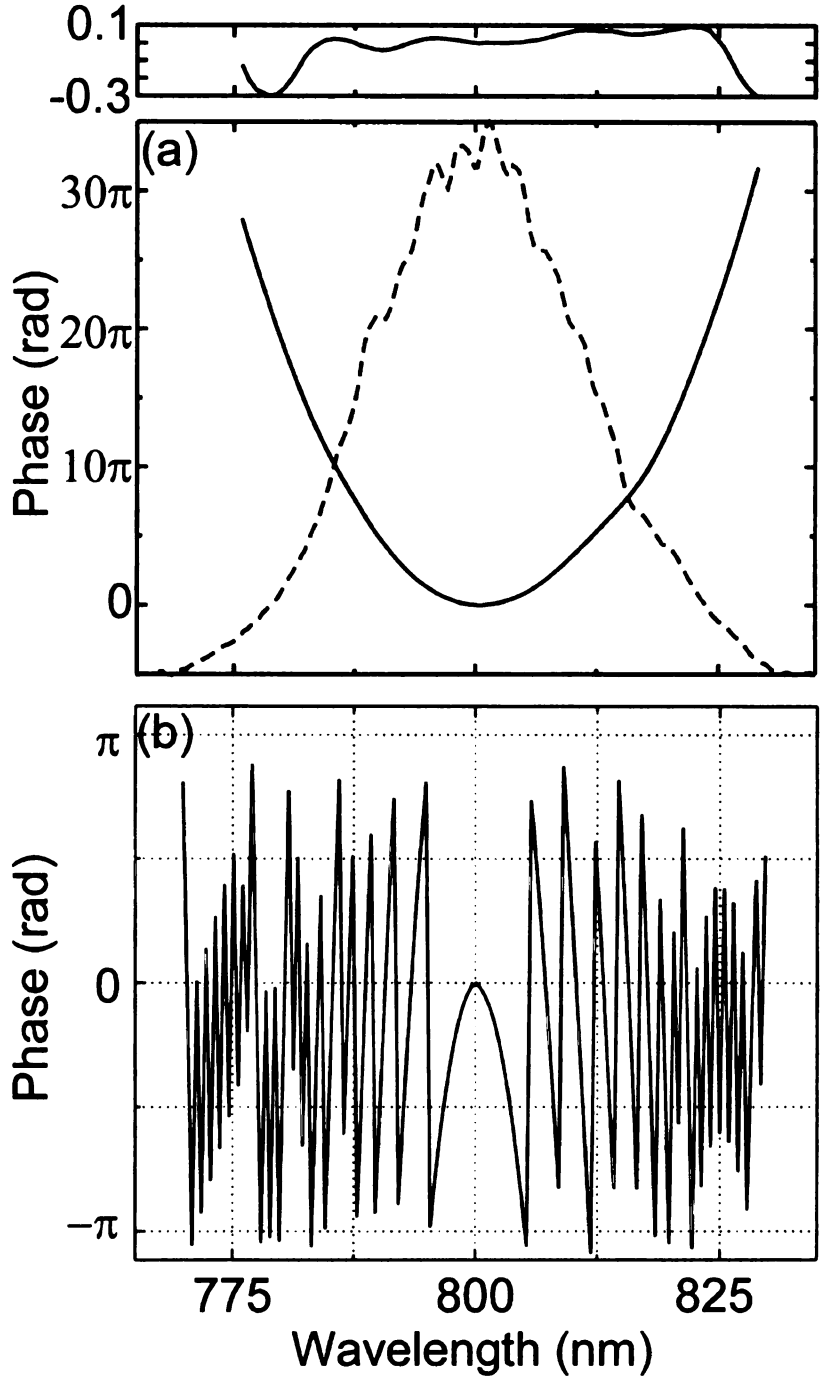

Fig. 3.12 MIIPS compensation of a heavily chirped pulse. (a) shows the measured phase of the uncompensated pulse. The upper panel shows the residue of the phase after successful compensation by MIIPS. (b) shows the applied compensation mask, with significant wrapping.

3.3 Chirp MIIPS

In this section, the implementation of quadratic phase functions, or chirps, as the reference phase functions for MIIPS, is presented. The Venteon Ti:Sa oscillator, with the output spectrum spanning 620-1050 nm, is used to test the experimental implementation of chirp MIIPS. The pulse shaper used to introduce the reference spectral phase $-\phi(\omega)$ was a folded all-reflective grating-based system with a 150-lines-per-mm grating, a 762-mm–focal-length spherical mirror, and a 640-pixel dual-mask SLM (see section 2.2). After the shaper, the laser pulses were focused onto a 20-μm type-I Potassium dideuterium phosphate (KDP) crystal, and the SHG signal was separated from the fundamental before it was directed to a spectrometer. The setup will be discussed in detail in the next chapter.

As stated previously in the theory section, the quadratic reference phase functions, $\phi(\omega, p) = \frac{1}{2} p(\omega - \omega_0)^2$, correspond to a set of horizontal grids in the space of phase second derivative. Therefore, when the SHG spectrum corresponding to each reference phase is plotted as a function of the scanning parameter p in a two dimensional contour map, the second derivative of the phase will be directly visualized in the contour map as the maximum for each frequency. To test the chirp MIIPS implementation, TL pulses were first obtained using the sinusoidal MIIPS method. A cubic spectral phase function defined as $\phi(\omega) = 500\text{fs}^3 (\omega\text{-}\omega_0)^3$, which corresponds to a linear $\phi''(\omega)$, was then introduced to the pulses and then the chirp MIIPS was performed to measure it. The experimental trace, SHG spectrum as a function of p, is shown in Fig. 3.13. The dashed line indicates the spectral maxima,

which directly correspond to the introduced $\phi''(\omega)$. Note that both the accuracy and precision of the measurement are ~1-2 fs^2, and that the results were obtained from a single chirp scan with grid-steps of 5 fs^2.

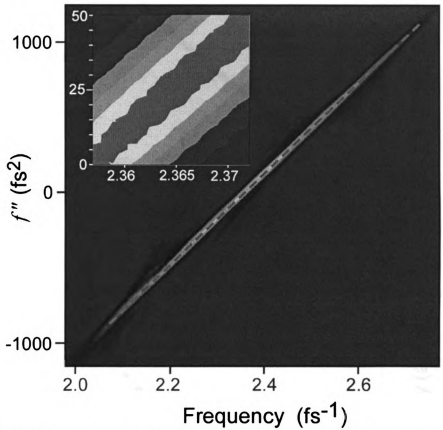

Fig. 3.13. Experimental measurement of a cubic phase obtained by a single chirp scan. The figure is a contour plot of the SHG spectra measured at each value of applied chirp. The feature revealed by the spectral maxima corresponds to the second derivative of the cubic phase introduced. As expected, the second derivative is linear with frequency. The inset shows a magnified portion of the trace.

Once $\phi''(\omega)$ is obtained, double integration can be used to calculate $\phi(\omega)$. Figure 3.14 shows the measured and the introduced functions, together with the spectrum of the laser. Note the excellent accuracy of the phase measurement, only after a single chirp scan. The third-order dispersion (TOD) was measured with 0.5% accuracy.

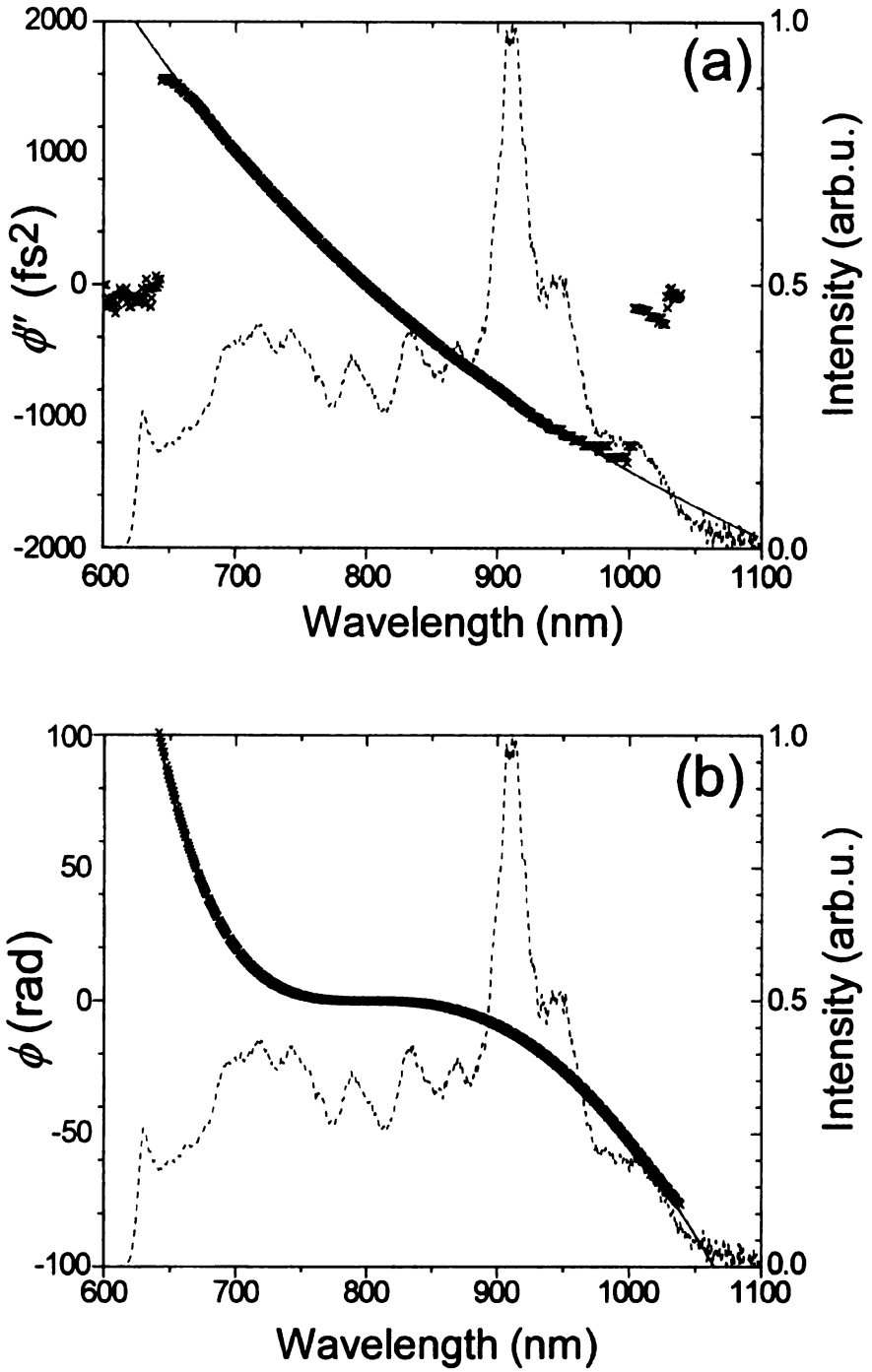

Fig. 3.14. Spectral phase measurement. The introduced (gray solid lines) and measured (black crosses) phase functions agree without adjusting parameters. (a) shows the second derivative of the spectral phases. (b) shows the spectral phases. The laser spectrum is also shown with dashed gray lines.

The method presented is able to measure arbitrarily complex spectral phases, as has been shown for sinusoidal MIIPS (presented in the previous section). To

demonstrate this ability, a sinusoidal spectral phase function defined by $\phi(\omega)=5\pi\ sin[7\text{fs}\ (\omega-\omega_0)]$, was introduced using the pulse shaper and then measured by the chirp method (see Fig. 3.15).

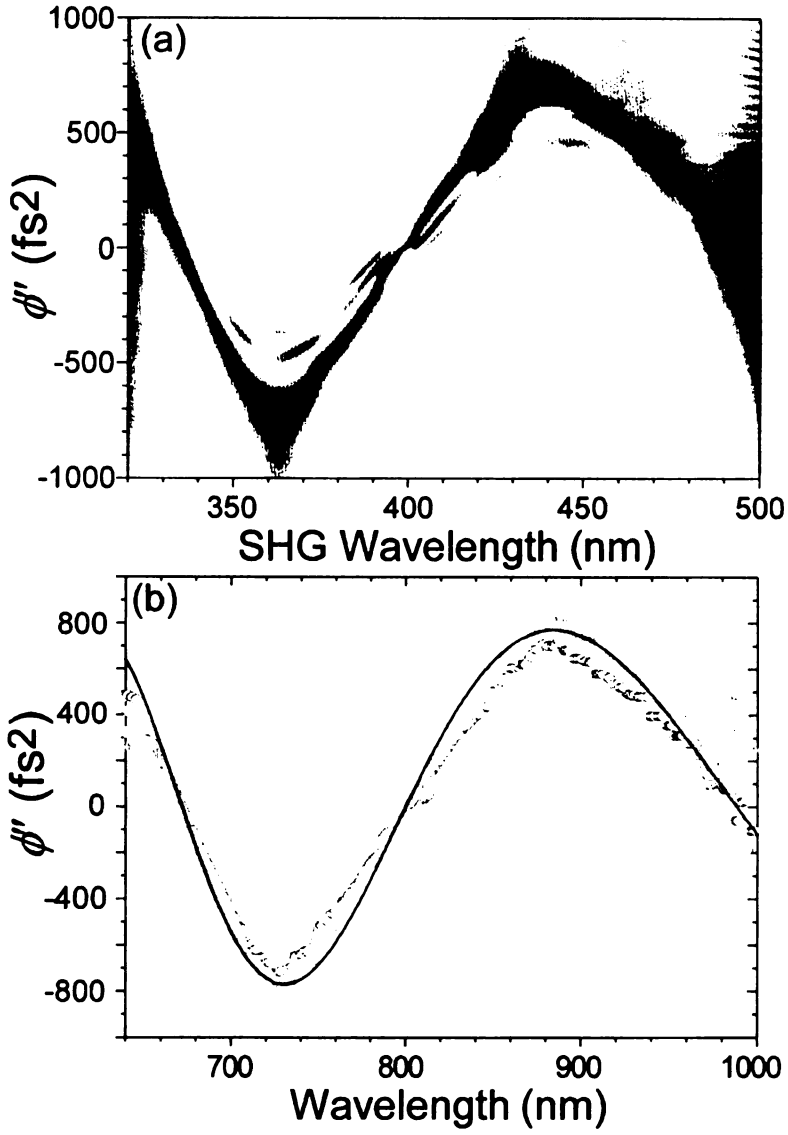

Fig. 3.15. Sinusoidal spectral phase measurement. (a) shows the experimental trace. The measured second-derivative of the phase can be directly visualized from the feature corresponding to the spectral maxima. (b) shows the measured second-derivative after a chirp scan (circles) and after one measurement-and-compensation iteration (gray dots). The solid line is second derivative of the introduced sinusoidal function.

As evident from the MIIPS trace shown in Fig. 3.15(a), the second derivative of the introduced phase is obtained from a chirp scan. The measured phase (circles) is

very close to the phase introduced by the pulse shaper (solid line), as shown in Fig. 3.15(b). To improve the quality of this method, an iterative measurement-and-compensation routine presented in previous section can be used.

A set of experiments similar to those where the complex spectral phases were applied and measured independently by two pulse shapers, described in section 3.2.4, were also performed with chirp MIIPS. One pulse shaper introduced the desired spectral phase, while the other was used to measure it using chirp MIIPS. The excellent agreement between the introduced and measured phases shown in Fig 3.16, clearly demonstrates the performance of chirp MIIPS method for the case of complex spectral phases.

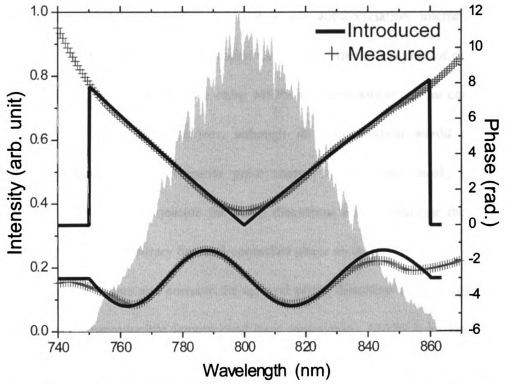

Fig. 3.16. Chirp MIIPS measurements of (a) a V-shape phase function and (b) a sinusoidal phase function. The solid curves correspond to the synthetic spectral phases introduced by the first pulse shaper. The crosses correspond to the phases measured by the second pulse shaper. The shaded area represents the spectrum of the pulses.

3.4 Conclusion

In this chapter, I have presented the implementation of MIIPS to directly measure the second derivative of the phase $\phi''(\omega)$, without relying on any retrieval algorithm, and thus determine the spectral phase of the pulses analytically. In chirp MIIPS, $\phi''(\omega)$ is visualized in the experimental contour plot, without any mathematical treatment. The accuracy was found to be 0.02 rad with 0.003 rad precision across the FWHM of the pulse, for the measured spectral phase and ± 0.2 fs^2/mm with a ±0.1 fs^2/mm precision for the measured GVD of materials. The dynamic range of MIIPS is very large. For a 640-pixel pulse shaper, it can successfully measure and compensate phase distortions up to ~500 rad and detect phase difference as small as 0.02 rad.

Data acquisition for MIIPS does not require autocorrelation, interferometry or even a computer controlled pulse shaper. Given that different amounts of chirp can be applied using passive optics, the chirp MIIPS implementation can be conveniently implemented using these devices, although its compensation would not be as straightforward. A more versatile pulse shaper, used in this work, is able to accomplish both tasks: measure the phase distortions and compensate them. It also allows introducing arbitrary but well-controlled phase masks.

MIIPS measures and corrects the spectral phase distortion at the target. This is necessary for reproducible femtosecond laser applications. MIIPS is an ideal method for laser pulse compression, as I will presented in the next chapter. Control of the spectral phase through MIIPS makes the accurate and reproducible pulse shaping

possible. Therefore, MIIPS establishes a solid base for laser control of multiphoton processes and selective molecular excitation.

Chapter 4

MIIPS Applications

4.1 Pulse characterization and compression

The quest for ultra-broad-bandwidth femtosecond laser pulses has progressed at a very fast rate during the last five years. In 2002, Baltuska *et al.*[173] used a double-pass noncollinear optical parametric amplifier (NOPA) system to deliver sub-4 fs visible-near-infrared pulses. They also used SHG-FROG and a feedback loop as a means for adaptive pulse compression. In 2006, Yamashita *et al.*[94] generated 2.8 fs pulses, in a system in which a hollow fiber filled with 3-atm argon gas was used to generate a 500 nm bandwidth. They used modified spectral phase interferometry for direct electric-field reconstruction (M-SPIDER) and a pulse shaper for pulse compression. The shortest pulses directly from a laser system itself were generated by Binhammer *et al.*[174] who achieved 4.3 fs pulses directly from an oscillator. They used a Ti:Sa oscillator whose intracavity dispersion was controlled by a combination of double chirped mirror pairs and a CaF_2 prism sequence. This oscillator was capable of generating pulses spanning over 450 nm. They used SPIDER to measure the spectral phase distortion, and then used a prism-pair precompressor and a prism-based pulse shaper for pulse compression.

Control of octave-spanning laser pulses is essential for the quest of this dissertation since it eliminates the complexity of using multiple laser beams or tunable laser sources to achieve selective multiphoton excitation. The use of a phase

controlled octave-spanning laser does not require overlapping of two or more beams at the sample spatially or temporally as a multiple-beam system requires, an issue that usually necessitates an expert on optics and laser for everyday usage. Nor it needs tuning the excitation wavelength as a narrowband tunable laser does, because an octave pulse can cover all the molecular transitions through different multiphoton processes due to its broad bandwidth. Hence, the use of an octave-spanning laser source can eliminate the problems such as change of focusing and laser beam registration, phase compensation for each wavelength, and change of optics inside the laser cavity, caused by use of a tunable laser system, which also requires a laser expert to fix. In a word, a controllable and stable octave laser source is ideal for a non-expert to use. Therefore, it is the first step that needs to be demonstrated for this dissertation.

Here, we demonstrate automated pulse characterization and compression for three different quasi-octave laser systems with ultrabroad bandwidth (corresponding TL pulse duration ranging from 4.3 to 5.9 fs) through a grating-based pulse shaper without prism precompression using MIIPS. All the experiments demonstrate one direct MIIPS application: pulse compression and generation of ultrashort pulses.

Due to the broadband spectra of these laser systems, the generated SHG spectrum is also very broad. There is no good quality filter commercially available that transmits all SHG spectrum while blocks the fundamental one. Therefore, the SHG separation in the experimental setup is not as simple as that described in previous chapter.

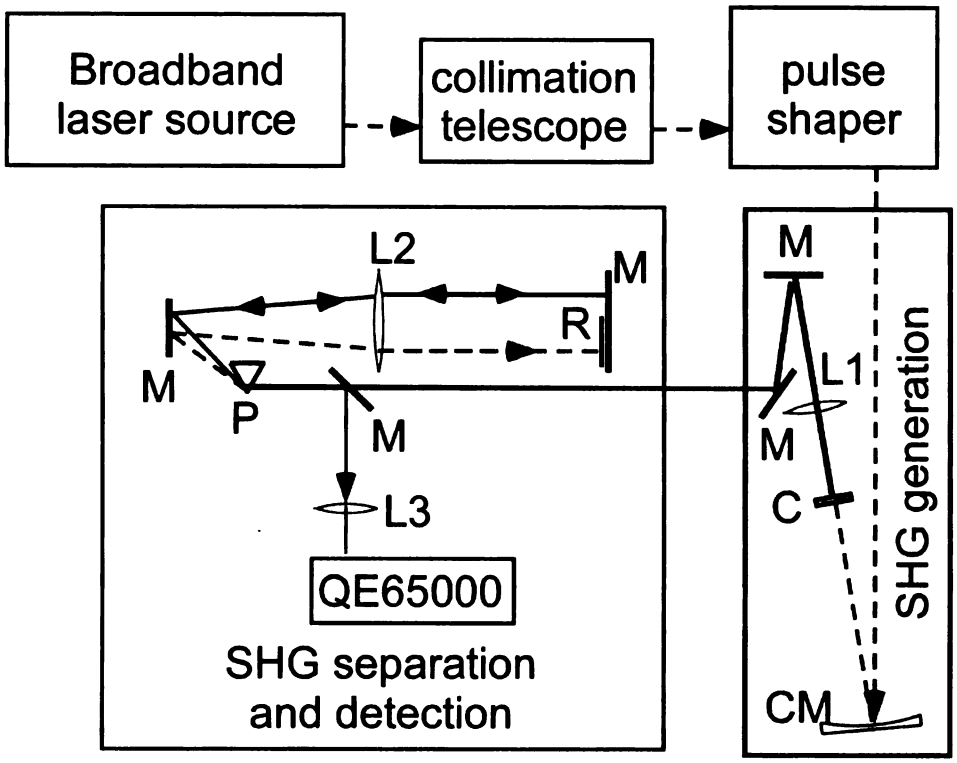

Fig. 4.1. Schematic setup for SHG generation, separation and detection. The dashed lines represent the fundamental beam and solid lines represent SHG signal. The SHG signal is generated after the curved mirror CM focuses the fundamental beam onto the KDP crystal C. Both the fundamental and SHG signal are collimated by lens L1 and directed into the SHG separation system: a prism-based 4*f* setup. After the quartz prism P, the fundamental and SHG signals are separated, and then both collimated by lens L2. A razor blade R is placed at the Fourier plane to block all the frequency components of the fundamental pulses while allow all the SHG frequencies to retro-reflect. After the SHG signal recombines, it is focused into a QE65000 spectrometer with lens L3. After the KDP crystal, all mirrors M are with protected aluminum coating. All the transmission optics are required to be made of quartz to avoid absorption of the SHG signal.

Fig 4.1 shows the whole apparatus for generation, separation and detection of the SHG signal. After the SHG was generated from a 20μm KDP crystal (C), both the SHG and the fundamental signals were collimated by a quartz lens L1 and the directed into the separation unit, a quartz-prism-based 4*f* Fourier Transform setup. At the Fourier Plane of this 4*f* setup, we put a razor blade (R) to block the fundamental frequency components without loss of SHG light. Since the SHG light was S-polarized, this separation unit was placed on a breadboard that is perpendicular

(vertical) to the optical table to avoid the use of polarization rotators that could not adequately manage the large spectral bandwidth. Finally, the SHG signal was directed into the spectrometer with another quartz lens.

4.1.1 Sub-5 fs laser oscillator system

This section shows the results of using sinusoidal MIIPS to compress the Venteon Ti:Sa oscillator system (see section 2.1.3), which is able to generate pulses with a spectrum that spans from 620 to 1050 nm. Figure 4.2(a) illustrates the spectrum of the fundamental pulses (in log scale) and the residual phase after compensation of the phase distortion. With such a residual phase, the calculated pulse duration would be 4.3 fs, which is confirmed by the interferometric autocorrelation trace shown as the inset of Fig 4.2(b). The longer wavelength edge of the spectrum looks noisier than the shorter wavelength because the spectrometer has lower spectral response and is thus less sensitive at longer wavelengths.

The corresponding SHG spectra (experimental and calculated) obtained for TL pulses are also shown in Fig 4.2(b). Note that the SHG spectrum starts at ~310 nm and ends at ~510 nm, spanning over 12,650 cm^{-1} (the spectrum span was measured from where the signals cannot be discriminated from noises, and the FW1/e^2M of the spectrum is ~136 nm). This is the broadest SHG signal ever generated directly from an oscillator using the conventional normal incidence on the KDP crystal. Other schemes for broad bandwidth SHG include the work by Baum *et al.*[175]. They used a NOPA system to generate visible pulses and used a confocal frequency doubling

scheme to generate a UV spectrum spanning ~10,720 cm^{-1}. In our setup the beam was directly focused on the KDP crystal. The excellent agreement between the experimental and calculated SHG spectra demonstrates MIIPS does measure and compensate the spectral phase of the system accurately.

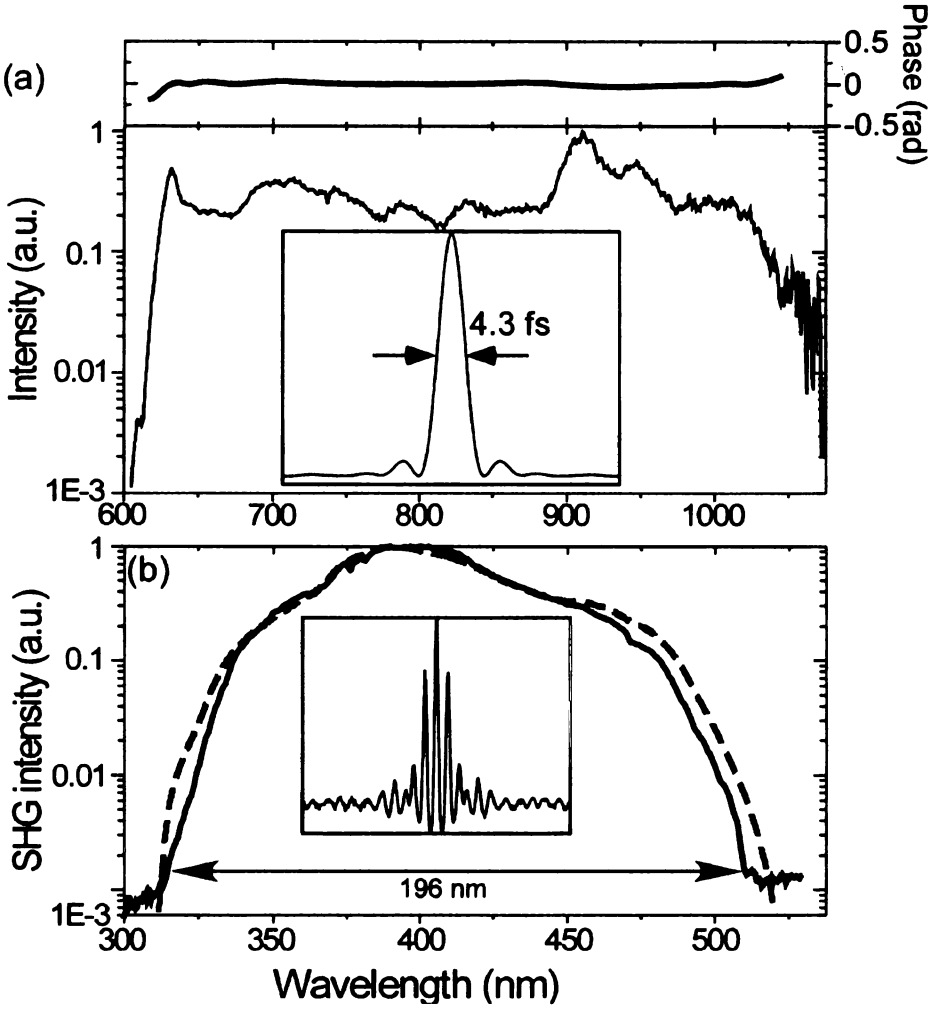

Fig. 4.2. (a) Spectrum of the fundamental pulses (log scale) and residual phase after MIIPS compensation. The inset shows the calculated temporal profile of the pulse with such residual phase. (b) Measured (solid line) and calculated (dashed line) SHG spectra (log scale) of the compensated pulses. Note that the calculation uses a Fourier Transform without any adjustable parameter and any broadband correction. The inset shows the experimental interferometric autocorrelation trace of the TL pulses, confirming the ~4.3 fs time duration.

Fig. 4.3(a) shows the fundamental spectrum and the MIIPS measured spectral phase from a different experiment. The spectrum is slightly different from that in Fig.

4.2 because we used a slightly different setting in the oscillator. In order to check the accuracy of the measurement, we used the measured phase and the fundamental spectrum to calculate the expected SHG spectrum.

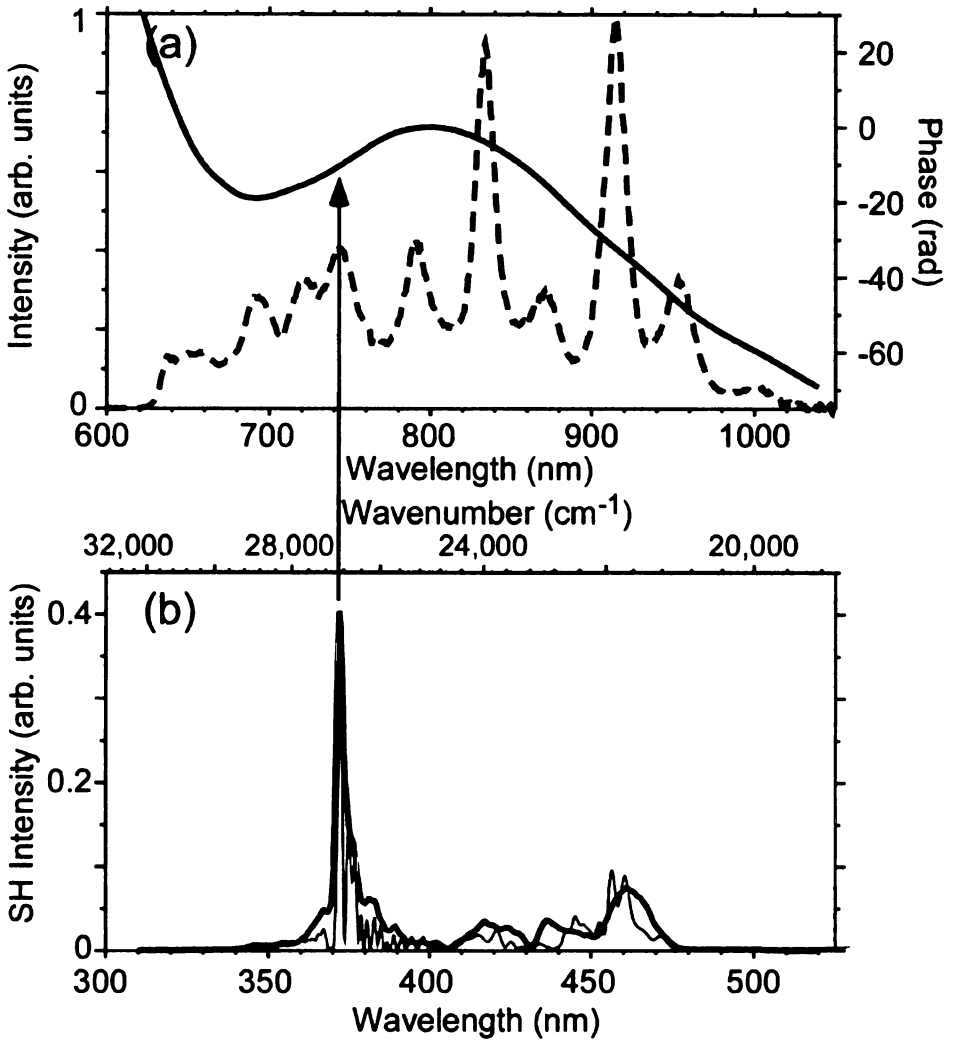

Fig. 4.3. (a) Spectrum of the fundamental pulses (dashed line) and measured phase (solid line). (b) Measured (black) and calculated (gray) SHG spectra of the compensated pulses. Both SHG spectra were normalized with respect to the TL SHG spectrum intensity.

Figure 4.3(b) shows very good agreement between the calculated spectrum and the experimentally measured SHG spectrum of the pulses prior to pulse compression. Some small features in the calculated spectrum are not present in our experimental data probably because of the low (~2.5 nm) spectrometer resolution. Since it is

well-known that the SHG spectrum depends on the spectral phase of the laser pulses[73, 74], the good match between experimental data and theoretical prediction demonstrates that the measured phase from MIIPS was accurate. As we can see from Fig. 4.3, the sharp peak in the SHG spectrum corresponds to the place in the fundamental spectrum where a point of inflection of the phase occurs.

Figure 4.4 demonstrates our ability to accurately deliver desired pulse shape with this ultrabroad bandwidth laser after MIIPS compensation. In these experiments, we chose several pseudorandom binary sequences[176], which will be discussed in detail in section 5.1, and generated binary sequences with points of symmetry and anti-symmetry in the frequency domain. Such binary phases generate sharp peaks at the point of symmetry and give very low background signal elsewhere, as was shown theoretically [177] and experimentally for pulses with less bandwith.[176] Figure 4.4 shows an example in which a 120-bit binary phase, containing 3 symmetrical sections, was used. The left section is symmetric to the center section and the right section is anti-symmetric to the center section. One can clearly see that two peaks were generated in the SHG spectrum at the positions exactly corresponding to the symmetry points of the binary phase. The left peak corresponds to the point of symmetry of phase function, and can be used as criteria to confirm the precision of the phase modulation [177]. Note that the two peaks generated by the binary phase function are not related to the peaks in the SHG spectrum of the uncompensated pulses. The width of the peaks was ~100 cm^{-1} and the separation between the two peaks was over 3,000 cm^{-1}. Other experiments show that the separation can be as large as 6,000 cm^{-1},

or as small as 300 cm^{-1}, and that the width of the peaks is limited by spectrometer resolution. The signal-to-noise ratio for the two peaks in Fig. 4.4 is ~15:1. This demonstrates our ability to accurately deliver the binary phase to the laser pulses, which can be used for selectively driving multi-photon processes such as two-photon excitation.

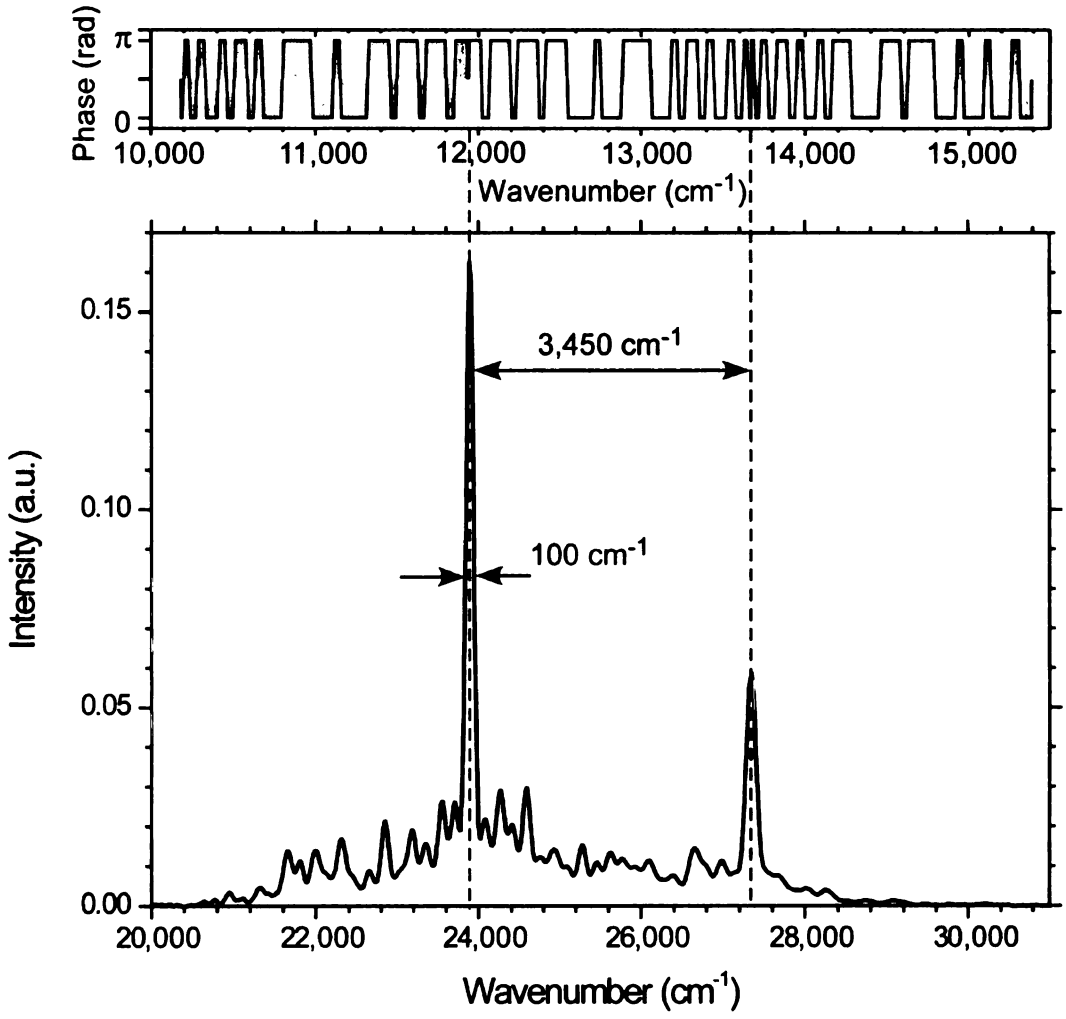

Fig. 4.4. Experimental selective SHG demonstration. Bottom: Second harmonic spectrum of binary phase shaped pulses (normalized with respect to the TL SHG spectrum intensity). Peaks occur at symmetry points of the phase, as expected Top: Pseudorandom 120 bit binary phase applied.

In some applications, the pulses are required to be very clean from any satellite pulses. As shown in the inset of Fig 4.2(a), there are still some obvious satellite pulses

with the highest peak intensity corresponding to ~6% of that of the major pulse, although it already has less satellite pulse than those in earlier publications.[94, 173, 174, 178] This comes from the irregularity of the fundamental spectrum.

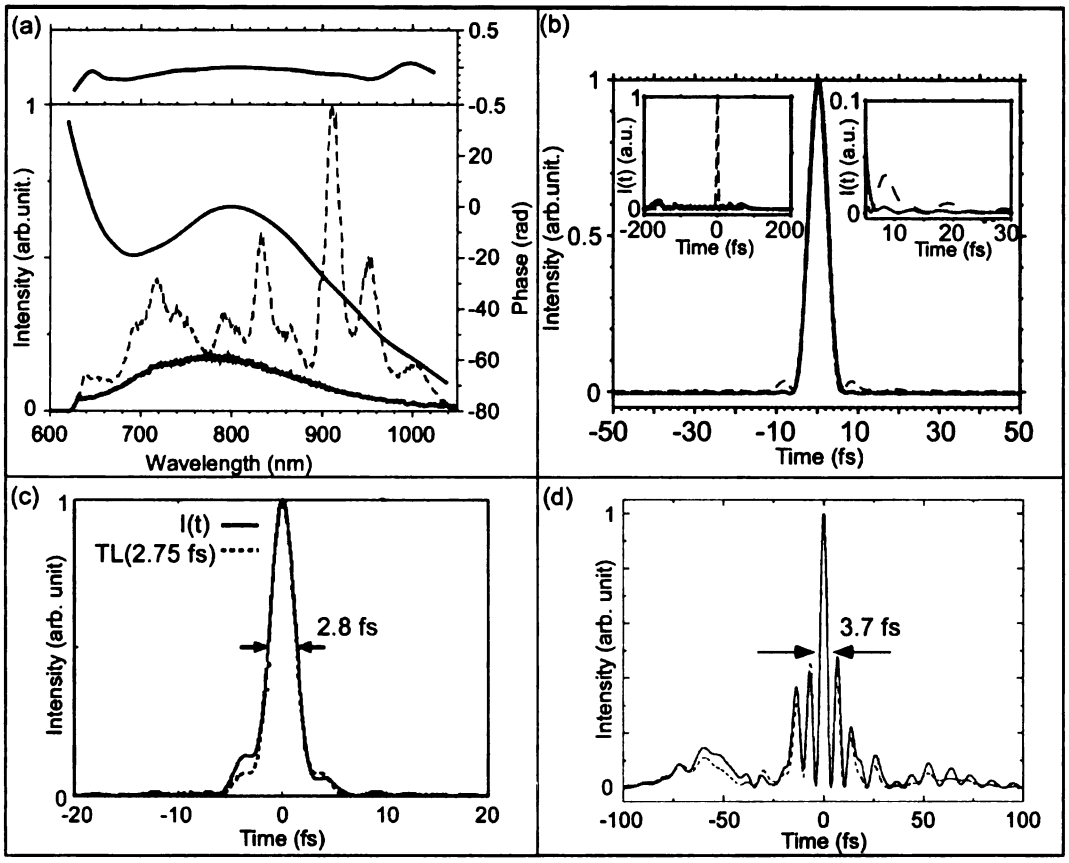

Fig. 4.5. (a) Spectrum of the fundamental pulses with (gray solid line) and without (dashed line) amplitude shaping. The black solid line shows the measured phase of the system. The top panel illustrates the residual phase after MIIPS compensation. (b) Calculated TL temporal profile for the pulses with (solid) and without (dashed) amplitude shaping. The left inset shows the calculated temporal profile with (dashed line) and without (solid line) MIIPS compensation. The right inset illustrates a zoom view of the satellite pulses. Note that the satellite pulses disappear when amplitude shaping is on. (c) The temporal profile of a 2.8 fs pulse reported by Yamashita and coworkers.[94] The solid line represents the reconstructed temporal profile for their experiments and dashed lines shows the ideal TL pulse profile. (d) The temporal profiles of a 3.7 fs pulse reported by Binhammer and coworkers.[178] The solid line represents the temporal profile for the pulse they generated and the dashed line represents the calculated pulse profile.

In order to get rid of those satellite pulses, we first introduce an amplitude mask to the pulse shaper to obtain the desired Gaussian spectral shape (in the frequency

domain) as shown in Fig. 4.5(a) and then use MIIPS to compensate the spectral phase of the pulses. In this case, the calculated temporal profile does not have any noticeable satellite pulses although the pulse duration is slightly increased to 5.2 fs (Fig 4.5(b)). Compare with the reported results for the 2.8 fs pulse[94] (Fig. 4.5(c)), which is clearly on a pedestal spans ~10 fs, and for the 3.7 fs pulse[178] (Fig. 4.5(d)), which has multiple satellite pulses, our pulses are obviously clean.

4.1.2 Sub-5 fs high intensity laser system

This section discusses the results of using sinusoidal MIIPS on the hollow waveguide system described in section 2.1.4 to generate high intensity sub-5 fs pulses[179]. Intense sub-10-fs laser pulses are required in high-field laser science for applications such as single attosecond pulse generation[180]. Spectral phase characterization of pulses generated from a hollow waveguide has been reported using SHG-FROG[181]. Adaptive phase characterization and correction have been accomplished using M-SPIDER and an SLM-based pulse shaper. [94, 182] Here I will present the use of MIIPS to achieve similar pulse compression results[183]. As mentioned in section 2.1.4, a grating-based pulse shaper with a 128-pixel phase-only SLM between the oscillator and amplifier is first used to eliminate all the spectral phase distortion through MIIPS before the laser pulses getting into the hollow core fiber. The optimized fiber output is directed into another grating-based pulse shaper with a 640-pixel dual-mask SLM and MIIPS was used again to correct all spectral phase distortions from the hollow core fiber and all other optics.

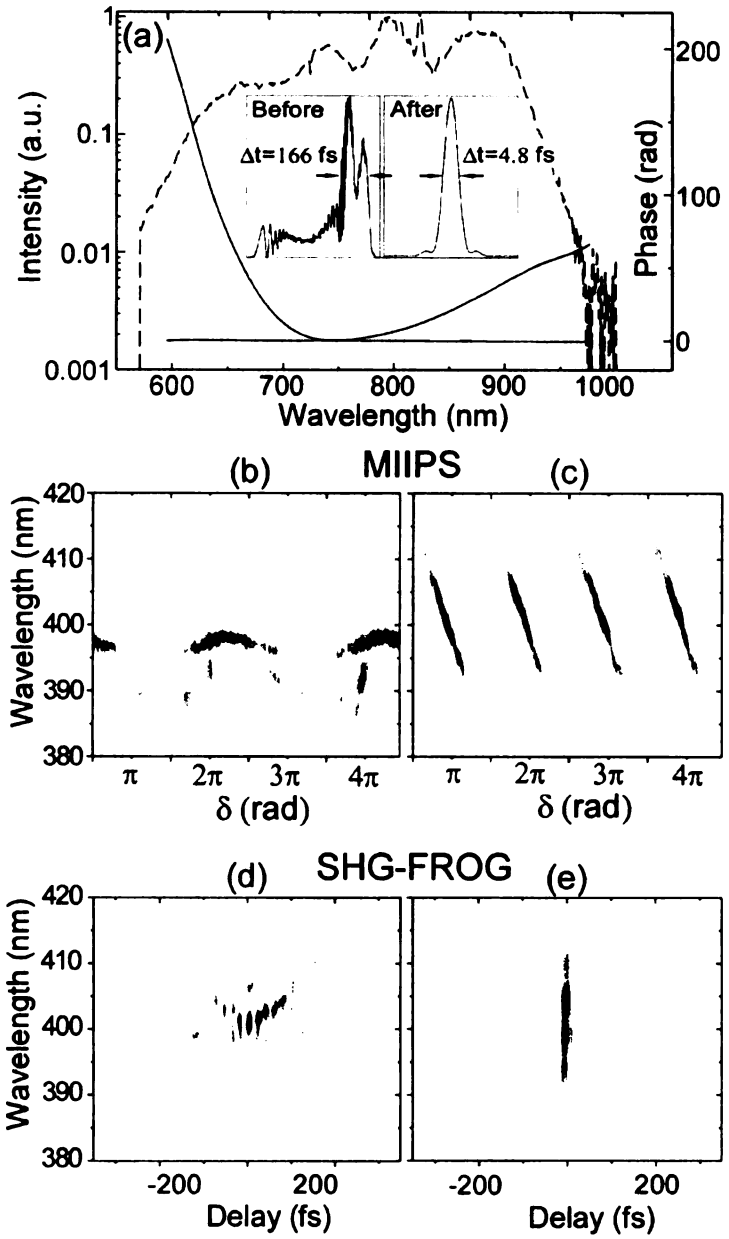

Fig. 4.6. MIIPS compression of continuum generated in an Ar-filled hollow-core fiber. The spectrum (dashed) and phase (solid) of the continuum, together with the temporal profile (inset) before and after spectral phase correction are shown. MIIPS and SHG-FROG traces of pulses before (b) and after MIIPS compression (c) are also shown. These pulses were obtained by blocking part of the continuum spectrum shown in (a) at the Fourier plane of the pulse shaper (see text). The parallel features in the MIIPS trace (c) indicate TL pulses. The remaining sub-pulses in the SHG-FROG trace (c) are a result of the deeply modulated spectrum.

Figure 4.6(a) shows the spectrum and spectral phase of continuum generated in an Argon-filled hollow-core fiber presented in section 2.1.4. The time duration of the

laser pulses was 166 and 4.8 fs before and after MIIPS compression, respectively (inset). The pulse energy of the compressed pulses was ~150 μJ/pulse. The pulse energy is limited by the throughput the second pulse shaper, which is ~50% due to the relatively low energy efficiency of the grating (~70%). When a grating with a higher efficiency is used, the pulse energy can be as high as ~300μJ/pulse. Fig 4.6(b) – (e) show a comparison of MIIPS and SHG-FROG traces of the output of the hollow-core fiber before and after MIIPS compression under such condition.

4.1.3 Sub-6 fs laser system with 2.12 GHz repetition rate

In communications, there has been a constant driver towards compressing information and sending it at the highest density possible. In this sense, there has been a drive for building sources that are modulated at GHz rates. Furthermore, it would be of interest to introduce information so that each pulse carries a large bite of information (binary bits). This section shows the results to use MIIPS correct the phase distortion for the Ti:Sa oscillator with 2.12 GHz repetition rate (see section 2.1.5). In this experiment, both sinusoidal and chirp MIIPS are employed to achieve the TL pulses. Fig. 4.7 shows the spectrum (dashed line) and the measured spectral phase (solid line) of the laser system, which includes the phase accumulated in the round-trips in the cavity and the phase distortions introduced by the optics and the medium in which the pulses propagate afterward. The residual phase after MIIPS spectral phase correction is illustrated in the top panel of Fig. 4.7. With such a residual phase, the calculated time duration of the pulse is ~5.9 fs. We achieved what would be

the fastest laser with the shortest pulses reported so far.

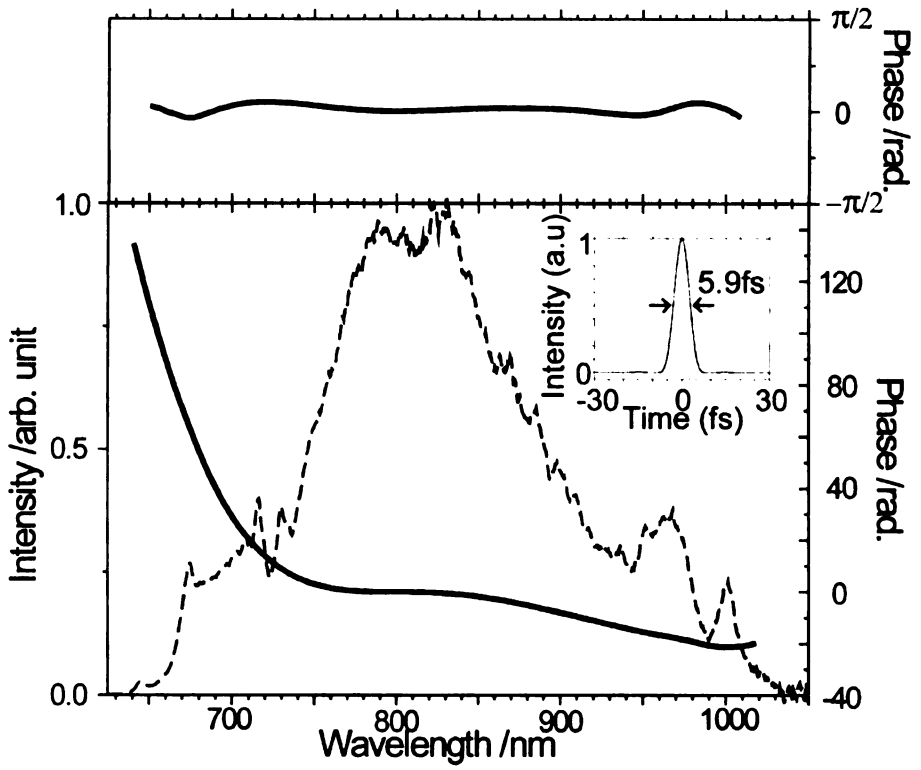

Fig. 4.7. Spectrum (dashed line) and measured spectral phase (solid line). The inset shows the calculated temporal profile. The top panel shows the residual phase after the spectral phase of the system was corrected by MIIPS.

After transform-limit pulses were achieved, a series of 8-bit binary phases defined in the frequency domain, i.e. only containing 0 and π values, were imposed to the pulses. Fig. 4.8 shows the experimental and calculated SHG spectra for two different 8-bit binary phases. The excellent match between the experimental and calculated SHG spectra provides an additional proof that the initial spectral phase distortions were accurately measured and corrected.

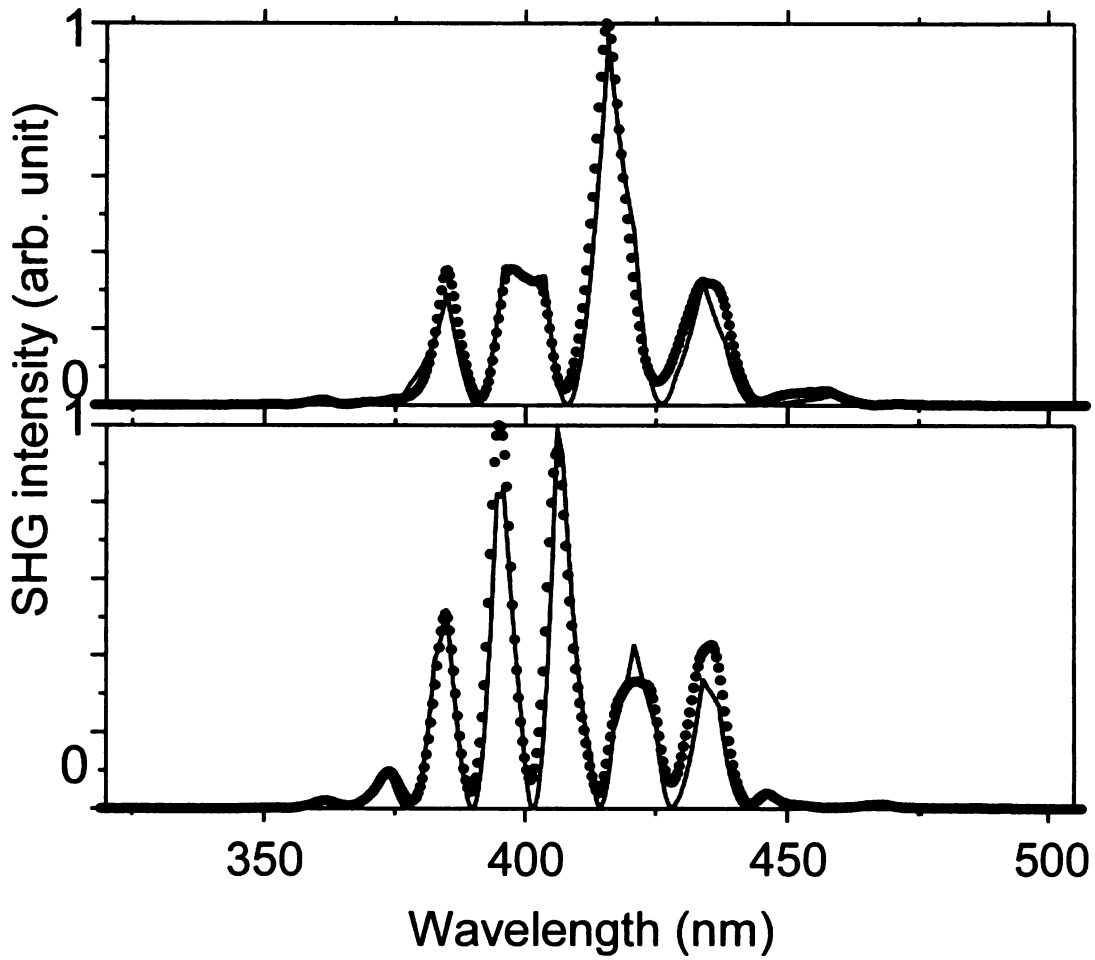

Fig. 4.8. Experimental (black dots) and calculated (gray line) SHG spectra corresponding two different 8-bit binary phases. Note the excellent agreement between calculation and experiment.

This laser system can be applied in rapid and encrypted information transmission, exploiting the high repetition rate of the oscillator and the fact that different binary phases result in unique NLO spectra, e.g., SHG spectra. A set of experiments were carried out and demonstrated that the current system can carry 64-bit encrypted information. Details of this project are discussed elsewhere.[184]

4.2 MIIPS applications for biological imaging

4.2.1. Measurement, compensation and reproducibility through high numerical aperture objectives

One of the greatest obstacles to fully developing the promising technique of multiphoton imaging is the significant amount of phase distortion introduced by high numerical aperture (NA) microscope objectives. To date, the characterization of such distortions has been accomplished for sub-10 fs pulses in objectives with NA up to 0.85,[185] and for up to 1.30 NA objectives if longer pulses are used.[186-189] Compensation of the quadratic term of the characterized distortions was accomplished in some cases through precompensation. However, higher order phase distortions, introduced by the objectives and even by the prisms necessary to precompensate for the quadratic phase distortions, cannot be compensated by these methods, nor can the phase distortions be quantified. The high order phase distortions deteriorate the efficiency of NLO process. Take two-photon excited fluorescence (TPEF), which is the prevailing NLO process in biological imaging, for example. The TPEF efficiency is expected to be inversely proportional to the pulse duration, or in other words, the more bandwidth the excitation pulses have, the more TPEF signal will be generated. However, no further signal increase is observed after the bandwidth of the pulses reaches ~30 nm, if high order phase distortion is not corrected. This is the main reason that ~100 fs laser pulses or even picosecond pulses are prevalent in the field of biological imaging. In this section, we demonstrate that MIIPS can successfully

quantify and compensate for all orders of arbitrary phase distortions introduced into a sub-12 fs pulse by high NA microscope objectives.

For this procedure, a periscope is used to bring the laser beam into the rear port of a Nikon TE2000-U inverted microscope. The beam is reflected upward through the objective and focused onto the SHG crystal. The three objectives used are a Nikon Plan Fluor ELWD 20x/0.45 NA objective, a Nikon Plan Fluor ELWD 40x/0.60 NA objective, and a Nikon Plan Apo TIRF oil immersion 60x/1.45 NA objective (Nikon immersion oil, Type NF is used.).

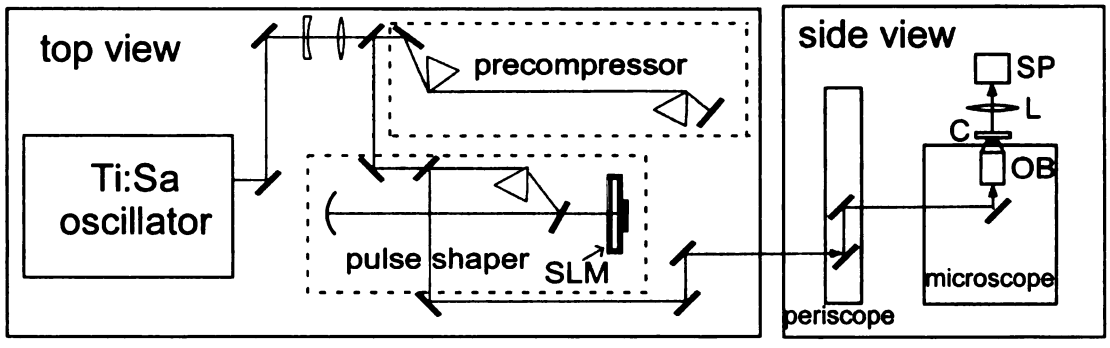

Fig. 4.9. Setup for compensation of phase distortion introduced by the high NA objectives. The pulses from the oscillator first pass through a precompressor consisting of two SF-10 prisms and are directed into a prism based pulse shaper with a 128-pixel P&A SLM. The beam then gets into the microscope through a periscope. After reflected by an internal mirror inside the microscope, the pulses are focused on the BBO crystal (C) by different objectives OB. The generated SHG signal is collected by a lens L into a spectrometer SP.

MIIPS alone is sufficient to compensate for the phase distortions introduced by the 20x/0.45 NA and 40x/0.60 NA microscope objectives (data not shown). To allow for the best compensation of higher order phase distortion introduced by the 60x/1.45 NA objective, a pair of SF10 prisms is used to reduce the quadratic phase contributions (~10^4 fs^2). The schematic setup of this experiment is illustrated in Fig. 4.9.

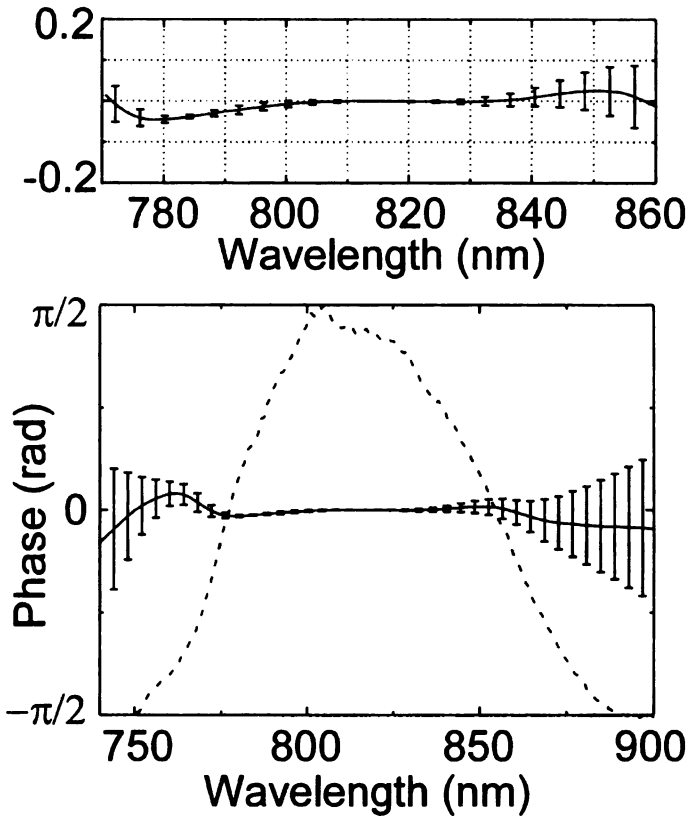

Fig. 4.10. Compensation of spectral phase distortions caused by a 60x/1.45 NA objective. The error bars indicate ± 1 standard deviation. The lower panel shows the full range of data, while the upper panel shows the same data over the FWHM of the pulse, on a reduced scale.

Figure 4.10 shows the compensation results for the 60x/1.45 NA objective. In both panels, the solid line shows the average phase residue of five independent measurements. The errors bars show the standard deviation for every fifth data point. The lower panel shows the full set of acquired data. The upper panel shows the same data over the FWHM with a reduced scale. Note that the phase is compensated to within 0.1 rad over the entire bandwidth of the pulse (770-860 nm), indicating that the distortions introduced by high NA objectives are well compensated over that range. We highlight the extremely narrow standard deviation observed in the reduced range, providing evidence of a very high degree of reproducibility of the MIIPS method, even when highly dispersive materials are utilized. The statistical phase error, defined

in the same way as in section 3.2.3, for the 60x/1.45 NA objective was calculated to be 0.026 rad over the full range of data, where the uncompensated phase distortion was ~100 rad. Considering the significant degree of distortion introduced by this high NA objective, the precision by which phase is measured by MIIPS is excellent although this number is slightly higher than that is shown in section 3.2.3.

4.2.2 MIIPS measurements after transmission through biological tissue

One of the most popular applications for femtosecond laser pulses is nonlinear biomedical imaging. Methods such as two-photon microscopy take advantage of the ability of near-infrared lasers to travel through scattering biological tissue and provide high-resolution images[190]. The development of techniques for optimized depth-resolved imaging, as well as surgical procedures involving femtosecond lasers, will require accurate characterization of pulses after they transmit through biological samples. However, when a laser beam transmits through a scattering medium such as biological tissue, the majority of the photons is scattered and the number of ballistic photons, which still maintain theirs directionality and coherence, drops exponentially with the depth of the medium. This occurs as a result of the presence of macroscopic and microscopic cellular constituents, fat globules, and refractive index mismatch between intra- and extra-cellular fluids. Therefore, it is impossible to use pulse characterization methods that require overlapping two or more beams.

Here we demonstrate the ability of the MIIPS method to measure spectral phase deformations caused by transmission through scattering biological tissue. The procedure involves measuring and correcting phase distortions inherent in the sub-12

femtosecond laser pulses to obtain TL pulses, and then comparing the spectral phase obtained when the laser transmits through a 500-μm slice of raw chicken breast tissue or through a similar thickness of glass. In an early work of the Dantus group, Dela Cruz *et. al.* [76]demonstrated that the degree of scattering has very little effect on the spectral phases, although the overall signal intensity depends largely on it. This confirms that the ballistic photons or coherent component of the electric field, maintain phase information as the laser penetrates a turbid, scattering medium. Fig. 4.11(a) and (b) show the MIIPS traces obtained for glass and tissue samples, respectively. As expected, a reduction in signal to noise ratio resulting from the exponential decay of ballistic photons as the pulse transmits through several scattering lengths of tissue was observed. Notwithstanding this limitation, phase information is still comparable to that obtained when light goes through an optical medium like glass. The presence of tissue slightly decreases the range of wavelengths that can be compensated by MIIPS, but the fact remains that the method works. Fig. 4.11(c) shows the phase residue, averaged over five trials, of the pulse as it went through glass and tissue. Note that the phase is compensated to within 0.02 rad over the entire FWHM of the pulse. MIIPS can fully compensate for distortions introduced by a scattering medium. More significantly, the MIIPS method corrects spectral phase distortions at the position of the sample.

Accurate phase compensation and accurate phase delivery at the target is important for femtosecond laser applications. This capability allows the Dantus group to perform selective functional imaging through biological tissue.[76] Simulations

show[20] that even for signal to noise ratios as low as one, it is possible to measure the spectral phase with high precision by smoothing the 2D MIIPS data before analysis. The good resistance to noise and independence of mode quality are additional significant advantages of the MIIPS method. MIIPS method is also applied to other biological systems. For example, we have utilized the MIIPS method to measure the GDD and TOD of vitreous humor and cornea-lens complex of a bovine eye[191].

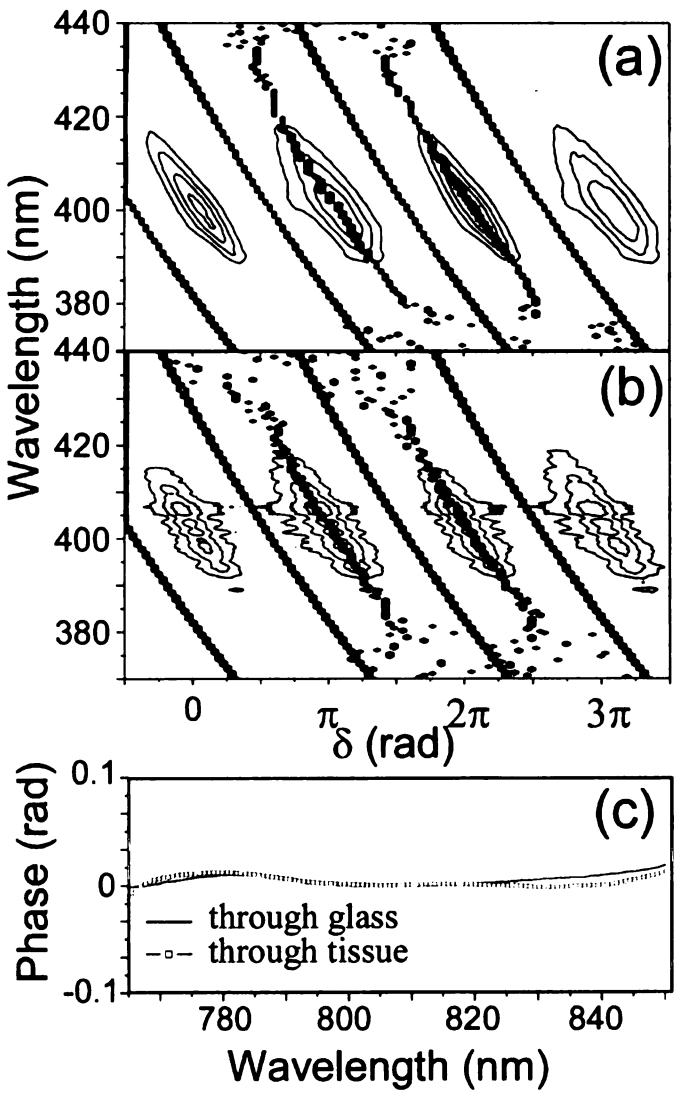

Fig. 4.11. MIIPS measurement through scattering biological tissue. Panels (a) and (b) show MIIPS traces of compensated pulses without and with tissue, respectively. While the overall signal to noise ratio is significantly decreased, similar phase information is obtained. (c) shows the residual phase after MIIPS compensation with and without tissue.

4.3 Conclusion

In this chapter, the compression of several quasi-octave laser sources using MIIPS was demonstrated, this work setting a world record in terms of the broadest SHG bandwidth to be generated and the shortest pulses to be generated from a GHz laser. Pulse compression by MIIPS was able to generate 4.3 ~ 5.9 fs pulses that reach the theoretical predicted TL pulse duration, regardless the pulse intensity and repetition rate. This ability guarantees the reproducibility for selective multiphoton excitations by accurate phase and/or amplitude shaping and usage of the full bandwidth of quasi-octave laser sources, as presented in next chapter. The attempt to control a real octave laser source is under investigation in the Dantus group and will be soon demonstrated.

In this chapter, MIIPS was also used to solve some technical problems faced when applying ultrashort femtosecond pulses in biological applications in this chapter. The correction of all orders of phase distortion introduced by the high NA objectives was demonstrated. This ability allows the use of sub-12 fs laser pulses with such objectives for reproducible high-resolution imaging without losing the advantage of the higher NLO efficiency given by the bandwidth of the short pulses. The accurate phase measurement after scattering media by MIIPS demonstrates the ability to achieve TL or other accurately shaped pulses at the sample even when the pulses propagate through biological tissue, providing a good starting point for deep tissue (few millimeter) imaging and laser surgeries.

Chapter 5

Selective molecular excitation

Controlling laser-matter interactions, which are central to imaging, molecular recognition, nonlinear optics and material processing, is an active area of research that has lately migrated to the use of ultrashort pulses because of their great efficiency at inducing nonlinear optical (NLO) processes. Controlling NLO excitation requires the design of laser pulses capable of inducing constructive interference between paths that lead to excitation at the desired frequency, while inducing destructive interference between all other paths. Although it is possible to calculate NLO observables such as the n^{th}-harmonic spectrum for a given laser field and material, the inverse problem, where one obtains the optimal field explicitly given a desired non-trivial target and an operator expressing the nonlinear interaction between light and matter, has remained in the realm of optimal control theory [192]. A theoretical and experimentally viable solution for selective non-resonant NLO excitation would have broad applications, for example in single-beam selective two-photon microscopy and in high resolution CARS microscopy. The lack of a mathematical expression that links the desired selectivity to the required properties of the field has motivated the use of empirical methods, such as computer based search algorithms, for exploring the nearly infinite possible combinations of phase and amplitude functions which define a shaped laser pulse [34]. Here in this chapter, I present how to use BPS to achieve selective NLO excitation. The first section presents theoretical and experimental demonstrations in selective SHG and SRS excitation that represent the highest resolution and the best

contrast ratio yet reported (section5.1). SHG is chosen since the same two-photon fields that generate the selective SHG can be directly applied in other two-photon processes, such as TPEF, the prevailing NLO process for biological imaging. The SRS is selected because it can be consider the first half of the CARS process, which is able to probe the molecular vibrations and give the fingerprint to identify different molecules. Applications of selective molecular excitation through BPS for real problems such as two-photon spectroscopy without a tunable laser source (section 5.2) and CARS spectroscopy with a single laser source (section 5.3), will then be presented.

5.1 Pseudorandom BPS for NLO processes

5.1.1 Introduction

This section presents theoretical and experimental results in selective NLO excitation that represent the highest resolution and the best contrast ratio yet reported, by orders of magnitude. These results derive from a physical model for NLO, as well as from the unusual combination of nonlinear optics and number theory as explained below. The goal is not only to be able to generate a strong signal at a desired wavelength (Fig. 5.1(a)), but also to suppress background elsewhere in the nonlinear spectra (Fig. 5.1(b)). The specific NLO processes under investigation in this section are SHG and SRS, selected for their wide applications in spectroscopy and microscopy. For both SHG and SRS, we defined a narrow spectral window: the integrated intensity of the spectrum inside this window was defined as signal S, while

the integrated intensity of the spectrum outside the window was defined as background B. The ratio between S and B is defined as the contrast ratio (CR), which is the most important fitness function for selective SHG and SRS throughout this section. We also use traditional signal to noise ratio (S/N), which compare the peak intensity of the signal to the average intensity of the background. For both CR and S/N factors, the larger the value, the better the selectivity of SHG or SRS at certain frequency.

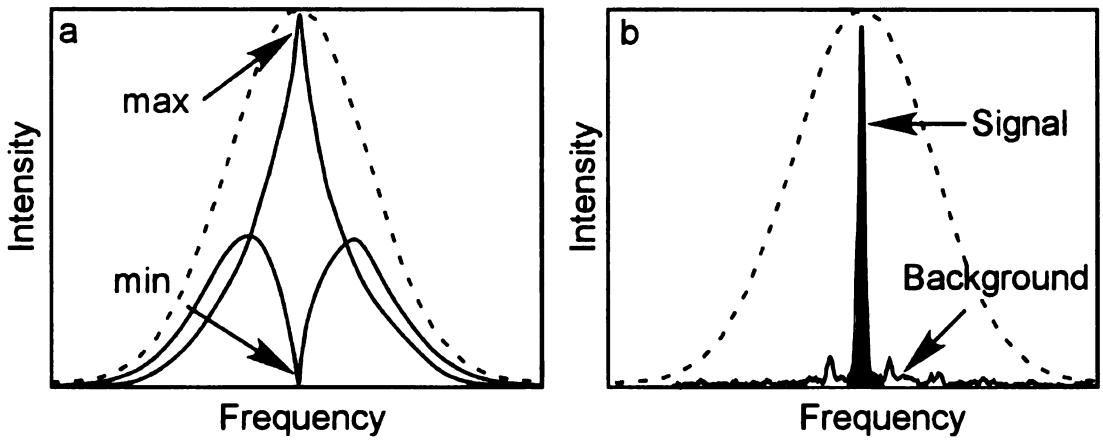

Fig.5.1. Nonlinear spectra of phase modulated pulses. The dashed line is the spectrum of a Gaussian transform-limited (flat spectral phase) pulse. (a) Maximization or minimization of nonlinear spectra at a selected frequency. (b) Generation of a narrow peak at a selected frequency with low background (the goal of this project).

A number of pioneers in the fields of physics and optics have already contributed to this topic. We highlight the work of Weiner who used periodically repeated binary m-sequences and Dammann gratings to selectively excite coherent phonons in crystals.[27, 28] The goal was to generate a pulse train in the time domain to enhance impulsive SRS excitation. Weiner also used shifted m-sequences for a proposed code-division multiple-access network, and used m-sequences and Hadamard codes to control SHG in two-photon diodes and in periodically poled thin or thick crystals.[78, 193] The goal

was to maximize or minimize SHG at the central frequency. Silberberg used sinusoidal phase modulation and step modulation for two-photon excitation (2PE) of atoms [71, 72]. He also used sinusoids, step-functions, and phase gates [194, 195] to narrow coherent anti-Stokes Raman scattering spectra and to suppress non-resonant contributions, taking advantage of the symmetry of phase modulation and of the interference between resonant and non resonant nonlinear effects.[196, 197] Weiner and Silberberg's research focused on maximizing or minimizing the signal at one frequency without requiring the suppression of the signal at all other frequencies (Fig 5.1 (a)). Optimizing the signal at one frequency while minimizing signal at other frequencies is a much more challenging problem and is what we solve here.

Different approaches have been introduced to achieve selective SRS. One technique involves a pair of chirped pulses.[61, 198] In this case, interference between frequencies in the two pulses causes amplitude modulation. The use of GA's is another widely used approach. For example, a group of experiments[60, 199, 200] and related theory[201] uses a very intense field shaped by a GA with spectral amplitude and phase modulation. The success of such method depends largely on the nature of the search space, or the distribution of good solutions over the set of all possible pulse shapes. In the ideal case of infinitely precise control of a pulse's shape and in the absence of experimental noise, the search space for a given nonlinear process is convex, meaning that each possible pulse shape can be transformed into a slightly better pulse shape by an infinitesimally small change to just one parameter, allowing the best possible pulse shape (the global maximum) to be quickly reached through a

series of small changes[202]. However, the current method of controlling a pulse's shape, with an SLM, can provide only a finite number of possible pulse shapes, usually about 100 SLM pixels (N), 1000 reliable phase values (N_φ), and 1000 reliable amplitude values (N_A). The set of possible pulse shapes is no longer continuous, and therefore the search space is no longer convex. Instead of an easy path toward the optimum solutions, we have dead-end solutions called local maxima, which are suboptimal but must be dramatically changed to reach a better solution. Under experimental conditions, the huge number of variables makes the search for an optimal pulse shape a daunting task; the number of pulse shapes possible using the SLM described above is $(N_\varphi \times N_A)^N = 10^{600}$. A search space this size makes all but the most convex problems extremely difficult.

As I described in the previous chapter, we first use BPS to reduce the number of variables to make the problem more manageable, while making sure not to eliminate all the best solutions from the search space. With BPS, we eliminate redundancy while preserving control over the parts of a pulse shape that contribute to our desired nonlinear effects. We have shown that the use of BPS [75], in which no amplitude shaping is used and the only two values of spectral phase allowed are 0 or π, allows us to reduce the problem to that of constructive and destructive interference between frequencies.[73, 74, 81] The search space becomes not only dramatically smaller but also more readily analyzable and, as we will show, amenable to search space mapping. Therefore, our first step is to map the search space and then use the characteristics from the map to generate the solutions to our goal.

5.1.2 Experimental setup

We measured SHG and SRS spectra of pulses from the Ti:Sa oscillator described in section 2.1.1. The beam went through a folded pulse pre-compressor consisting of a pair of SF10 prisms and then into a pulse shaper. The pulse shaper consisted of a SF10 and a BK7 prism, a 200-mm focal length spherical mirror, and a dual-mask SLM (CRI, Inc., SLM-256) in the folded geometry, as described in section 2.2. Two prisms were used to cover more SLM pixels. The MIIPS method was used for all the experiments to achieve TL pulses at the target within 0.05 radian precision. For the SHG experiments, the beam was focused on a 10 μm β-BBO type I crystal and the signal was recorded with a spectrometer of spectral resolution ~0.3 nm. For the SRS experiments, the beam was introduced into a balanced Michelson interferometer (FR-103PD, Femtochrome Research, Inc). SRS spectra were retrieved from Fourier transformation of intensity autocorrelation traces obtained by a two-photon diode.

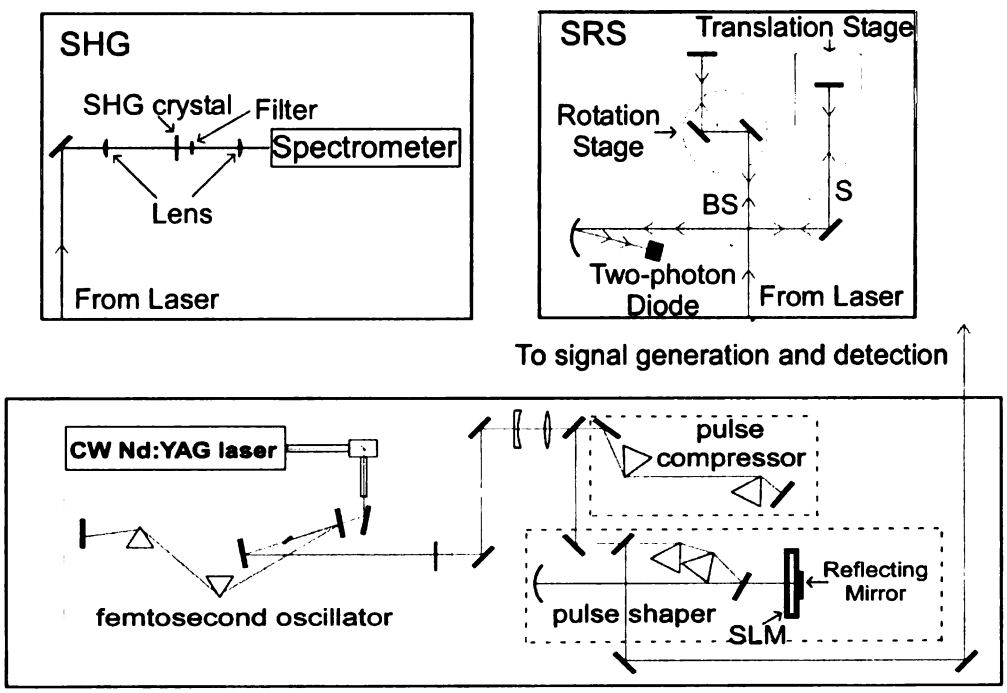

Fig.5.2. Schematic experimental setup. BS: beamsplitter; S: beamsplitter substrate only.

5.1.3 Mapping of the search space for SHG and SRS

In this section, we investigate all possible 16-bit BP functions for their ability to generate selective SHG and SRS excitation, and examine the distribution of the BP functions that best create narrow peaks at desired locations in the SHG and SRS spectra, i.e., map the search spaces.

We applied each phase to the center spectral region of our femtosecond laser pulses, using amplitude shaping to eliminate the signal outside of this spectral window. Each of the 16 logical bits covered 4 SLM pixels for SHG and 3 SLM pixels for SRS. We defined a spectral window with width 1.3 nm or 50 cm^{-1} for SHG and SRS, respectively, to calculate the CR factors as the fitness function for each BP. For SRS, we disregarded the spectral region below 150 cm^{-1}, a region that is essentially unaffected by phase shaping.

To visualize the search space, we transformed each binary phase function into an (x,y) coordinate on a two-dimensional plot called a search space map. We first translated each binary phase function (for example, $\pi 0 \pi\pi 00000 \pi 00 \pi\pi\pi 0$) into a binary sequence (1011000001001110_2 in this example), then divided this sequence into two halves ($x = 10110000_2$, $y = 01001110_2$). The binary x- and y-halves of the sequence were directly converted to their base-10 equivalents ($x = 13_{10}$, $y = 114_{10}$). The resulting (x,y) coordinate pair corresponds to a point on a 2D map, which is assigned a color based on the experimental performance of the original binary phase function; white if the CR value was high, down to black for a very low CR. For the SHG search space maps, the x portion (first half) of the binary sequence was reversed

before conversion to decimal. We applied this reversal to highlight the different roles of symmetry in SHG as opposed to SRS, as discussed below.

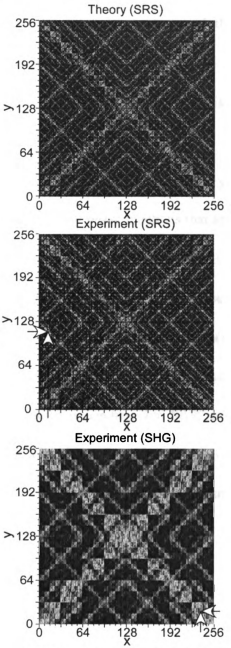

Fig. 5.3. Calculated (top) and experimental mapping of selective SRS (middle) and SHG (bottom) at the center of the nonlinear spectrum (see Fig. 5.1(b)). X and y coordinates are the decimal representations of the left and right halves of the binary phase sequences, respectively, and the grayscale represents the value of the fitness function CR. Here, phase sequences with high CR values are shown in white, while sequences with low CR values are shown in black. Note the excellent agreement between the experiments and the theoretical prediction. Arrows point to the locations of the global maxima.

Figure 5.3 shows calculated and experimental SRS search spaces and experimental SHG search spaces, for signal windows placed in the middle of the available nonlinear spectra. The binary phase sequence with the highest CR ratio for SRS is π0ππ00000π00πππ0, which is mapped to (13,114) as described above, while the binary phase sequence with the highest CR for SHG is π0ππ0πππ000π00ππ, mapped to (237,19).

Many of the good phase functions are found on the lines y=x and $y=x_{max}-x$. For the SHG maps, these lines contain only phase functions that are reflection symmetric or antisymmetric about Ω, the frequency for which the NLO is being maximized; i.e., $\phi_{SHG}(\Omega+\omega)=\pm\phi_{SHG}(\Omega-\omega)$, while for SRS the phases on these lines have translation symmetry or anti-symmetry about Ω; that is, $\phi_{SRS}(\omega)=\pm\phi_{SRS}(\Omega+\omega)$. These lines are dominant features on the search space maps, agreeing not only with previous experimental observation by other researchers for SRS[27]and SHG[71], but also with theoretical predictions of the role of symmetry in constructing phase functions for optimizing nonlinear optical processes.[20] Note that even among symmetric phases on the lines of the search space map, there are phases with poor CR ratios. To achieve the best CR ratios among symmetric phases one half of the binary phase function, $\phi_{SHG}(\Omega+\omega)$ or $\phi_{SRS}(\omega)$, must contain a pseudorandom series of bit flips [20]. The search space map also contains interesting fractal structure (Fig. 5.4), as evidenced by the similarity of the structures as one zooms in on a region of the data. This fractal quality results form the symmetry inherent to low order NLO processes and can be used to further reduce the search space as a small region of the search space could predict the

whole distribution of the map.

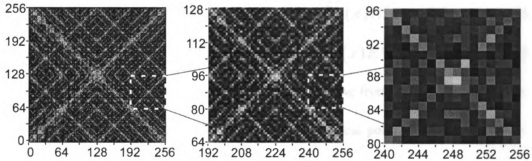

Fig. 5.4. Fractal structure of the search space map. Left: experimental search space map for SRS, middle: zoom-in view of the left panel dashed region, right: zoom-in view of the middle panel dashed region. All three panels show the same structure.

As the target signal wavelength is scanned across the nonlinear spectrum, the center of symmetry that maximizes this signal is scanned across the phase function. Movie 1 and movie 2 in reference [176] show the SHG and SRS maps when the signal window is scanned from one end of the spectrum to the other. In each case, the phase functions with the highest CR ratios are located on lines that contain only symmetric or antisymmetric phases, with the locations of the lines changing to reflect the changing location of the center of symmetry.

5.1.4 Synthesis of optimized electric field using pseudorandom BP

Our goal is to synthesize the optimal electric field $E^{(2)}$ to cause 2PE, e.g., SHG, and $E^{(0)}$ to cause SRS. These fields are not molecule-specific; nonlinear signals are proportional to the absolute value of square of these fields and the corresponding molecular cross sections. We define here the two-photon field spectrum, $I^{(2)}=|E^{(2)}|^2$ for 2PE, and the intensity spectrum $I^{(0)}=|E^{(0)}|^2$ for SRS, which can be calculated according to the convolution theorem by self-convolution (Eq. (5.1)) and by autocorrelation

(Eq. (5.2)) of the fundamental field $E(\omega)$ in the frequency domain, respectively:

$$E^{(2)}(\omega) = \int E(t)^2 \exp(i\omega t)dt = \int E(x)E(\omega - x)dx \quad (5.1)$$

$$E^{(0)}(\omega) = \int |E(t)|^2 \exp(i\omega t)dt = \int E(x)E^*(x - \omega)dx \quad (5.2)$$

The role of phase symmetry in nonlinear optics resulting from these expressions has been comprehensively analyzed for BPS from a theoretical point of view by Lozovoy [20], and have been experimental proofed by the search space mapping study described in the previous section.

We find that the problem of maximizing NLO signal at one frequency while minimizing the background elsewhere can be framed in terms of the number theory problem of finding low-autocorrelation binary sequences. To see this link, we first simplify the problem for theoretical analysis by assuming that the spectrum of the fundamental field is unity for all frequencies, and we concentrate on the electric field, leaving molecular cross sections aside. The use of binary phase shaping, in which the spectral phase is limited to values of 0 or π, allows us to represent the electric field (E_i) in the frequency domain as a sequence of values +1 and -1, respectively. This mathematical object forms a Galois group, $GF(2^N)$, where N is the number of bits in the sequence. Eq. (5.1) and (5.2) can be rewritten for Galois fields as Eq. (5.3) and (5.4).

$$E^{(2)}_{i+j} = \sum E_i E_j \; ; i = 0..N-1, j = 0..N-1 \quad (5.3)$$

$$E^{(0)}_{i-j} = \sum E_i E_j^* \; ; i = 0..N-1, j = i..N-1 \quad (5.4)$$

Eq. (5.3)and (5.4) summarize how these pseudorandom Galois fields can be used to suppress NLO excitation at any desired frequency, i.e., simply having an equal number of +1 and -1 contributions in the sum. Binary sequences with minimum

autocorrelation will minimize the sum for every frequency; and when symmetrized or antisymmetrized, they will produce maximum NLO excitation at their center of symmetry while suppressing excitation elsewhere, exactly as desired in selective NLO excitation. The amplitude of the resulting spectrum is bound at all frequencies by the spectrum of a TL pulse E_i=1 such that $E^{(2)}_{N\pm i} = E^{(0)}_i = N - i$. We can therefore produce selective NLO excitation through the use of minimum-autocorrelation binary sequences, which are freely available thanks to years of research in the well-established fields of communications engineering and statistical mechanics [203].

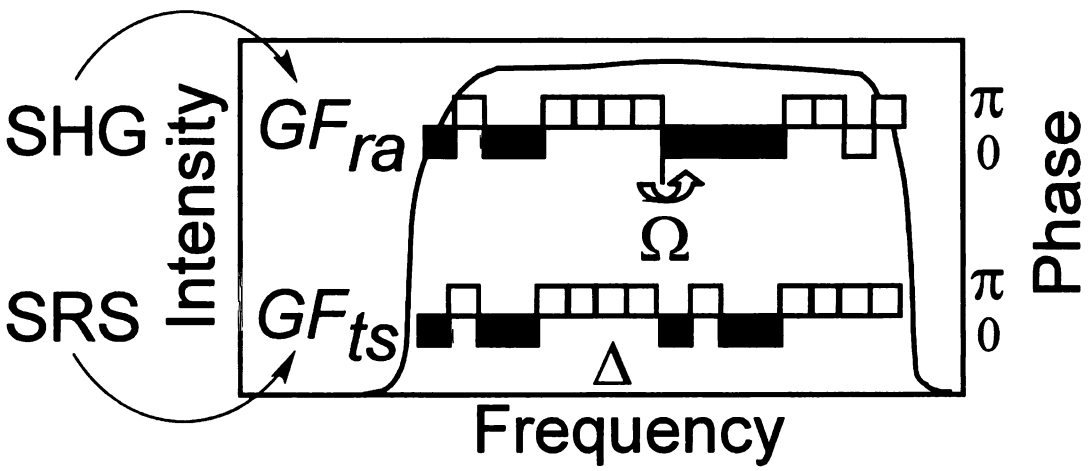

Fig. .5.5. 8-bit pseudorandom BP applied to femtosecond laser pulses for selective SHG or SRS at the center of the spectrum. The top phase, designed for selective SHG, is formed by reflection and anti-symmetrization of the pseudorandom sequence. The bottom phase, designed for selective SRS, is formed by translation symmetrization.

Figure 5.5 describes how to use phase shaping of an ultrashort pulse to achieve selective NLO excitation. First, we choose a pseudorandom binary number from a list of sequences with minimal correlation [204] (for N=8, for example, it is 10110000_2). Second, we transform the binary number into a $GF(2^N)$ sequence (-+--++++). Third, we symmetrize (or antisymmetrize) the GF depending on the nonlinear process, using

reflection $raGF(2^N)$ for 2PE and translation $tsGF(2^N)$ for SRS, producing a phase function that will cause the desired selective NLO excitation.

Using the above method, we have tested solutions of Eq. (5.3)and (5.4) using binary sequences of length up to 608 bits theoretically. The results are described in terms of two parameters: CR and S/N as defined previously in Fig.5.1. The optimal 608-pixel solution created using a symmetrized low-autocorrelation 304-bit binary sequence is +++++-+-+++--+++-+---++---+-++++---+--+++-+----++--+-+---+--+---+--

-------++-++--+--++-++-----++++---+++++--++++------+--+--+-+------+-+++-----+-++

++++-+++-+-+----+-+--+----+-+-+++++---+++-+-+--+-++--+-+--+--+-++-+-++---++--

-++---++-+-+-+-+++-+++---+-----++--+-++++-++---+--+-++++-++--+----+--++-++++

+-+-. The resulting Galois field gives an S/N of 1697:1 or 1400:1, and a CR of 1.4 or 2.3 for 2PE or SRS, respectively. These pseudorandom binary sequences provide at least 3 or 7 times better S/N and CR than the average completely random binary phase function for a given number of pixels for 2PE and SRS, respectively. This level of performance would be virtually impossible to achieve using random binary phase functions. This performance would also be extremely difficult to reproduce using a learning algorithm controlled pulse shaper; although some of the low-autocorrelation binary sequences given in [204] were found using learning algorithms, finding low-autocorrelation binary sequences is a very challenging problem that requires the use of multiprocessor computers. The longest low-autocorrelation binary sequences (with $>10^6$ digits) have been designed using Legendre sequences [205].

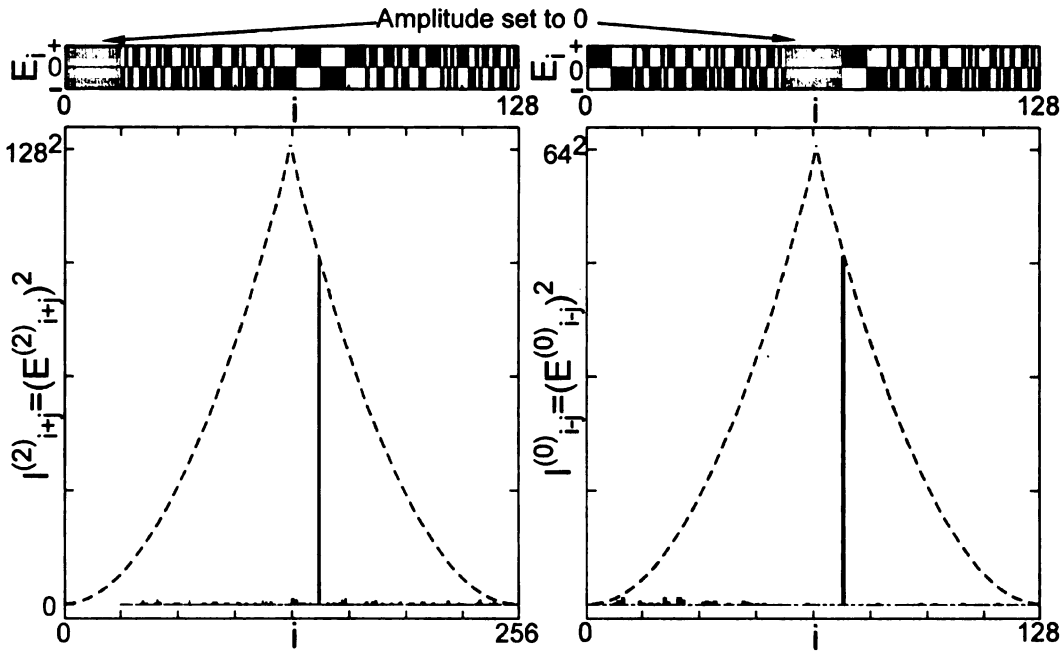

FIG. 5.6. Symmetrized pseudorandom Galois fields (top) and their self-convolution (left) and auto-correlation (right) for the generation of very narrow NLO excitation with minimum background in SHG or SRS spectra. The gray area in top panel shows the spectral part with amplitude set to 0. The dashed line shows the NLO spectra of TL excitation.

When the signal to be maximized is not at the center of the spectrum, we form the *GF* from the longest possible symmetrized sequence. The leftover *GF* bits, which do not contribute to the signal, must be set to 0 by amplitude modulation. This decreases the background without changing the maximum NLO response for 2PE, and suppresses the low frequency half for SRS excitation. Results of calculations according to these rules are presented in Figure 5.6. As the number of bits in the *GF* sequence increases, the amplitude of the signal remains at the TL limit (dashed lines Fig. 5.6.), provided symmetrized sequences are used. At the same time, the average amplitude of the background, as well as the width of the signal peak, decreases linearly with increase in number of pixels. Multiphoton intrapulse interference [73, 74] is responsible for the almost complete background suppression. Thus, without resorting

to empirical evaluation, we are able to construct excellent solutions to the problem of selective NLO excitation. In the case of an ideal pulse shaper, our work is finished at this point.

5.1.5 Experimental results using pseudorandom BP

To demonstrate the analytical solutions given by equations (5.3) and (5.4) under experimental conditions, we performed experiments with sequences of length N=48 bits distributed over the center of the SLM, where the spectral laser power is greater than ¼ of the maximum value; frequencies outside this range were blocked. The spectral width of the remaining portion of the spectrum is 70nm as shown in Fig. 5.7. Initial experiments were performed using symmetrized *GF* based on sequences with minimal autocorrelation [204]. Very narrow peaks in 2PE and SRS spectra were observed. The intensity of the peaks was about 70% of the transform limited intensity. Simulations show that the nonlinearity of spatial to frequency transformation in the pulse shaper decreases the maximum of the peak in the NLO spectrum, and that the SLM spectral resolution is responsible for the less-than-ideal background suppression.

To optimize the experimental CR results we first evaluated all symmetrized 24 bit sequences with a 4 bit flat center region. This gave us a total number of $2^{(48/2)-4}$ sequences to evaluate, a number that is very small compared with the number of 48 bit phase functions with arbitrary phase and amplitude modulation. We simulated the best sequences to predict their NLO response, taking into account the spectrum of the fundamental pulse and the two main imperfections of the SLM, nonlinearity of

frequency dispersion on the SLM and limited spectral resolution. By this method we optimized selective NLO at a number of different frequencies outside the center of the bandwidth so that we could scan the excitation frequency.

Our results are presented in Fig. 5.7, where we scan a narrow-band peak with an S/N of 150 and a CR of 4.5, the highest ever reported in selective NLO excitation by a single phase shaped ultrashort pulse. Compared to a sinusoidal phase modulation, which produces an S/N of 3 and a CR of 0.4, these results show improvement of almost two orders of magnitude. The narrow-band peak has a spectral width of 0.7nm in 2PE and 50 cm^{-1} in SRS spectra, which is close to the spectral width of one SLM pixel, this being an experimental-limiting parameter.

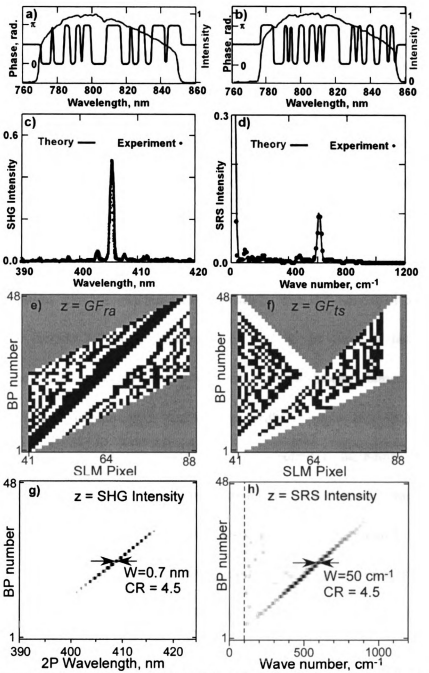

FIG. 5.7. Experimental NLO excitation. (a) and (b) show the spectra of the excitation pulses (gray) and the BP's (black) to achieve the selective SHG and SRS in the center of the spectra, respectively. (c) and (d) show the SHG and SRS spectra corresponding to (a) and (b). The gray lines demonstrate the calculated spectra and the black dots show the experimentally measured spectrum. (e) and (f) show BP masks imprinted on the SLM. Each horizontal row represents different BP shapes, which are shown along the y-axis in the order that the target frequency for selective NLO excitation scans across the spectrum. Black corresponds to 0, white corresponds to π. Gray areas are regions where the amplitude of the field was set to 0. (g) and (h) illustrate experimentally measured SHG and SRS spectra, respectively, as the target frequency scans across the spectrum. Darker shading indicates higher intensity.

5.1.6 Conclusion

In conclusion, we presented a general solution (and a specific 608 bit solution) to selective even-numbered multiphoton excitation. We discovered that using low-autocorrelation binary phase sequences allow us to achieve selective nonlinear optical excitation while suppressing background. The existing literature on low-autocorrelation binary numbers provides sequences that can be used to construct phase functions that will optimize excitation. In this way we avoid using empirical evaluation based searches which scale exponentially with the number of pixels. The applications include TPE spectroscopy, which will be presented in next section. Selective nonlinear excitation will allow coherent anti-Stokes Raman scattering (section 5.3) and photon echo spectroscopy with a single laser pulse. Other applications exist in photochemistry and bio-photonics including functional multiphoton microscopy and selective two-photon photodynamic therapy. The adaptation of number theory principles to physics and chemistry, progress in modern mathematics together with the technical progress in controlling the phase of laser light promises the development of new non-empirical approaches to laser control of physicochemical processes.

5.2 High-resolution two-photon spectroscopy with a non-tunable laser

5.2.1 Introduction

Since the first experimental observation of the SHG[22] and TPE[23] in 1961, several techniques have been developed to determine TPE cross sections for various

materials.[206-208] The direct measurement of the TPA cross sections is rather difficult because only a very small fraction of photons is absorbed in a TPA process. TPEF is an alternative approach to determine the TPE cross section and then calculate the TPA cross section provided that the sample is fluorescent and the quantum efficiency is known.

In 1990, Denk et al. successfully applied two-photon fluorescence into laser scanning microscopy[190]. Because of the fluorescence dependence on the square of the excitation laser intensity, the intrinsic three-dimensional resolution and the absence of background fluorescence, as well as the ability to reduce photobleaching, this two-photon fluorescence microscopy (TPFM) technique soon won over conventional confocal fluorescence microscopy and became the prevalent technique that biologists use to take images for tissues and cells. Since then, a demand of quantitative study in TPE spectra for the widely-used fluorophores arose. Started in 1996, Webb and coworkers published a series of papers[209-212] that measured the TPA and TPE spectra for several common fluorophores. These experiments involved a complicated optical setup and a tunable Ti:Sa laser source. Their laser spectrum can be tuned from 690 to 1050 nm, but this tunability involved 4 sets of different intracativy mirrors. Furthermore, every time when the laser spectrum is tuned, the laser intensity, registration of the beam path and the focusing on the sample might change, making the measurement extremely difficult and time-consuming. Without a laser expert, this kind of measurements is impossible to perform.

To date, more and more new fluorophores have been developed. An easier

method to measure the TPE spectra of the new fluorophores without a laser specialist is required. Furthermore, researchers who are developing new fluorophores also demand an easy way to characterize their new products and compare them with conventional ones. In addition, an easier way to measure TPE spectra would also help spectroscopists who use TPA or TPE spectra to study the electronic structures of excited states of the molecules. Here, we present a fast and automated method of taking TPE spectra.

The concept of this automated TPE spectrometer is to apply the optimized BP's for selective two-photon transitions presented in the previous section to a broadband laser which is capable of causing TPE in a broad spectral range. Thus, the tuning of excitation wavelength is achieved by automated BPS through the pulse shaper instead of by tweaking the laser itself as required for the conventional method. Since the effective two-photon fields generated from BPS do not have the uniform intensities, SHG spectrum corresponding to each BP is required in order to normalize the TPEF obtained from the sample.

5.2.2 Experimental setup

A proof-of-concept experiment was first performed with a normal Ti:Sa oscillator system used in section 5.1. We demonstrate TPE spectrum measurements of several molecules in solution. In Fig. 5.8, we show the TPE spectra for Coumarin 460 and Rhodamine 590 in methanol (10^{-5}M). The spectra obtained by pure phase shaping has very good resolution (~1.5 nm) and are in good agreement with independent

experimental measurements [213].

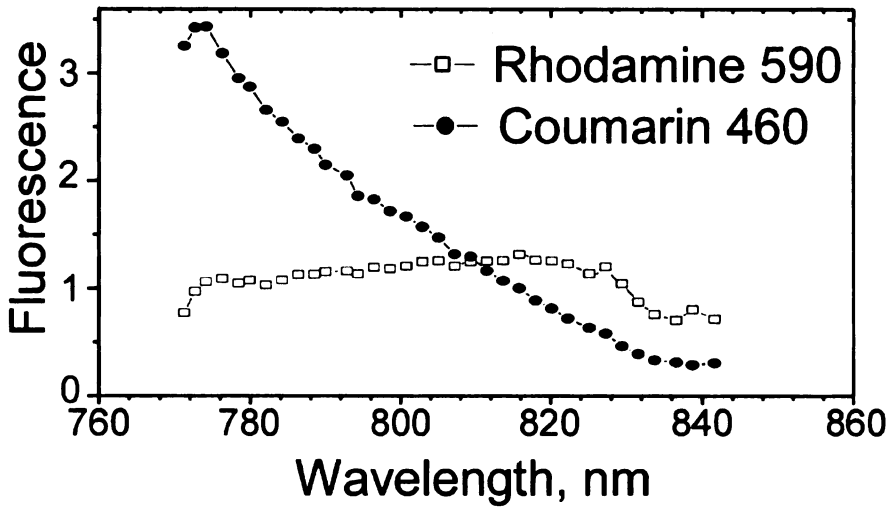

Fig. 5.8. TPE spectra of two fluorescent dyes: rhodamine 590 and coumarin 460

The Venteon oscillator, able to generate sub-5 fs pulses, is ideal for the measurement of TPE spectra. As shown in Chapter 4, such sub-5 fs pulses can generate a SHG spectrum whose span approaches 200 nm (315 - 515nm), covering the two-photon transitions of most biological fluorophores. Fig. 5.9 illustrates the experimental setup. The pulses from the Venteon Ti:Sa oscillator pass through a telescope and then the pulse shaper same as described in section 4.1.1. The pulses are then focused onto the sample, either a 20μm KDP crystal or the 2mm cells containing fluorescent samples. The SHG spectra are obtained with the SHG separation and detection system used in section 4.1.1. The fluorescence signals is collected by a 40x, 0.6 NA objective and then focused on an avalanche photon diode (APD) incorporated with a photon counter. A bandpass filter which allows transmission of 400-600 nm light is also used to minimize the noise from other sources including the scattering of the fundamental pulses.

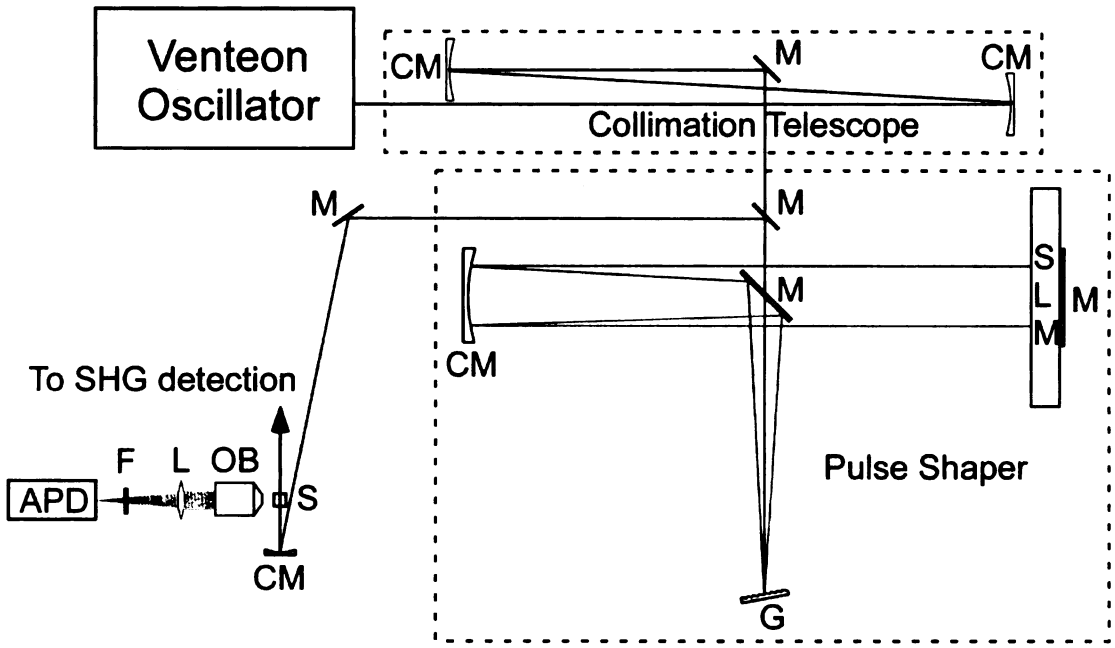

Fig. 5.9. Schematic setup for TPE spectroscopy. Femtosecond pulses from Venteon oscillator are first directed into a 1:2.5 telescope to collimate the beam and expand the beam size to obtain ideal optical resolution in the pulse shaper. The beam is then introduced into a reflective pulse shaper. After the pulse shaper, the beam is focused onto the sample S, which is either a KDP crystal to generate SHG or sample cells to generate the two-photon fluorescence. The SHG signal is directed into the SHG separation and detection system presented in section 4.1.1. The fluorescence signal is collected with a 40x objective OB at 90° angle and focused onto the APD detection unit with lens L. The filter F is used to minimize the unwanted noise including the scattering of the fundamental beams. CM: curved mirror, M: mirror and G: grating.

Both amplitude-only shaping and BPS were used to generate the selective two-photon field from 330 to 480 nm. For amplitude-only shaping, each amplitude window contained 26 SLM pixels, which correspond to a ~20 nm width in the fundamental spectrum. For BPS, a symmetrized 13-bit sequence with minimal autocorrelation was used. Each bit of the BP contains 4 SLM pixels, which in total corresponds to a ~95 nm width in the fundamental spectrum. The resulting SHG spectra, which characterize the effective two-photon field, are shown in Fig. 5.10. Both pure amplitude shaping and BPS achieved selective SHG. However, BPS provides sharper peaks that would result in better resolution in TPE spectrum. By

using a BP with more bits, the resolution could be reduced to ~0.7nm, which corresponds to the optical resolution of a single SLM pixel.

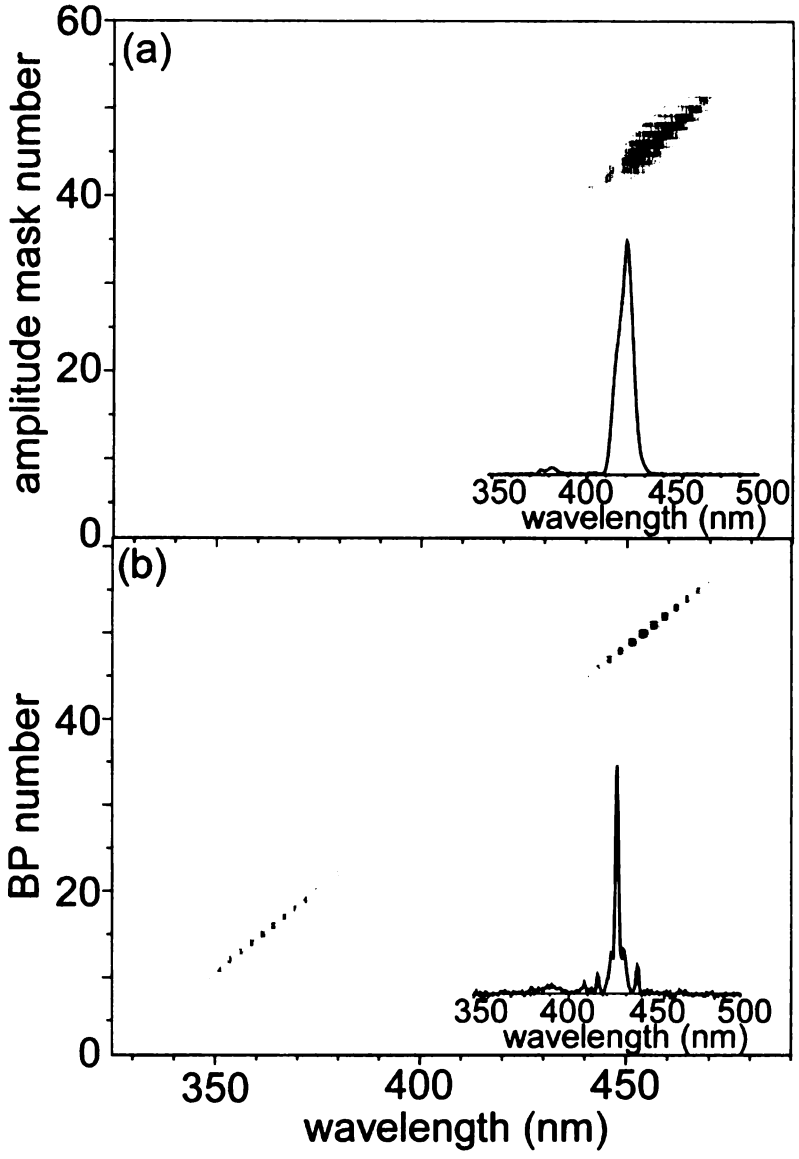

Fig. 5.10. SHG spectra generated with (a) pure amplitude modulation and (b) BPS for selective TPE. Each horizontal line in the contour plot represents a SHG spectrum, which are shown along the y-axis in the order of increasing target frequency for selective TPE. Both approaches provide the TPE effective fields that scan from 330 to 480 nm. Pure amplitude modulation has slightly better CR given the signal window is bigger than that for BPS. The BPS gives much sharper TPE field, which is necessary to achieve high resolution in TPE spectroscopy.

After the SHG spectra were acquired, the fluorescent samples were placed at the target position and the TPEF signal was recorded with the same set of amplitude or

BP functions. Each amplitude or BP function corresponds to a certain excitation wavelength as shown in Fig. 5.10. The TPEF intensity for each amplitude or BP is normalized with the corresponding total SHG intensity in order to acquire the TPE spectrum. It takes less then a minute to acquire a TPE spectrum for most of the samples once the effective TPE field is characterized by SHG, which take an additional minute. The spectrum acquisition time is much shorter compared with the conventional method.

5.2.3. Accuracy and reproducibility

In order to test the accuracy of the proposed method, we took the TPE spectra of two well-known molecules: Fluorescein and Rhodamine B. Fig. 5.11 shows the comparison between our spectra and the spectra measured by the Webb group with the conventional method[209, 210]. The excellent agreement demonstrates the accuracy of this new approach. In addition, the new method provides better resolution, ~4 nm compared with 10 ~ 20 nm resolution in the conventional method.

Figure 5.12 illustrates TPE spectra that measured on different days for three different samples The samples used were Fluorescein and 8-hydroxypyrene-1,3,6-trisulfonic acid (HPTS), a pH-sensitive molecule that has a different absorption spectra when the pH value of the environment changes. The excellent reproducibility demonstrated in those spectra makes this fast and automated approach very reliable.

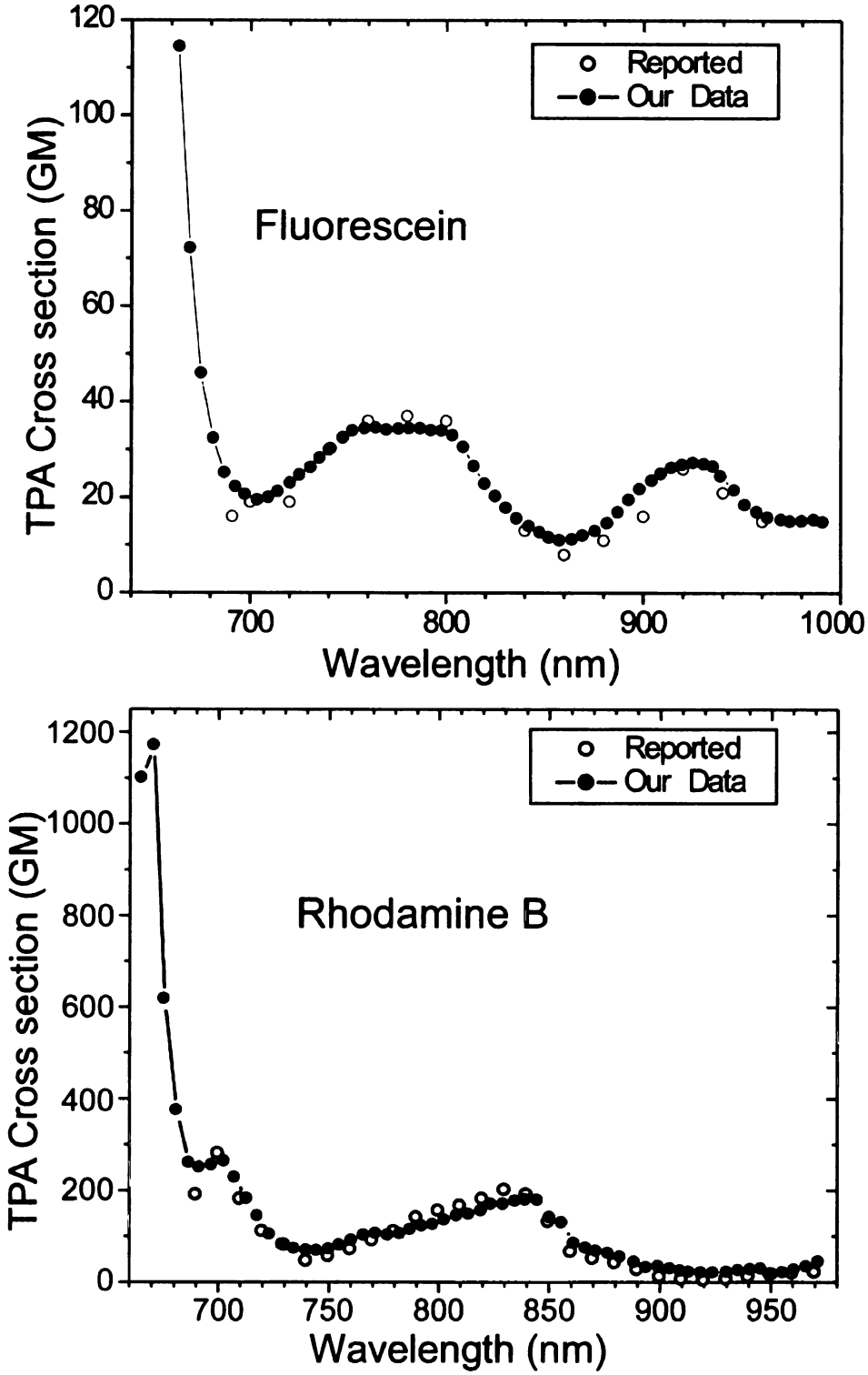

Fig 5.11. Comparison between the TPE spectra measured with our approach and reported data for (a) Fluorescein and (b) Rhodamine B. The solid lines with black dots in both panels illustrate the TPE spectra taken with our approach, and the circles shows the spectra taken with the conventional method. Note the excellent agreement between both.

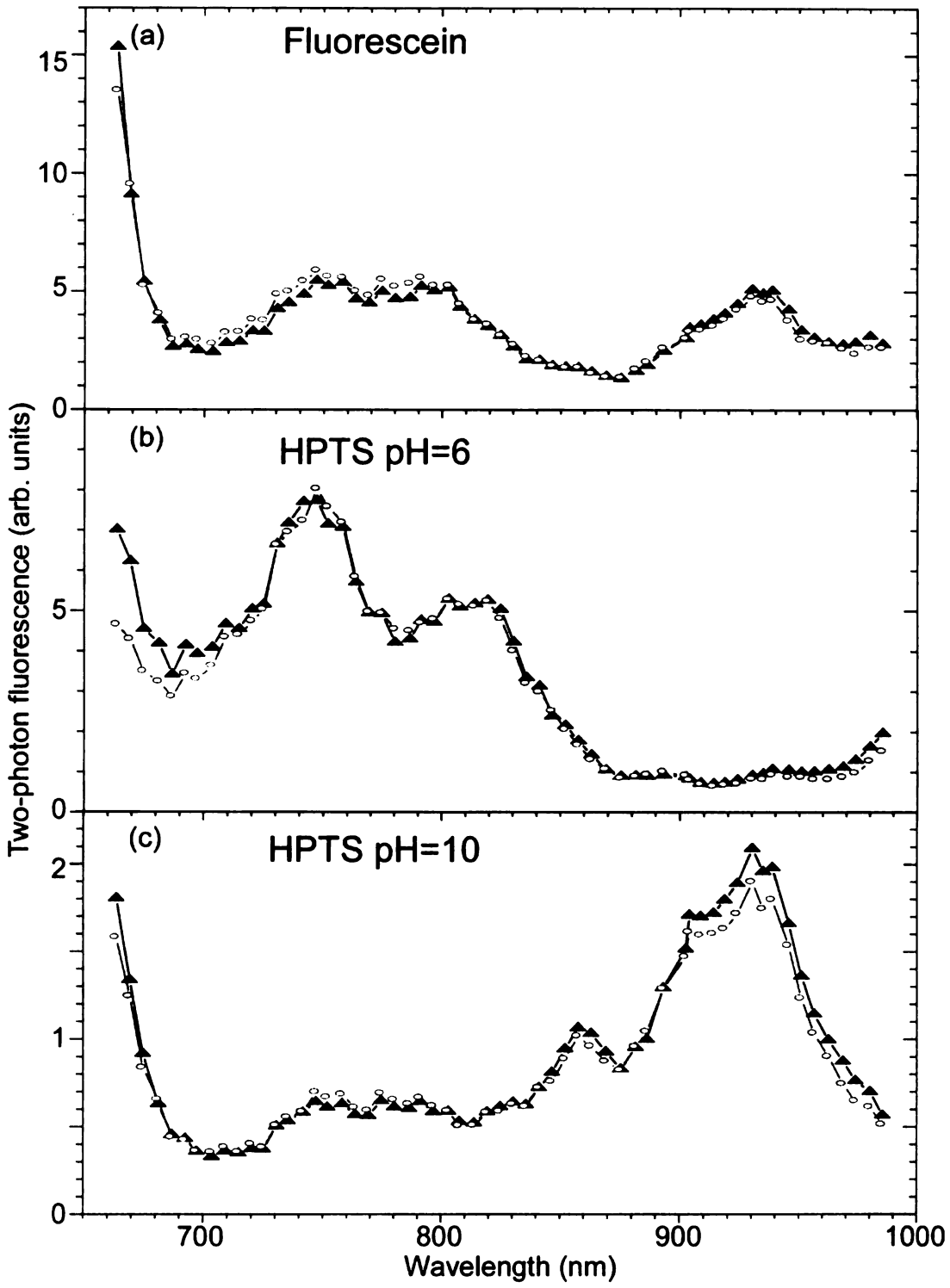

Fig 5.12. TPE spectra for (a) Fluorescein, (b)HPTS in a pH = 6 solution and (c) HPTS in a pH =10 solution measured on two different days. Note the excellent agreement between two sets of data.

5.3 CARS spectroscopy for remote detection and identification of chemicals

5.3.1 Introduction

Present analytical methods for compound identification are incapable of addressing the need for detecting improvised explosive devices. Therefore, an urgent need exists to develop methods capable of standoff explosive detection, such that security decisions can be made while the explosive is outside the range of severe damage. Several spectroscopic techniques have been explored for standoff detection, most of them relying on the high intensity and directionality of lasers. Laser-induced breakdown spectroscopy (LIBS)[214, 215] and spontaneous Raman spectroscopy[216, 217] are presently among the most promising. However, both of these approaches are unsafe, causing some target destruction because of their dependence on powerful laser beams with pulse energies ranging from tens to hundreds of milli-Joules.

The National Research Council report on "Existing and Potential Standoff Explosive Detection Techniques"[218] lists CARS as one of the promising techniques for standoff explosive detection. CARS is a third order nonlinear process which typically involves the interaction of the material with three laser beams (pump, Stokes, and probe).[219] Unlike LIBS, which only provides relative atomic composition by ablating the sample, CARS obtains spectroscopic vibrational information that can be used to distinguish among different molecules and even isomers. The coherent stimulation of the Raman process in CARS results in several orders of magnitude greater efficiency over spontaneous Raman signals.[220] Therefore the process requires orders of magnitude less power, making it much safer than LIBS and spontaneous

Raman. In this sense, CARS provides a non-destructive approach.

In 2002, Scully and coworkers proposed CARS for chemical warfare detection,[221] and recently, reported the first femtosecond adaptive spectroscopic technique (FAST) CARS spectrum of anthrax markers obtained at an arms-length distance of 0.2 m.[222] A significant achievement that greatly advances the possibility of biological warfare agent identification in real time, but requires three different femtosecond laser pulses with different wavelengths, specific time delays and at a specific crossed-beam geometry. The resulting FAST CARS signal depends on these stringent alignment and timing requirements, making this method impractical for standoff 100 m detection, particularly outside of a laboratory.

CARS has become a promising tool for microscopic material and biological imaging , utilizing the vibrational response of different molecules as a contrast agent, and thereby eliminating the need for fluorescent labeling.[223] Recently, a single-beam CARS approach for microscopy was developed by Silberberg.[194] Single-beam CARS removes the complexities involved when using several laser pulses, eliminating the spatial and temporal overlapping problems. This approach has been further refined by the groups of Leone[224] and Motzkus.[225]

Single-beam CARS microscopy uses pico-Joule pulses with a broad bandwidth spectra (>100 nm) which are prone to chromatic dispersion in air. The signal is usually drowned by the non-resonant (non-specific) nonlinear optical molecular response. Special spectral phase and polarization pulse shaping is required to enhance the desired spectroscopic information, typically requiring additional background

subtraction. Adaptation of this method to standoff detection, therefore, requires amplified (six-orders of magnitude) ultra-broad bandwidth pulses with phase and polarization pulse shaping capable of delivering optimally coherent pulses at distances of 100 m, so that the non-resonant background can be eliminated. Ideally, this method should also be capable of selective vibrational state excitation to provide orthogonality and eliminate false alarms.

Here in this section, we present molecular identification from a standoff distance of 12 m (currently limited by laboratory space), based on an improved strategy of single-beam CARS and describe the key technical breakthroughs that make this approach possible. Then, data from a number of compounds in liquid states are shown, including isomeric compounds, demonstrating the ability of this method for remote chemical identification. Finally, the feasibility of selective excitation among different intramolecular vibrational modes and complete non-resonant CARS background suppression based on optimally designed laser pulses with GF is demonstrated.

5.3.2 Experimental setup

As shown in Fig. 5.13, the intensive (200 μJ) broadband laser pulses from the hollow waveguide (see section 2.1.4) are first collimated by a 0.762-m-focal-length spherical mirror and then directed into a pulse shaper with a 640-pixel dual-mask SLM. After the pulse shaper, the beam is focused by a home-built newtonian telescope onto the target 12 m away form the telescope. The telescope consists of a negative lens (focal length equals 0.2 m) and a 0.762-m-focal-length spherical mirror

with 76.2 mm diameter. The beam diameter at the telescope was 50 mm. The laser beam energy at the sample was less than 10 μJ/pulse with a beam diameter of 2 mm. This laser power, orders of magnitude less than that is required by LIBS and spontaneous Raman, is well below the damage threshold of all the samples, no detectable damage or continuum light generation was observed during the CARS measurements. The distance in this experiment is limited by the size of the optical table instead of the method itself. The experimental results were obtained with a mirror behind the sample that reflects the CARS signal back. However, data obtained from back-scattered signal has also been demonstrated and published elsewhere.[179] A beam splitter is used to direct the signal to the detection system. The detection system comprises a 740 nm lowpass filter (Omega Optical), a thin horizontal polarizer, a 5-cm focal-length thin lens and a QE65000 spectrometer (Ocean Optics).

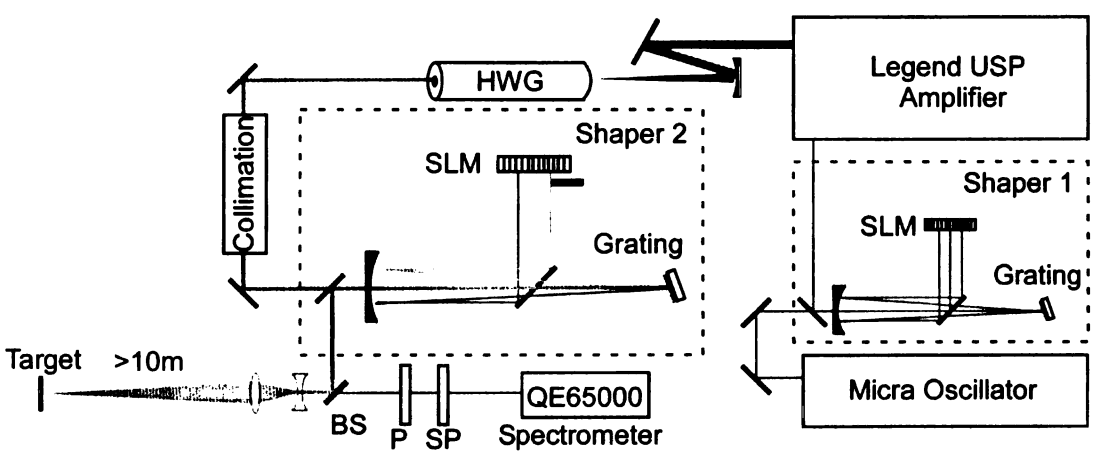

Fig. 5.13. CARS spectroscopy optical setup for remote chemical detection. HWG: hollow waveguide, BS: beamsplitter, P: polarizer and SP: shortpass filter.

MIIPS was used through the 640-pixel pulse shaper to eliminate the spectral phase distortion introduced by the hollow core fiber, optics including the wall of cell containing the sample and especially, the air. The air has a GVD value of 20.1 fs^2/m[226]

and with a 12-m distance, the air can make our initial 10 fs pulses about seven times longer, resulting a drop of the signal intensity ~50 times. Pulse shaping was also used to control the phase and polarization of different components of the laser pulses in a way that minimizes the non-resonant contribution and improves resolution. The non-resonant CARS signal increases with the bandwidth of the laser, which in our case is 1800 cm^{-1}. In order to reduce the considerable background in single-beam CARS microscopy Oron et al. use a π phase gate.[227] In other work, they have also introduced a polarization gate to the probe to further improve the resolution.[195] We incorporate both of these strategies in our approach. The probe pulse is defined by keeping 6 out of 640 pixels (about 1.5 nm bandwidth, centered at 770 nm) horizontally polarized while using the remaining pixel to rotate the rest of the pulse to vertical polarization. A phase gate (3 out of 640 pixels) is also used. (See Fig. 5.14)

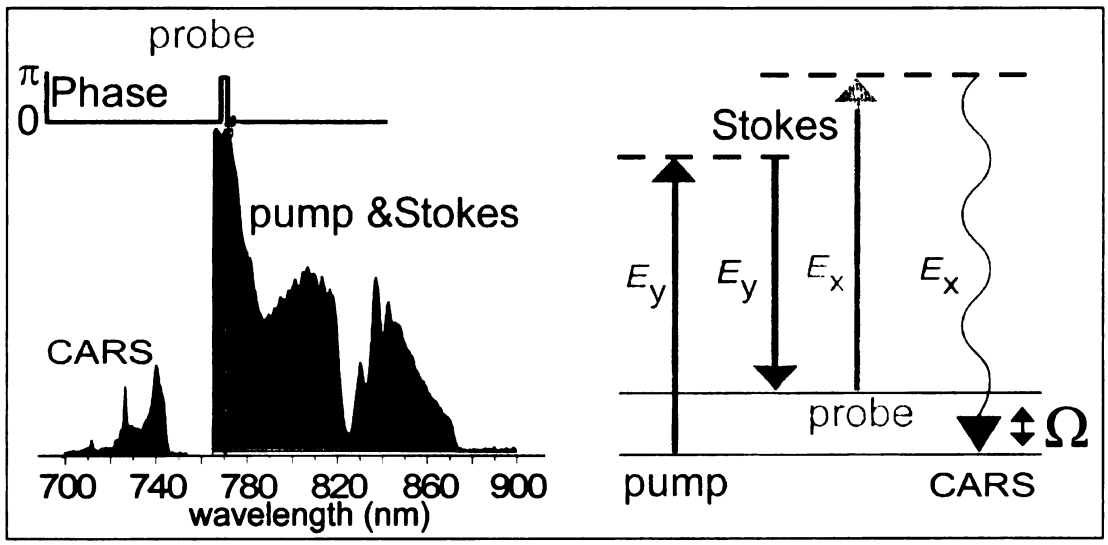

Fig. 5.14. The spectrum, phase and polarization of the shaped laser pulse for single-beam CARS. Pump, stokes, probe and CARS signals are marked with different gray scales in left panel. Pump and stokes have vertical polarization (y) while the probe and CARS signal have horizontal polarization (x). The right panel shows a ladder diagram for the CARS process.

MIIPS makes sure that TL pulses are used at the target so that all the pump and

stokes pairs are in phase and interfere constructively. As shown in Fig. 5.15, the signal intensity changes more than an order of magnitude with and without MIIPS correction of the spectral phase distortion.

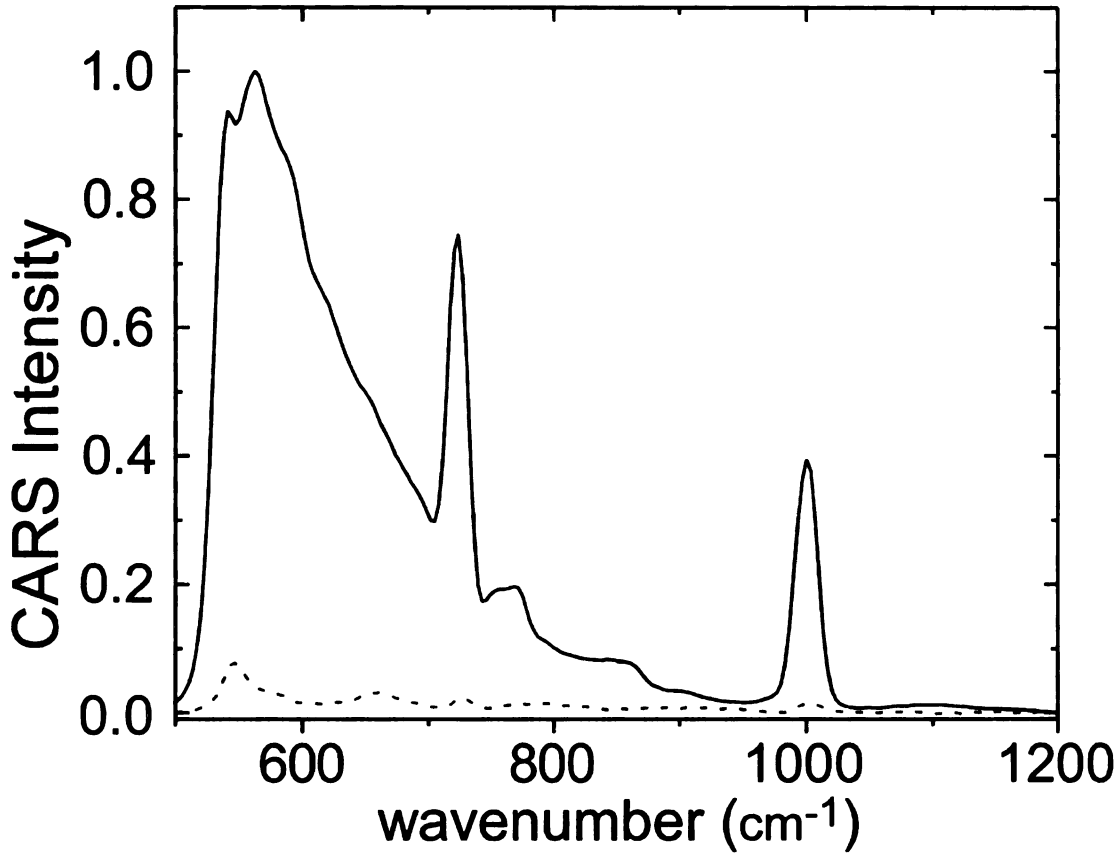

Fig. 5.15. Single-beam CARS spectrum (raw data). Unprocessed spectra of *m*-xylene collected at a standoff 12 m distance with (solid) and without (dashed) phase distortion compensation using MIIPS. Note that both resonant and non-resonant contribution increase with MIIPS compensation.

The unprocessed CARS spectra presented in Fig. 5.15 comprise both resonant and non-resonant contributions, where resonant contribution present as sharp peaks corresponding to different vibration modes of the molecules while the non-resonant contribution is present as broad features under sharp peaks that give no chemical information. Therefore, we fit the broad-bandwidth non-resonant contribution and then subtract it to obtain the processed spectra only with resonant peaks that give

chemical identification signature. The spectra shown in the following section 5.3.3 are all processed spectra with above procedures.

5.3.3 Remote chemical identification with CARS spectroscopy

In this section, chemical identification at a remote distance (12 m) is demonstrated with single-beam CARS spectroscopy. Fig. 5.16 shows the remote CARS spectra from several pure liquid samples. The liquid samples used were toluene (J.T. Baker), *o*-xylene (Fluka), *o*-nitrotoluene, *m*-nitrotoluene, *p*-xylene, and *m*-xylene(Sigma-Aldrich). All samples had purity greater than 98% and were used without further purification. Cells with 1mm path length were used as container for the liquid samples for the measurements.

In Fig 5.16, the characteristic vibration fingerprints of each molecule are clearly shown, enabling us to easily distinguish all samples including different isomeric species. This is the major advantage for CARS spectroscopy over LIBS, which is not capable of identifying molecular isomers. Based on those vibration fingerprints, an automated computer software was demonstrated and a screenshot of the computer interface is shown in Fig. 5.17. Incorporated with the remote CARS optical setup, this software can automatically identify those six liquid samples 12-meter away in a second. When the sample is not one of those six chemicals in the reference library, the indicator for unknown sample will light up.

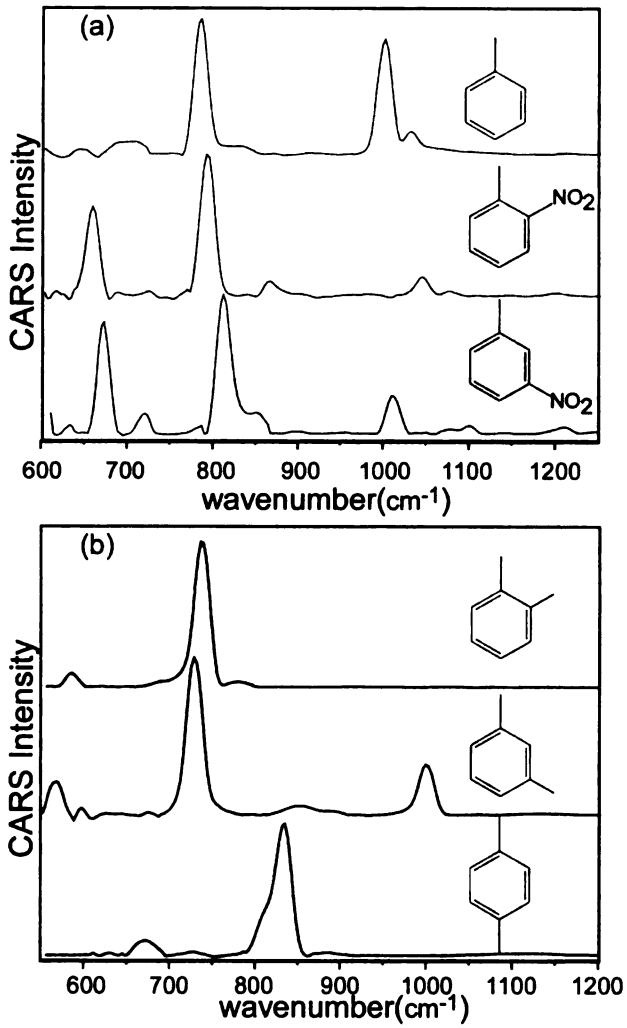

Fig. 5.16. Remote CARS spectra from liquid samples. A) CARS spectra from liquid toluene, o-nitrotoluene and m-nitrotoluene; B) CARS spectra from liquid ortho, meta and para-xylene. Note the vibrational signatures of the molecules shown in the spectra give a very easy way to distinguish isomers.

This remote single-beam CARS spectroscopy can identify chemical in liquid, solid and gaseous state, no matter the sample is pure or in mixtures. CARS spectrum from a 1:99 mixtures of *o*-xylene and *p*-xylene has been demonstrated, presenting ability of this approach to quantitatively analyze mixtures down to the microgram level. The single laser shot capability of this method and detection of back-scattered signals instead of retro-reflected signals have also been shown. Details of these

studies are published elsewhere.[179] The software can also be expanded to identify more chemicals simply by adding the vibration fingerprints of new chemicals into the reference library.

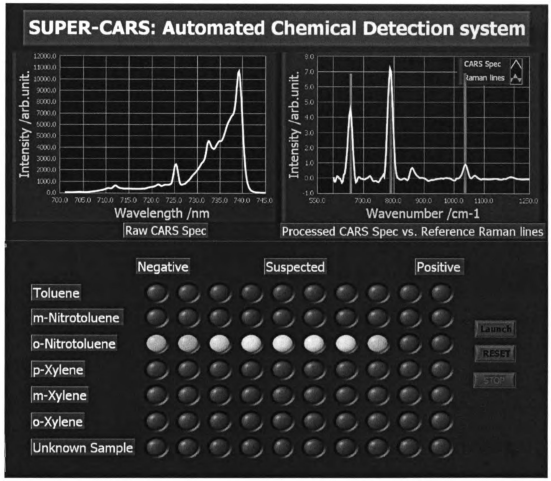

Fig. 5.17. Screenshot of the automated chemical identification software. The upper-left panel shows the unprocessed data and the upper-right panel shows the processed CARS spectrum (white) and the matched the vibration fingerprints peaks (gray). The lower part of the interface shows the identification indicators for each chemicals and the start and stop button of the program. The current indicator shows that *o*-nitrotoluene is detected for the last eight shots.

5.3.4 Mode-selective CARS spectroscopy with BPS

The most important requirement for standoff identification is the ability to discriminate signals from other sources as well as signals from a complex chemical background. In particular, for CARS it is important to eliminate, as much as possible,

contributions from the non-resonant background. The unprocessed CARS spectrum of *m*-xylene is presented in Fig. 5.15. Note that the non-resonant background (broad feature spanning the whole spectrum) is more intense than the resonant CARS features at 725 and 1000 cm^{-1}.

Silberberg and coworkers used a sinusoidal phase function to control the single broad bandwidth CARS process and achieved some molecular selectivity[194]. Optimum selectivity, with maximum background suppression, can be achieved using binary phase functions[75]. When using binary phases, the laser pulse spectrum is partitioned into discrete regions, each receiving a phase retardation value of zero or π. The CARS signal at each frequency Ω is given by the sum of discrete contributions from all the frequencies in the pulse whose difference is Ω according to the equation: $E(\Omega) = \sum_{\omega} E(\omega)E(\omega - \Omega)$, where the electric field E can only take the value of (+1) when the phase is zero and (−1) when the phase is π. The goal becomes finding the binary phase function that causes the sum to reach a maximum for the desired Ω, and zero elsewhere. Fortunately, this problem has been solved in the field of mathematics. The type of functions that we are looking for are known as GF, or minimum correlation sequences, as presented in previous section.

Here, we use optimal discrimination based on GF synthesized using binary phase functions to achieve selective excitation of individual vibrational modes, and at the same time eliminate the non-resonant background. One of the reasons why the non-resonant signal is greatly reduced is that the complex binary spectral phase causes the creation of a train of pulses in the time domain (see Fig. 5.18(b)). The temporal

profiles of the pulses corresponding to red and blue binary phases show oscillation periods ~46 fs and ~33 fs, which match the vibration frequency of ν_1 breathing and ν_{12} in-plane bending modes of *m*-xylene, respectively.

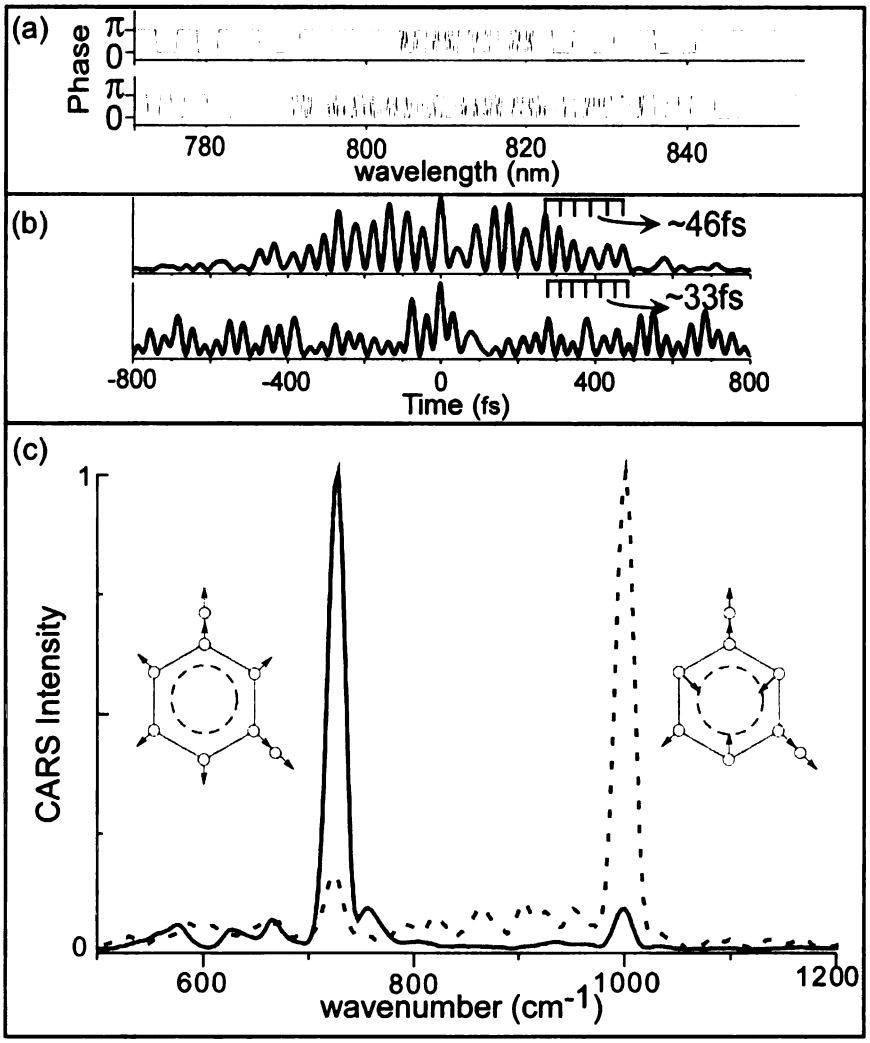

Fig. 5.18. Selective excitation of individual vibrational modes for *m*-xylene. (a) BP's that optimize different individual vibrations of *m*-xylene. The top phase is designed to optimize excitation of the breathing mode at 725 wavenumber and the lower phase is designed to optimize excitation of in-plane bending mode at 1000 wavenumber. (b) The calculated temporal profiles corresponding to top and lower phases in panel (a). Note that the oscillation periods of those temporal profiles are ~46 fs and ~33 fs, which match the vibration frequency of the breathing and in-plane bending modes of *m*-xylene, respectively. (c) Unprocessed CARS spectra from *m*-xylene with two specially designed binary phases. Note that the non-resonant contribution is successfully suppressed eliminating the need for data processing. The designed binary phases control the ratio between the two Raman peaks with an overall two order-of-magnitude discrimination from 7:1 to 1:12. D. Integrated intensity for different binary phases (optimized for different Raman shifts) applied in the pulse shaper.

By spreading the peak intensity of the ultrashort pulse into several sub-pulses, the non-resonant contribution is essentially eliminated. This type of pulse shaping allows for CARS data to be collected with high selectivity despite the ultrabroad bandwidth. The unprocessed spectra in Fig. 5.18(c) show selective excitation of the ν_1 or ν_{12} modes of *m*-xylene, with the elimination of non-resonant contribution. Frequency selective excitation, as shown here, gives single-beam CARS a means to discriminate between different compounds in a complex mixture, making it ideal for applications in complex environments. By collecting the integrated CARS signal for each binary phase, single-beam CARS spectroscopy can be achieved without a spectrometer.

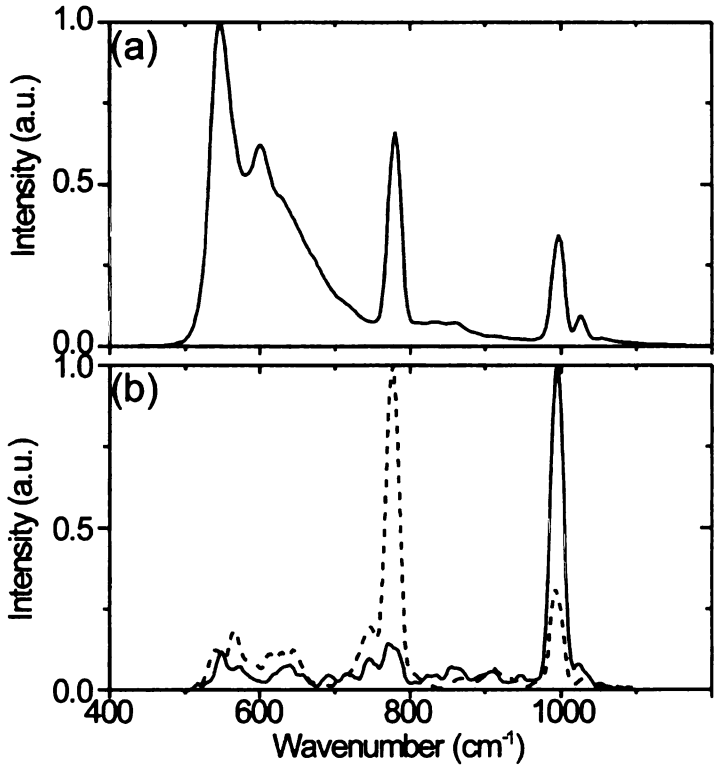

Fig. 5.19. Selective excitation of individual vibrational modes for toluene. (a) Unprocessed single-beam CARS spectrum of toluene. A large non-resonant background is present. (b) Unprocessed single-beam CARS spectra of toluene using specially designed pulses. For each spectrum, a binary phase designed to optimize individual excitation of vibrational modes was used. Selectivity and suppression of the non-resonant background were obtained. The spectra were taken ~12 m away from the sample.

Selective excitation of individual vibrational modes and elimination of the non-resonant contribution are also demonstrated for other chemicals. Fig. 5.19 shows the results for toluene.

5.4 Conclusions

In this chapter, selective multiphoton excitations are achieved with a single broadband laser source through pulse shaping. The optimized BP functions allow us to achieve selective NLO excitation for a certain frequency while suppressing the background elsewhere. This approach let us avoid using empirical evaluation based on searches that scale exponentially with the number of pixels.

The optimized BP functions were applied to a quasi-octave laser source to demonstrate a fast and robust way to measure the TPE spectra with high resolution. The same BP's can be applied in TPFM, so that the fluorophores that have same or similar emission but different absorption spectra, e.g. HPTS in environments with different pH values, can be excited selectively and identified. Another possible direct application of the same BP's is two-photon photodynamic therapy. The laser pulses can only activate the medicine associated with a certain part of tissue or cellular components without changing others. This is extremely usefully for kill a certain unhealthy tissue or cell, leaving health cells untouched.

Single-beam CARS spectroscopy for remote chemical identification is also presented in this chapter. Although single-beam CARS was achieved for microscopy several years ago by satisfying the phase matching condition through very tight focus

by microscope objectives, this is the first demonstration of single-beam CARS with a loose focus for remote detection. This spectroscopy technique possesses the sensitivity, background discrimination and detection speed required for standoff identification of compounds and mixtures in solid, liquid and gaseous phase. GF optimized BP's were also applied in this technique to achieve selective vibrational mode excitation with complete elimination of non-resonant background contributions, making them very promising for single-beam CARS microscopy applications, too.

Conclusion

This dissertation focuses on developing the shaped femtosecond laser an all-purpose tool that can be used by non-experts. There are two main aspects in this research. The first aspect explored was the ability to control excitation essentially of any molecular transitions using a single laser source, taking advantage of phase control of multiphoton processes, and the second is the ability to selectively excite a molecular transition at a certain frequency but not others.

A universal laser source that could be used to excite any possible molecular transition eliminates the complexity to use multiple laser sources or a tunable laser source. In both latter cases, an expert in laser and optics is required for jobs such as tweaking the laser or realign the beam path every time that experiment condition changes, making automated usage of the laser more implausible. Beyond the use of such a universal source for research, applications of this source would take advantage of its great flexibility. The control of several quasi-octave laser sources, whose spectra cover most of the molecular transitions by different multiphoton processes, has been achieved in this work by measuring and correcting the spectral phase distortion through MIIPS. These progresses establish a firm foundation on which the universal laser source will be constructed, I believe in the very near future.

Selective transitions for SHG, TPEF, SRS and CARS processes are demonstrated through BPS in this work. We discovered an approach with which one can excite a certain multiphoton transition while suppressing excitation of all other transitions.

Besides their applications in nonlinear spectroscopy and molecular identification as demonstrated in this dissertation, these results would inspire the progress in a variety of field such as biological imaging, photodynamic therapy, nanoscale lithology and information and telecommunication technology.

Bibliography

1 A. H. Zewail, *Physics Today* **33**, (11), 27-33 (1980).

2 W. S. Warren, and A. H. Zewail, *Journal of Chemical Physics* **75**, (12), 5956-5958 (1981).

3 W. S. Warren, and A. H. Zewail, *Journal of Chemical Physics* **78**, (5), 2279-2297 (1983).

4 W. S. Warren, and A. H. Zewail, *Journal of Chemical Physics* **78**, (5), 2298-2311 (1983).

5 W. S. Warren, and A. H. Zewail, *Journal of Chemical Physics* **78**, (6), 3583-3592 (1983).

6 C. P. Lin, J. Bates, J. T. Mayer, and W. S. Warren, *Journal of Chemical Physics* **86**, (6), 3750-3751 (1987).

7 W. S. Warren, *Science* **242**, (4880), 878-884 (1988).

8 D. E. Spence, P. N. Kean, and W. Sibbett, in *Conference on Laser and electro-optics (CLEO) CPDP10*, OSA/IEEE LEOS, Anaheim, California, 1990.

9 D. E. Spence, P. N. Kean, and W. Sibbett, *Optics Letters* **16**, (1), 42-44 (1991).

10 A. D. Bandrauk, Y. Fujimura, and R. J. Gordon, *Laser Control and Manipulation of Molecules*. American Chemical Society: Washington, 2002; Vol. 821, p 371.

11 N. E. Henriksen, *Chemical Society Reviews* **31**, (1), 37-42 (2002).

12 T. C. Weinacht, and P. H. Bucksbaum, *Journal of Optics B-Quantum and Semiclassical Optics* **4**, (3), R35-R52 (2002).

13 G. Roberts, *Philosophical Transactions of the Royal Society of London Series a-Mathematical Physical and Engineering Sciences* **360**, (1794), 987-1021 (2002).

14 S. A. Rice, and S. P. Shah, *Physical Chemistry Chemical Physics* **4**, (10), 1683-1700 (2002).

15 T. Brixner, and G. Gerber, *Chemphyschem* **4**, (5), 418-438 (2003).

16 D. Goswami, *Physics Reports-Review Section of Physics Letters* **374**, (6), 385-481 (2003).

17 H. Rabitz, *Science* **299**, (5606), 525 (2003).

18 M. Shapiro, and P. Brumer, 354 (2003).

19 M. Dantus, and V. V. Lozovoy, *Chemical Reviews* **104**, (4), 1813-1859 (2004).

20 V. V. Lozovoy, and M. Dantus, *Chemphyschem* **6**, (10), 1970-2000 (2005).

21 V. V. Lozovoy, and M. Dantus, *Annu. Rep. Prog. Chem., Sect. C: Phys. Chem.* **102**, 227-258 (2006).

22 P. A. Franken, G. Weinreich, C. W. Peters, and A. E. Hill, *Physical Review Letters* 7, (4), 118-& (1961).

23 W. Kaiser, and C. G. B. Garrett, *Physical Review Letters* 7, (6), 229-& (1961).

24 T. H. Maiman, *Nature* **187**, (4736), 493-494 (1960).

25 M. Goppert-Mayer, *Annalen Der Physik* **9**, (3), 273-294 (1931).

26 W. S. Warren, *Journal of Chemical Physics* **81**, (12), 5437-5448 (1984).

27 A. M. Weiner, D. E. Leaird, G. P. Wiederrecht, and K. A. Nelson, *Science* **247**, (4948), 1317-1319 (1990).

28 A. M. Weiner, D. E. Leaird, G. P. Wiederrecht, and K. A. Nelson, *Journal of the Optical Society of America B-Optical Physics* **8**, (6), 1264-1275 (1991).

29 B. Broers, L. D. Noordam, and H. B. V. Vandenheuvell, *Physical Review A* **46**, (5), 2749-2756 (1992).

30 B. Broers, L. D. Noordam, and H. B. V. Vandenheuvell, *Institute of Physics Conference Series*, (126), 223-226 (1992).

31 B. Broers, H. B. V. Vandenheuvell, and L. D. Noordam, *Optics Communications* **91**, (1-2), 57-61 (1992).

32 D. J. Tannor, and S. A. Rice, *Journal of Chemical Physics* **83**, (10), 5013-5018 (1985).

33 D. J. Tannor, R. Kosloff, and S. A. Rice, *Journal of Chemical Physics* **85**, (10),

5805-5820 (1986).

34 R. S. Judson, and H. Rabitz, *Physical Review Letters* **68**, (10), 1500-1503 (1992).

35 C. J. Bardeen, V. V. Yakovlev, K. R. Wilson, S. D. Carpenter, P. M. Weber, and W. S. Warren, *Chemical Physics Letters* **280**, (1-2), 151-158 (1997).

36 D. Yelin, D. Meshulach, and Y. Silberberg, *Optics Letters* **22**, (23), 1793-1795 (1997).

37 T. Baumert, T. Brixner, V. Seyfried, M. Strehle, and G. Gerber, *Applied Physics B-Lasers and Optics* **65**, (6), 779-782 (1997).

38 A. Efimov, and D. H. Reitze, *Optics Letters* **23**, (20), 1612-1614 (1998).

39 K. Takasago, M. Takekawa, M. Suzuki, K. Komori, and F. Kannari, *Ieee Journal of Selected Topics in Quantum Electronics* **4**, (2), 346-352 (1998).

40 E. Zeek, K. Maginnis, S. Backus, U. Russek, M. Murnane, G. Mourou, H. Kapteyn, and G. Vdovin, *Optics Letters* **24**, (7), 493-495 (1999).

41 D. Zeidler, T. Hornung, D. Proch, and M. Motzkus, *Applied Physics B-Lasers and Optics* **70**, S125-S131 (2000).

42 M. R. Armstrong, P. Plachta, E. A. Ponomarev, and R. J. D. Miller, *Optics Letters* **26**, (15), 1152-1154 (2001).

43 A. Baltuska, T. Fuji, and T. Kobayashi, *Optics Letters* **27**, (5), 306-308 (2002).

44 F. L. Legare, J. M. Fraser, D. M. Villeneuve, and P. B. Corkum, *Applied Physics B-Lasers and Optics* **74**, S279-S282 (2002).

45 P. Baum, S. Lochbrunner, L. Gallmann, G. Steinmeyer, U. Keller, and E. Riedle, *Applied Physics B-Lasers and Optics* **74**, S219-S224 (2002).

46 A. Assion, T. Baumert, M. Bergt, T. Brixner, B. Kiefer, V. Seyfried, M. Strehle, and G. Gerber, *Science* **282**, (5390), 919-922 (1998).

47 M. Bergt, T. Brixner, B. Kiefer, M. Strehle, and G. Gerber, *Journal of Physical Chemistry A* **103**, (49), 10381-10387 (1999).

48 A. Glass, T. Rozgonyi, T. Feurer, R. Sauerbrey, and G. Szabo, *Applied Physics B-Lasers and Optics* **71**, (3), 267-276 (2000).

49 C. Daniel, J. Full, L. Gonzalez, C. Kaposta, M. Krenz, C. Lupulescu, J. Manz, S. Minemoto, M. Oppel, P. Rosendo-Francisco, S. Vajda, and L. Woste, *Chemical Physics* **267**, (1-3), 247-260 (2001).

50 T. Brixner, B. Kiefer, and G. Gerber, *Chemical Physics* **267**, (1-3), 241-246 (2001).

51 R. J. Levis, G. M. Menkir, and H. Rabitz, *Science* **292**, (5517), 709-713 (2001).

52 R. J. Levis, and H. A. Rabitz, *Journal of Physical Chemistry A* **106**, (27), 6427-6444 (2002).

53 T. Hornung, R. Meier, D. Zeidler, K. L. Kompa, D. Proch, and M. Motzkus, *Applied Physics B-Lasers and Optics* **71**, (3), 277-284 (2000).

54 D. Zeidler, S. Frey, K. L. Kompa, and M. Motzkus, *Physical Review A* **64**, (2), art. no.-023420 (2001).

55 T. Ando, T. Urakami, H. Itoh, and Y. Tsuchiya, *Applied Physics Letters* **80**, (22), 4265-4267 (2002).

56 T. Brixner, N. H. Damrauer, P. Niklaus, and G. Gerber, *Nature* **414**, (6859), 57-60 (2001).

57 T. Brixner, N. H. Damrauer, B. Kiefer, and G. Gerber, *Journal of Chemical Physics* **118**, (8), 3692-3701 (2003).

58 T. C. Weinacht, J. L. White, and P. H. Bucksbaum, *Journal of Physical Chemistry A* **103**, (49), 10166-10168 (1999).

59 T. Hornung, R. Meier, and M. Motzkus, *Chemical Physics Letters* **326**, (5-6), 445-453 (2000).

60 T. C. Weinacht, R. Bartels, S. Backus, P. H. Bucksbaum, B. Pearson, J. M. Geremia, H. Rabitz, H. C. Kapteyn, and M. M. Murnane, *Chemical Physics Letters* **344**, (3-4), 333-338 (2001).

61 R. A. Bartels, T. C. Weinacht, S. R. Leone, H. C. Kapteyn, and M. M. Murnane, *Physical Review Letters* **88**, (3), art. no. 033001 (2002).

62 D. Zeidler, S. Frey, W. Wohlleben, M. Motzkus, F. Busch, T. Chen, W. Kiefer, and A. Materny, *Journal of Chemical Physics* **116**, (12), 5231-5235 (2002).

63 J. L. Herek, W. Wohlleben, R. J. Cogdell, D. Zeidler, and M. Motzkus, *Nature*

417, (6888), 533-535 (2002).

64 T. Hornung, R. Meier, R. de Vivie-Riedle, and M. Motzkus, *Chemical Physics* **267**, (1-3), 261-276 (2001).

65 R. Bartels, S. Backus, E. Zeek, L. Misoguti, G. Vdovin, I. P. Christov, M. M. Murnane, and H. C. Kapteyn, *Nature* **406**, (6792), 164-166 (2000).

66 S. Vajda, A. Bartelt, E. C. Kaposta, T. Leisner, C. Lupulescu, S. Minemoto, P. Rosendo-Francisco, and L. Woste, *Chemical Physics* **267**, (1-3), 231-239 (2001).

67 A. Bartelt, A. Lindinger, C. Lupulescu, S. Vajda, and L. Woste, *Physical Chemistry Chemical Physics* **6**, (8), 1679-1686 (2004).

68 B. J. Pearson, J. L. White, T. C. Weinacht, and P. H. Bucksbaum, *Physical Review A* **6306**, (6), (2001).

69 F. G. Omenetto, A. J. Taylor, M. D. Moores, and D. H. Reitze, *Optics Letters* **26**, (12), 938-940 (2001).

70 J. Kunde, B. Baumann, S. Arlt, F. Morier-Genoud, U. Siegner, and U. Keller, *Applied Physics Letters* **77**, (7), 924-926 (2000).

71 D. Meshulach, and Y. Silberberg, *Nature* **396**, (6708), 239-242 (1998).

72 D. Meshulach, and Y. Silberberg, *Physical Review A* **60**, (2), 1287-1292 (1999).

73 K. A. Walowicz, I. Pastirk, V. V. Lozovoy, and M. Dantus, *J. Phys. Chem. A* **106**, (41), 9369-9373 (2002).

74 V. V. Lozovoy, I. Pastirk, K. A. Walowicz, and M. Dantus, *J. Chem. Phys.* **118**, (7), 3187-3196 (2003).

75 M. Comstock, V. V. Lozovoy, I. Pastirk, and M. Dantus, *Optics Express* **12**, (6), 1061-1066 (2004).

76 J. M. Dela Cruz, I. Pastirk, M. Comstock, V. V. Lozovoy, and M. Dantus, *P. Natl. Acad. Sci. USA* **101**, (49), 16996-17001 (2005).

77 V. V. Lozovoy, I. Pastirk, and M. Dantus, *Optics Letters* **29**, (7), 775-777 (2004).

78 A. M. Weiner, J. P. Heritage, and J. A. Salehi, *Optics Letters* **13**, (4), 300-302 (1988).

79 A. M. Weiner, *Review of Scientific Instruments* **71**, (5), 1929-1960 (2000).

80 J. M. Dela Cruz, I. Pastirk, V. V. Lozovoy, K. A. Walowicz, and M. Dantus, *J. Phys. Chem. A* **108**, (1), 53-58 (2004).

81 I. Pastirk, J. M. Dela Cruz, K. A. Walowicz, V. V. Lozovoy, and M. Dantus, *Opt. Express* **11**, (14), 1695-1701 (2003).

82 J. M. Dela Cruz, I. Pastirk, M. Comstock, V. V. Lozovoy, and M. Dantus, *Proceedings of the National Academy of Sciences of the United States of America* **101**, (49), 16996-17001 (2004).

83 I. Pastirk, M. Kangas, and M. Dantus, *J. Phys. Chem. A* **109**, 2413-2416 (2005).

84 J. M. Dela Cruz, V. V. Lozovoy, and M. Dantus, *J. Phys. Chem. A* **109**, (38), 8447-8450 (2005).

85 J. M. Dela Cruz, M. Kangas, I. Pastirk, V. V. Lozovoy, and M. Dantus, *Journal of Modern Optics* **53**, (16-17), 2533-2541 (2006).

86 J. C. Shane, V. V. Lozovoy, and M. Dantus, *Journal of Physical Chemistry A* **110**, (40), 11388-11391 (2006).

87 V. V. Lozovoy, T. C. Gunaratne, J. C. Shane, and M. Dantus, *Chemphyschem* **7**, (12), 2471-2473 (2006).

88 V. V. Lozovoy, X. Zhu, T. C. Gunaratne, D. A. Harris, J. C. Shane, and M. Dantus, *Journal of Physical Chemistry A* **112**, (17), 3789-3812 (2008).

89 T. Gunaratne, M. Kangas, S. Singh, A. Gross, and M. Dantus, *Chemical Physics Letters* **423**, (1-3), 197-201 (2006).

90 R. L. Fork, B. I. Greene, and C. V. Shank, *Applied Physics Letters* **38**, (9), 671-672 (1981).

91 C. V. Shank, R. L. Fork, R. Yen, R. H. Stolen, and W. J. Tomlinson, *Applied Physics Letters* **40**, (9), 761-763 (1982).

92 R. L. Fork, C. V. Shank, and R. T. Yen, *Applied Physics Letters* **41**, (3), 223-225 (1982).

93 A. Migus, C. V. Shank, E. P. Ippen, and R. L. Fork, *Ieee Journal of Quantum Electronics* **18**, (1), 101-109 (1982).

94 M. Yamashita, K. Yamane, and R. Morita, *IEEE Journal of Selected Topics in Quantum Electronics* **12**, (2), 213-222 (2006).

95 P. F. Moulton, *Journal of the Optical Society of America B-Optical Physics* **3**, (1), 125-133 (1986).

96 P. Albers, E. Stark, and G. Huber, *Journal of the Optical Society of America B-Optical Physics* **3**, (1), 134-139 (1986).

97 C. Spielmann, F. Krausz, T. Brabec, E. Wintner, and A. J. Schmidt, *Optics Letters* **16**, (15), 1180-1182 (1991).

98 C. P. Huang, M. T. Asaki, S. Backus, M. M. Murnane, H. C. Kapteyn, and H. Nathel, *Optics Letters* **17**, (18), 1289-1291 (1992).

99 L. E. Hargrove, R. L. Fork, and M. A. Pollack, *Applied Physics Letters* **5**, (1), 4-& (1964).

100 E. P. Ippen, C. V. Shank, and A. Dienes, *Applied Physics Letters* **21**, (8), 348-& (1972).

101 U. Keller, G. W. Thooft, W. H. Knox, and J. E. Cunningham, *Optics Letters* **16**, (13), 1022-1024 (1991).

102 F. Salin, J. Squier, and M. Piche, *Optics Letters* **16**, (21), 1674-1676 (1991).

103 T. Brabec, C. Spielmann, P. F. Curley, and F. Krausz, *Optics Letters* **17**, (18), 1292-1294 (1992).

104 M. Piche, and F. Salin, *Optics Letters* **18**, (13), 1041-1043 (1993).

105 R. L. Fork, O. E. Martinez, and J. P. Gordon, *Optics Letters* **9**, (5), 150-152 (1984).

106 R. E. Sherriff, *Journal of the Optical Society of America B-Optical Physics* **15**, (3), 1224-1230 (1998).

107 J. P. Zhou, G. Taft, C. P. Huang, M. M. Murnane, H. C. Kapteyn, and I. P. Christov, *Optics Letters* **19**, (15), 1149-1151 (1994).

108 R. A. Baumgartner, and R. L. Byer, *Ieee Journal of Quantum Electronics* **15**, (6), 432-444 (1979).

109 M. Ohashi, K. Kitayama, Y. Ishida, and N. Uchida, *Applied Physics Letters* **41**,

(12), 1111-1113 (1982).

110 R. W. Tkach, and A. R. Chraplyvy, *Optical and Quantum Electronics* **21**, S105-S112 (1989).

111 V. E. Perlin, and H. G. Winful, *Journal of Lightwave Technology* **20**, (2), 250-254 (2002).

112 W. H. Lowdermilk, and J. E. Murray, *Journal of Applied Physics* **51**, (5), 2436-2444 (1980).

113 J. P. Zhou, C. P. Huang, M. M. Murnane, and H. C. Kapteyn, *Optics Letters* **20**, (1), 64-66 (1995).

114 J. E. Murray, and W. H. Lowdermilk, *Journal of Applied Physics* **51**, (7), 3548-3555 (1980).

115 M. D. Perry, and G. Mourou, *Science* **264**, (5161), 917-924 (1994).

116 D. Strickland, and G. Mourou, *Optics Communications* **56**, (3), 219-221 (1985).

117 P. Maine, D. Strickland, P. Bado, M. Pessot, and G. Mourou, *Ieee Journal of Quantum Electronics* **24**, (2), 398-403 (1988).

118 G. Vaillancourt, T. B. Norris, J. S. Coe, P. Bado, and G. A. Mourou, *Optics Letters* **15**, (6), 317-319 (1990).

119 S. Backus, C. G. Durfee, M. M. Murnane, and H. C. Kapteyn, *Review of Scientific Instruments* **69**, (3), 1207-1223 (1998).

120 F. X. Kartner, N. Matuschek, T. Schibli, U. Keller, H. A. Haus, C. Heine, R. Morf, V. Scheuer, M. Tilsch, and T. Tschudi, *Optics Letters* **22**, (11), 831-833 (1997).

121 N. Matuschek, F. X. Kartner, and U. Keller, *Ieee Journal of Quantum Electronics* **35**, (2), 129-137 (1999).

122 R. Szipocs, K. Ferencz, C. Spielmann, and F. Krausz, *Optics Letters* **19**, (3), 201-203 (1994).

123 A. Stingl, C. Spielmann, F. Krausz, and R. Szipocs, *Optics Letters* **19**, (3), 204-206 (1994).

124 L. Xu, G. Tempea, C. Spielmann, F. Krausz, A. Stingl, K. Ferencz, and S. Takano, *Optics Letters* **23**, (10), 789-791 (1998).

125 D. H. Sutter, G. Steinmeyer, L. Gallmann, N. Matuschek, F. Morier-Genoud, U. Keller, V. Scheuer, G. Angelow, and T. Tschudi, *Optics Letters* **24**, (9), 631-633 (1999).

126 L. Gallmann, D. H. Sutter, N. Matuschek, G. Steinmeyer, U. Keller, C. Iaconis, and I. A. Walmsley, *Optics Letters* **24**, (18), 1314-1316 (1999).

127 Y. Oishi, A. Suda, K. Midorikawa, and F. Kannari, *Review of Scientific Instruments* **76**, (9), (2005).

128 G. Stibenz, N. Zhavoronkov, and G. Steinmeyer, *Optics Letters* **31**, (2), 274-276 (2006).

129 M. Nisoli, S. DeSilvestri, and O. Svelto, *Applied Physics Letters* **68**, (20), 2793-2795 (1996).

130 M. Nisoli, S. DeSilvestri, O. Svelto, R. Szipocs, K. Ferencz, C. Spielmann, S. Sartania, and F. Krausz, *Optics Letters* **22**, (8), 522-524 (1997).

131 S. Sartania, Z. Cheng, M. Lenzner, G. Tempea, C. Spielmann, F. Krausz, and K. Ferencz, *Optics Letters* **22**, (20), 1562-1564 (1997).

132 L. Gallmann, T. Pfeifer, P. M. Nagel, M. J. Abel, D. M. Neumark, and S. R. Leone, *Applied Physics B-Lasers and Optics* **86**, (4), 561-566 (2007).

133 A. Bartels, and H. Kurz, *Optics Letters* **27**, (20), 1839-1841 (2002).

134 S. T. Cundiff, and J. Ye, *Reviews of Modern Physics* **75**, (1), 325-342 (2003).

135 S. A. Diddams, T. Udem, J. C. Bergquist, E. A. Curtis, R. E. Drullinger, L. Hollberg, W. M. Itano, W. D. Lee, C. W. Oates, K. R. Vogel, and D. J. Wineland, *Science* **293**, (5531), 825-828 (2001).

136 T. Udem, J. Reichert, R. Holzwarth, and T. W. Hansch, *Optics Letters* **24**, (13), 881-883 (1999).

137 G. T. Nogueira, and F. C. Cruz, *Optics Letters* **31**, (13), 2069-2071 (2006).

138 I. Pastirk, V. V. Lozovoy, and M. Dantus, *Chemical Physics Letters* **333**, (1-2), 76-82 (2001).

139 F. Verluise, V. Laude, Z. Cheng, C. Spielmann, and P. Tournois, *Optics Letters* **25**, (8), 575-577 (2000).

140 D. Kaplan, and P. Tournois, *Journal De Physique Iv* **12**, (PR5), 69-75 (2002).

141 A. Monmayrant, M. Joffre, T. Oksenhendler, R. Herzog, D. Kaplan, and P. Tournois, *Optics Letters* **28**, (4), 278-280 (2003).

142 A. M. Weiner, and J. P. Heritage, *Revue De Physique Appliquee* **22**, (12), 1619-1628 (1987).

143 A. M. Weiner, J. P. Heritage, and E. M. Kirschner, *Journal of the Optical Society of America B-Optical Physics* **5**, (8), 1563-1572 (1988).

144 A. M. Weiner, *IEEE J. Quantum Elect.* **28**, (4), 908-920 (1992).

145 R. J. Levis, G. M. Menkir, and H. Rabitz, *Science* **292**, 709-713 (2001).

146 C. J. Bardeen, V. V. Yakovlev, J. A. Squier, K. R. Wilson, S. D. Carpenter, and P. M. Weber, *J. Biomed. Opt.* **4**, (3), 362-367 (1999).

147 D. Oron, N. Dudovich, D. Yelin, and Y. Silberberg, *Phys. Rev. A* **65**, (4), Art. No. 043408 Part B (2002).

148 A. Neogi, H. Yoshida, T. Mozume, and O. Wada, *Opt. Commun.* **159**, (4-6), 225-229 (1999).

149 J. Ahn, T. C. Weinacht, and P. H. Bucksbaum, *Science* **287**, 463-465 (2000).

150 V. V. Lozovoy, and M. Dantus, *Chem. Phys. Lett.* **351**, (3-4), 213-221 (2002).

151Y. Yasuno, M. Nakama, Y. Sutoh, M. Itoh, M. Mori, and T. Yatagai, *Opt. Commun.* **186**, (1-3), 51-56 (2000).

152 R. L. Fork, C. H. B. Cruz, P. C. Becker, and C. V. Shank, *Optics Letters* **12**, (7), 483-485 (1987).

153 K. Naganuma, K. Mogi, and H. Yamada, *Ieee Journal of Quantum Electronics* **25**, (6), 1225-1233 (1989).

154 R. Trebino, and D. J. Kane, *Journal of the Optical Society of America a-Optics Image Science and Vision* **10**, (5), 1101-1111 (1993).

155 C. Iaconis, and I. A. Walmsley, *Optics Letters* **23**, (10), 792-794 (1998).

156 K. Yamane, Z. G. Zhang, K. Oka, R. Morita, M. Yamashita, and A. Suguro, *Optics Letters* **28**, (22), 2258-2260 (2003).

157 H. X. Miao, A. M. Weiner, C. Langrock, R. V. Roussev, and M. M. Fejer, *Optics Letters* **32**, (4), 424-426 (2007).

158 J. M. Dela Cruz, I. Pastirk, M. Comstock, and M. Dantus, *Opt. Express* **12**, (17), 4144-4149 (2004).

159 A. Baltuska, M. S. Pshenichnikov, and D. A. Wiersma, *Opt. Lett.* **23**, (18), 1474-1476 (1998).

160 A. Baltuska, M. S. Pshenichnikov, and D. A. Wiersma, *IEEE J. Quantum Elect.* **35**, (4), 459-478 (1999).

161 D. A. Harris, J. C. Shane, V. V. Lozovoy, and M. Dantus, *Optics Express* **15**, (4), 1932-1938 (2007).

162 V. V. Lozovoy, B. Xu, Y. Coello, and M. Dantus, *Optics Express* **16**, (2), 592-597 (2008).

163 B. Xu, J. M. Gunn, J. M. Dela Cruz, V. V. Lozovoy, and M. Dantus, *Journal of the Optical Society of America B-Optical Physics* **23**, (4), 750-759 (2006).

164 S. Diddams, and J. C. Diels, *J. Opt. Soc. Am. B* **13**, (6), 1120-1129 (1996).

165 I. H. Malitson, *J. Opt. Soc. Am.* **55**, (10), 1205-1209 (1965).

166 Ohara Corp., "Optical glass catalog data" retrieved May 2, 2005, http://www.oharacorp.com/swf/catalog.html.

167 Y. Coello, B. Xu, T. L. Miller, V. V. Lozovoy, and M. Dantus, *Applied Optics* **46**, (35), 8394-8401 (2007).

168 L. Gallmann, D. H. Sutter, N. Matuschek, G. Steinmeyer, and U. Keller, *Appl. Phys. B- Lasers O.* **70**, (Suppl.), S67-S75 (2000).

169 V. V. Lozovoy, and M. Dantus, *Annu. Rep. Prog. Chem., Sect. C: Phys. Chem.* **102**, 227 - 258 (2006).

170 J. P. Ogilvie, D. Debarre, X. Solinas, J. L. Martin, E. Beaurepaire, and M. Joffre, *Optics Express* **14**, (2), 759-766 (2006).

171 P. Xi, Y. Andegeko, L. R. Weisel, V. V. Lozovoy, and M. Dantus, *Opt. Commun.* **281**, (7), 1841-1849 (2008).

172 B. von Vacano, T. Buckup, and M. Motzkus, *Journal of the Optical Society of*

America B-Optical Physics **24**, (5), 1091-1100 (2007).

173 A. Baltuska, and T. Kobayashi, *Applied Physics B-Lasers and Optics* **75**, (4-5), 427-443 (2002).

174 T. Binhammer, E. Rittweger, R. Ell, F. X. Kartner, and U. Morgner, *IEEE Journal of Quantum Electronics* **41**, (12), 1552-1557 (2005).

175 P. Baum, S. Lochbrunner, and E. Riedle, *Optics Letters* **29**, (14), 1686-1688 (2004).

176 V. V. Lozovoy, J. C. Shane, B. W. Xu, and M. Dantus, *Optics Express* **13**, (26), 10882-10887 (2005).

177 V. V. Lozovoy, and M. Dantus, *Chem. Phys. Chem.* **6**, 1970-2000 (2005).

178 T. Binhammer, E. Rittweger, U. Morgner, R. Ell, and F. X. Kartner, *Optics Letters* **31**, (10), 1552-1554 (2006).

179 H. Li, D. A. Harris, B. Xu, P. J. Wrzesinski, V. V. Lozovoy, and M. Dantus, *Optics Express* **16**, (8), 5499-5504 (2008).

180 M. Hentschel, R. Kienberger, C. Spielmann, G. A. Reider, N. Milosevic, T. Brabec, P. Corkum, U. Heinzmann, M. Drescher, and F. Krausz, *Nature* **414**, (6863), 509-513 (2001).

181 Z. Cheng, A. Furbach, S. Sartania, M. Lenzner, C. Spielmann, and F. Krausz, *Optics Letters* **24**, (4), 247-249 (1999).

182 B. Schenkel, J. Biegert, U. Keller, C. Vozzi, M. Nisoli, G. Sansone, S. Stagira, S. De Silvestri, and O. Svelto, *Optics Letters* **28**, (20), 1987-1989 (2003).

183 H. Li, D. A. Harris, B. Xu, P. J. Wrzesinski, V. V. Lozovoy, and M. Dantus, *Optics Express* **16**, (8), 5499-5504 (2008).

184 B. Xu, Y. Coello, G. T. Nogueira, F. C. Cruz, and M. Dantus, *submitted Optics Express*, (2008).

185 J. Jasapara, and W. Rudolph, *Opt. Lett.* **24**, (11), 777-779 (1999).

186 I. Amat-Roldan, I. G. Cormack, P. Loza-Alvarez, and D. Artigas, *Opt. Lett.* **29**, (19), 2282-2284 (2004).

187 D. N. Fittinghoff, A. C. Millard, J. A. Squier, and M. Muller, *IEEE J. Quantum*

Elect. **35**, (4), 479-486 (1999).

188 M. Muller, J. Squier, R. Wolleschensky, U. Simon, and G. J. Brakenhoff, *J. Microsc-Oxford* **191**, 141-150 (1998).

189 D. N. Fittinghoff, J. A. Squier, C. P. J. Barty, J. N. Sweetser, R. Trebino, and M. Muller, *Opt. Lett.* **23**, (13), 1046-1048 (1998).

190 W. Denk, J. Strickler, and W. Webb, *Science* **248**, (4951), 73-76 (1990).

191 Y. Coello, B. W. Xu, T. L. Miller, V. V. Lozovoy, and M. Dantus, *Applied Optics* **46**, (35), 8394-8401 (2007).

192 S. A. Rice, and M. Zhao, *Optical control of molecular dynamics*. Wiley: New York, 2000; p 437.

193 Z. Zheng, and A. M. Weiner, *Chemical Physics* **267**, (1-3), 161-171 (2001).

194 N. Dudovich, D. Oron, and Y. Silberberg, *Nature* **418**, (6897), 512-514 (2002).

195 D. Oron, N. Dudovich, and Y. Silberberg, *Physical Review Letters* **90**, (21), 213902 (2003).

196 N. Dudovich, B. Dayan, S. M. G. Faeder, and Y. Silberberg, *Physical Review Letters* **86**, (1), 47-50 (2001).

197 N. Dudovich, D. Oron, and Y. Silberberg, *Physical Review Letters* **88**, (12), 123004 (2002).

198 E. Gershgoren, R. A. Bartels, J. T. Fourkas, R. Tobey, M. M. Murnane, and H. C. Kapteyn, *Optics Letters* **28**, (5), 361-363 (2003).

199 B. J. Pearson, J. L. White, T. C. Weinacht, and P. H. Bucksbaum, *Physical Review a* **6306**, (6), art. no. 063412 (2001).

200 R. A. Bartels, S. Backus, M. M. Murnane, and H. C. Kapteyn, *Chemical Physics Letters* **374**, (3-4), 326-333 (2003).

201 S. A. Malinovskaya, P. H. Bucksbaum, and P. R. Berman, *Physical Review A* **69**, (1), 013801 (2004).

202 H. A. Rabitz, M. M. Hsieh, and C. M. Rosenthal, *Science* **303**, (5666), 1998-2001 (2004).

203 M. R. Schroeder, *Number theory in science and communication : with applications in cryptography, physics, digital information, computing, and self-similarity*. 3rd ed.; Springer: Berlin ; New York, 1997; p 362.

204 J. Knauer, http://www.cecm.sfu.ca/~jknauer/labs/records.html.

205 P. Borwein, K. K. S. Choi, and J. Jedwab, *Ieee Transactions on Information Theory* **50**, (12), 3234-3249 (2004).

206 J. P. Hermann, and J. Ducuing, *Physical Review A* **5**, (6), 2557-& (1972).

207 A. J. Twarowski, and D. S. Kliger, *Chemical Physics* **20**, (2), 259-264 (1977).

208 M. Sheikbahae, A. A. Said, T. H. Wei, D. J. Hagan, and E. W. Vanstryland, *IEEE Journal of Quantum Electronics* **26**, (4), 760-769 (1990).

209 C. Xu, and W. W. Webb, *Journal of the Optical Society of America B-Optical Physics* **13**, (3), 481-491 (1996).

210 M. A. Albota, C. Xu, and W. W. Webb, *Applied Optics* **37**, (31), 7352-7356 (1998).

211 A. A. Heikal, and W. W. Webb, *Biophysical Journal* **76**, (1), A260-A260 (1999).

212 S. H. Huang, A. A. Heikal, and W. W. Webb, *Biophysical Journal* **82**, (5), 2811-2825 (2002).

213 J. P. Ogilvie, K. J. Kubarych, A. Alexandrou, and M. Joffre, *Optics Letters* **30**, (8), 911-913 (2005).

214 P. Rohwetter, J. Yu, G. Mejean, K. Stelmaszczyk, E. Salmon, J. Kasparian, J. P. Wole, and L. Woste, *Journal of Analytical Atomic Spectrometry* **19**, (4), 437-444 (2004).

215 F. C. DeLucia, A. C. Samuels, R. S. Harmon, R. A. Walters, K. L. McNesby, A. LaPointe, R. J. Winkel, and A. W. Miziolek, *Ieee Sensors Journal* **5**, (4), 681-689 (2005).

216 J. C. Carter, S. M. Angel, M. Lawrence-Snyder, J. Scaffidi, R. E. Whipple, and J. G. Reynolds, *Applied Spectroscopy* **59**, (6), 769-775 (2005).

217 S. K. Sharma, A. K. Misra, P. G. Lucey, S. M. Angel, and C. P. McKay, *Applied Spectroscopy* **60**, (8), 871-876 (2006).

218 *Existing and Potential Standoff Explosives Detection Techniques.* The National Academies Press: 2004.

219 P. D. Maker, and R. W. Terhune, *Physical Review* **137**, (3A), A801-& (1965).

220 G. I. Petrov, R. Arora, V. V. Yakovlev, X. Wang, A. V. Sokolov, and M. O. Scully, *Proceedings of the National Academy of Sciences of the United States of America* **104**, (19), 7776-7779 (2007).

221 M. O. Scully, G. W. Kattawar, R. P. Lucht, T. Opatrny, H. Pilloff, A. Rebane, A. V. Sokolov, and M. S. Zubairy, *Proceedings of the National Academy of Sciences of the United States of America* **99**, (17), 10994-11001 (2002).

222 D. Pestov, R. K. Murawski, G. O. Ariunbold, X. Wang, M. C. Zhi, A. V. Sokolov, V. A. Sautenkov, Y. V. Rostovtsev, A. Dogariu, Y. Huang, and M. O. Scully, *Science* **316**, (5822), 265-268 (2007).

223 J. X. Cheng, A. Volkmer, and X. S. Xie, *Journal of the Optical Society of America B-Optical Physics* **19**, (6), 1363-1375 (2002).

224 S. H. Lim, A. G. Caster, and S. R. Leone, *Physical Review A* **72**, (4), (2005).

225 B. Von Vacano, and M. Motzkus, *Optics Communications* **264**, (2), 488-493 (2006).

226 I. Pastirk, X. Zhu, R. M. Martin, and M. Dantus, *Optics Express* **14**, (19), 8885-8889 (2006).

227 D. Oron, N. Dudovich, and Y. Silberberg, *Phys. Rev. Lett.* **89**, 273001 (2002).